Cavity-induced artificial gauge field in a Bose-Hubbard ladder

Masterarbeit in Physik
von
Catalin-Mihai Halati

angefertigt am
Helmholtz-Institut für Strahlen- und Kernphysik

vorgelegt der
Mathematisch-Naturwissenschaftlichen Fakultät
der
Rheinischen Friedrich-Wilhelms-Universität Bonn

September, 2017

1. Gutachter(in):   Prof. Dr. Corinna Kollath
2. Gutachter(in):   Prof. Dr. Hartmut Monien

Abstract

We investigate the preparation of stationary states of an open system, as the attractor states of the dissipative dynamics are more robust than the many-body states of a closed system. We consider theoretically ultracold interacting bosonic atoms confined to quasi-one-dimensional ladder structures formed by optical lattices and coupled to the field of an optical cavity. The atoms can tunnel along the leg direction and collect a spatial phase imprint during a cavity-assisted tunneling along a rung via Raman transitions employing a cavity mode and a transverse running wave pump beam. By adiabatic elimination of the cavity field we obtain an effective Hamiltonian for the bosonic atoms, which needs to be analyzed self-consistently. Firstly, we characterize the low energy properties of the effective Hamiltonian by performing a Bogoliubov theory for quasiparticles excitations on top of the bosonic condensate, whose spectrum has characteristic features of the superfluid phase. Furthermore, using the numerical density matrix renormalization group method, we obtain a rich steady state diagram of self-organized steady states. Transitions between superfluid to Mott-insulating states occur, on top of which we can have Meissner, vortex liquid, and vortex lattice phases. Also a state that explicitly breaks the symmetry between the two legs of the ladder, namely the biased-ladder phase is dynamically stabilized.

Contents

Contents

IV

1. Introduction

The field of studying quantum phenomena within ultracold atoms systems has attracted majors efforts since the realization of Bose-Einstein Condensation [1–3] and quantum degenerate Fermi gases [4] 20 years ago. By loading the ultracold atoms into optical lattice potentials one can effectively enhance the interaction between the atoms, realizing the strongly correlated regimes. Thus the system of ultracold atoms in optical lattices provides a powerful framework for the realization of the strongly correlated phases, due to the high controllability of parameters [5]. The experimental realization of the superfluid to Mott-insulator transition of bosonic atoms trapped in an optical lattice [6] represents a remarkable example. In this context, the playground of theorists consists in various versions of the Bose-Hubbard model [7], in which the interplay between quantum kinetic processes and, short and long-range interactions can be studied. The Bose-Hubbard model is well-known from condensed matter physics, as the minimal model that captures the physics of interacting bosons in a lattice, its phase diagram has been explored both analytical and numerical [8–20].

In recent years, ultracold atoms coupled to an optical cavity mode have proven to be an exciting field of physics [21]. One can target the desired steady state by engineering the coupling to the environment [22]. The steady state is realized as the attractor of the dissipative dynamics, thus being protected from external perturbations. In recent experiments [23, 24], ultracold bosonic atoms placed in an optical cavity have realized a Dicke phase transition [25–28]. In the experiment from Ref. [23] a Bose-Einstein condensate has been placed inside an optical cavity and coupled also to a standing-wave transverse pump beam. Above a critical value of the intensity of the transverse pump beam the atoms self-organize into a checkerboard pattern of the density and the cavity field has a finite value.

In addition to the coupling to the optical cavity, one can confine the atomic gas with external optical lattice potentials, to realize a modified Bose-Hubbard model with long-range interactions [29, 30]. This has been investigated theoretically [31, 32] and, in particular, the effect of the long-range interactions on the superfluid to Mott insulator transition has been analyzed [33–39]. More complex combined cavity-atom systems have been proposed in which self-organization can occur, as the organization of bosonic atoms in triangular or hexagonal lattices [40], or of fermionic atoms into superradiant phases [41–44]. Disordered structures have been theoretically proposed in setups such as multimode cavities [45–52]. Phases for which the spin-orbit

coupling plays an important role have been discussed for standing-wave cavities [53–56], or ring cavities [57, 58].

Essential phenomena arise in systems of charged quantum particles subjected to a magnetic field, for instance, the quantum Hall effect [59, 60]. It describes the movement of quantum particles under the action of a magnetic field in two dimensions. Even though the integer quantum Hall effect is understood from the behavior of noninteracting electrons, other exotic physics can be studied in interacting many-body systems in the presence of an Abelian gauge field [61, 62], like the fractional quantum Hall effect.

In this context, a natural development is to realize gauge fields in ultracold atomic systems [63–65]. The generation of an artificial gauge field has been implemented in different ways such as Raman coupling [66, 67], lattice shaking [68], or laser-assisted hopping [69, 70]. These artificial gauge fields for neutral atoms have similar effects as magnetic fields for charged particles. In the mentioned setups a static artificial magnetic field is induced, thus no feedback of the atoms on the artificial field exist. The Hofstadter model in two dimensions [70–73] or on a ladder geometry [74] and the Haldane model [75] are realized.

The quasi-one-dimensional ladder structure is the minimal geometry in which the effects of gauge fields can lead to interesting effects. For weakly interacting ultracold bosons on a ladder a Meissner and a vortex superfluid phase were observed by measuring the chiral current that flows along the legs of the ladder [74]. Furthermore, the rich phase diagram has been explored, with other exciting phases such as vortex lattice and biased ladder superfluid phase, Meissner and vortex Mott insulator theoretically predicted to occur [76–91].

Recently proposals have been put forward for the dynamic generation of gauge fields by a cavity-assisted tunneling. The artificial magnetic field emerges dynamically due to the feedback mechanism between the cavity field and the motion of atoms [92–97]. The steady state diagram and the dynamics has been determined in the case of noninteracting fermions including states with chiral currents on a ladder geometry [92–94] or non-trivial topological properties in two dimensions [95].

In the present work we consider interacting bosons on a ladder structure coupled to a cavity mode and explore the steady state diagram for different on-site interaction strengths, different magnetic fluxes and different fillings. We characterize the self-organized phases that arise and we investigate the stability of these phase in the coupled atomic cavity system. The thesis is an extended version of the work we presented in Ref. [98] and similarities can exist in the

overlapping parts.

The structure of the thesis is as follows. In Chap. 2 we describe the setup of the bosonic atoms in the optical cavity in Sec. 2.1, and the theoretical model in Sec. 2.2. We derive an effective model for the atomic degrees of freedom by performing the adiabatic elimination of the cavity field in Sec. 2.3, and deduce a stability condition for the steady states in Sec. 2.4. In the next chapter, Chap. 3, we discuss the properties of the effective Hamiltonian, by looking at the low-energy physics in Sec. 3.1 and in Sec. 3.2, and we briefly summarize the phases observed in the rich phase diagram in Sec. 3.3. In Chap. 4 we discuss the density matrix renormalization group method and certain technical details of its implementation and convergence. The stable self-organized phases with a finite cavity field and their properties are presented in Chap. 5.

2. Bose-Hubbard ladder coupled to a cavity mode

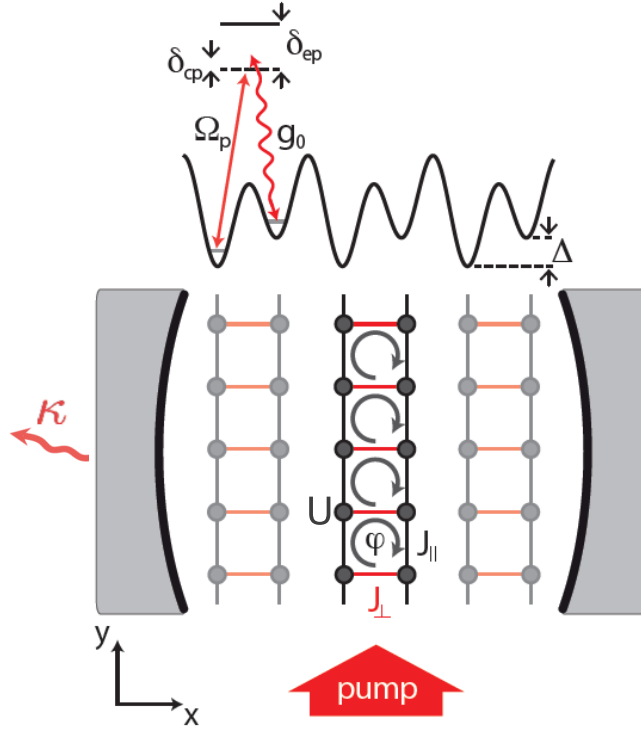## 2.1. Description of the setup

Figure 2.1.: Sketch of the setup involving one pump beam, adapted from Ref. [95]. The bosonic atoms in an optical cavity are subjected to an optical super-lattice potential which creates an array of ladders. The atoms tunnel along the legs with the amplitude $J_\parallel$, via the cavity-induced processes they tunnel along the rungs with an effective amplitude $J_\perp$ and have an on-site interaction of strength U. In the level scheme of the cavity-induced tunneling, the energy offset between two neighboring wells, Δ, strongly suppresses the tunneling along the rungs. This is restored by a Raman processes involving the cavity mode with vacuum Rabi frequency g_0 and a transverse pump beam with Rabi frequency Ω_p, respectively.

We study an ultracold bosonic gas placed in an optical cavity and additionally subjected to optical lattice potentials (Fig. 2.1), we will follow our work from Ref. [98]. A similar setup has been introduced and discussed in previous work in the context of fermionic atoms [93–95]. The optical super-lattice potentials confine the atoms to an array of decoupled ladders. The

first step in obtaining this structure is to create two-dimensional decoupled layers by applying a strong optical lattice potential along the z-direction. One applies an optical lattice of wavelength λ_y along the y-direction, which induces a lattice spacing of $d_\parallel = \lambda_y/2$. A superposition of two optical lattices with wavelengths λ_x and $\lambda_x/2$ is applied along the x-direction, such that decoupled double wells are formed with an energy offset Δ between the two wells (see Fig. 2.1). The lattice height along the y-direction is sufficiently low such that the atoms tunnel with amplitude $J_\parallel$ between neighboring sites. The potential offset between the two wells along x-direction strongly suppresses the tunneling along the rungs. The tunneling is restored by a Raman transition involving a standing-wave cavity mode and the running-wave pump laser (Fig. 2.1). The cavity mode has the frequency ω_c, vacuum Rabi frequency g_0 and the wave-vector $\mathbf{k}_c = k_c \mathbf{e}_x$ along the x-direction, where $\mathbf{e}_i$, with $i = x, y, z$, denote the unit vectors along the three spatial directions. All other cavity modes are assumed to be far detuned from the possible transitions and are not considered. The pump laser beam has the frequency ω_p and the wave-vector $\mathbf{k}_p = k_p \mathbf{e}_y$. The pump and cavity modes are considered to be far detuned from the internal atomic transition, i.e. $\omega_e \gg \omega_c, \omega_p$, thus the excited state population is negligible and it can be adiabatically eliminated. The detuning between the cavity mode and the pumping beam is chosen such that it is close to the potential offset, $\hbar(\omega_c - \omega_p) \approx -\Delta$. A cavity-induced Raman tunneling along the rungs of the ladder is obtained via the feedback mechanism between the motion of the atoms and the cavity mode. In the following we will use the rotating frame with the frequency ω_p.

During the Raman processes a spatially dependent phase factor $e^{-i\Delta \mathbf{k} \cdot \mathbf{r}}$ is imprinted onto the atomic wave-function, where $\Delta \mathbf{k} = \pm k_c \mathbf{e}_x + k_p \mathbf{e}_y$. The cavity mode does not give a contribution when the tunneling around a plaquette is considered. However, due to the running-wave nature of the pump beam the atoms collect a phase $\varphi(j+1)$ tunneling on the rung $j+1$ and a phase $-\varphi j$ on the rung j, where $\varphi \simeq \pi \lambda_y/\lambda_p$, The accumulated phase φ is equivalent to the Aharonov-Bohm phase for charged particles subjected to a magnetic field oriented orthogonal to the ladder surface. Thus, the bosonic atoms experience an artificial magnetic field in the presence of a finite cavity field. In an experimental realization, the flux φ can be varied by modifying the angle of the pump beams with respect to the x-y-plane.

2.2. Derivation of the model

In this section we will perform an expansion in the Wannier basis of the atomic field operators, obtaining a model for the atomic-cavity system in the tight-binding description. Thus we

2.2 Derivation of the model

reduce the original Hamiltonian in continuum space to a lattice Hamiltonian with only a few effective parameters. We will first derive the Hamiltonian for the setup with only one transversal pump beam, as presented in Fig. 2.1 and used in Ref. [95], and at the end of the section we will generalize the result for the case with two pump beams, as depicted in Fig. 2.2. A bosonic quantum gas placed in an optical cavity subjected to an optical lattice and a transversal pump beam can be described in the rotating wave approximation by the Hamiltonian [21]

$$H = H_g + H_e + H_{int} + H_c + H_{ac} + H_{ap}, \tag{2.1}$$

where the different terms will be defined in the following. Only two internal electronic states of the atoms are relevant for the atomic dynamics, the ground state (g) and the excited state (e) in resonance with the considered transitions. Their dynamics is described by

$$H_g = \int d^3r \left(\psi_g^\dagger(\mathbf{r}) \left(-\frac{\hbar^2}{2m} \nabla^2 + V_g(\mathbf{r}) \right) \psi_g(\mathbf{r}) \right),$$
$$H_e = \int d^3r \left(\psi_e^\dagger(\mathbf{r}) \left(-\frac{\hbar^2}{2m} \nabla^2 + \hbar\delta_{ep} + V_e(\mathbf{r}) \right) \psi_e(\mathbf{r}) \right), \tag{2.2}$$

with $\psi_g(\mathbf{r})$ and $\psi_e(\mathbf{r})$ the bosonic annihilation operators at position $\mathbf{r}$ in the ground state and in excited state, respectively. The field operators fulfill the usual bosonic commutation relations, $\left[\psi(\mathbf{r}), \psi^\dagger(\mathbf{r}') \right] = \delta(\mathbf{r} - \mathbf{r}')$. The external potentials for the atom in the ground and the excited state are represented by $V_g(\mathbf{r})$ and $V_e(\mathbf{r})$, and m is the mass of the bosonic atoms. In the rotating frame of the pump beam with the frequency ω_p, the detuning of the pump laser from the atomic transition is given by $\delta_{ep} = \omega_e - \omega_p$, where the internal atomic transition has a frequency of ω_e. For a large detuning δ_{ep} the excited state population is negligible, thus the interaction between the atoms in the ground state and the excited state, and also between the atoms in the excited state can be neglected. Thus the interaction part of the Hamiltonian reads

$$H_{int} = \frac{g}{2} \int d^3r \left(\psi_g^\dagger(\mathbf{r})^2 \psi_g(\mathbf{r})^2 \right), \tag{2.3}$$

where the strength of the contact interactions is given by $g = \frac{4\pi\hbar^2 a_s}{m}$, with a_s the s-wave scattering length.

The next term in the Hamiltonian (2.1) gives the dynamics of the cavity field

$$H_c = \hbar\delta_{cp}a^\dagger a, \tag{2.4}$$

The bosonic operators a and $a^\dagger$ are the annihilation and creation operators for the cavity photon mode, in the rotating frame at the pump frequency, with $\delta_{cp} = \omega_c - \omega_p$.

$$H_{ac} = \hbar g_0 \int d^3r \left(\psi_g^\dagger(\mathbf{r}) \cos(\mathbf{k}_c\mathbf{r})a^\dagger \psi_e(\mathbf{r}) + h.c. \right), \tag{2.5}$$

where g_0 is the vacuum Rabi frequency and $\mathbf{k}_c$ is the wave-vector of the cavity mode.

The last term corresponds to the coherent drive of the atoms by the pump laser beams

$$H_{ap} = \hbar\Omega_p \int d^3r \left(\psi_g^\dagger(\mathbf{r})e^{-i\mathbf{k}_p\mathbf{r}} \psi_e(\mathbf{r}) + h.c. \right), \tag{2.6}$$

with Ω_p the Rabi frequency and $\mathbf{k}_p$ is the wave-vector of the pump beam.

In the following we will perform the adiabatic elimination of the excited state, obtaining an effective Hamiltonian which governs the evolution of the atomic ground state coupled to a mode of the cavity field. The equations of motion for the field operators of the excited and ground state, without any external potentials, are

$$
\begin{aligned}
i\hbar\partial_t\psi_e(\mathbf{r}) =& \left(-\frac{\hbar^2}{2m}\nabla^2 + \hbar\delta_{ep} \right)\psi_e(\mathbf{r}) \\
&+ \left(\hbar g_0 \cos(\mathbf{k}_c\mathbf{r})a + \hbar\Omega_p e^{i\mathbf{k}_p\mathbf{r}} \right)\psi_g^\dagger(\mathbf{r}), \\
i\hbar\partial_t\psi_g(\mathbf{r}) =& \left(-\frac{\hbar^2}{2m}\nabla^2 + g\psi_g^\dagger(\mathbf{r})\psi_g(\mathbf{r}) \right)\psi_g(\mathbf{r}) \\
&+ \left(\hbar g_0 \cos(\mathbf{k}_c\mathbf{r})a^\dagger + \hbar\Omega_p e^{-i\mathbf{k}_p\mathbf{r}} \right)\psi_e^\dagger(\mathbf{r}).
\end{aligned}
\tag{2.7}
$$

Assuming that the internal time-scales are faster than the external (not electronic) ones, $\delta_{ep} \gg g_0, \Omega_p$, we can expand the stationary value of $\psi_e(\mathbf{r})$ up to first order in V_{eff}/δ_{ep}, where $V_{eff} = \hbar g_0 \cos(\mathbf{k}_c\mathbf{r})a + \hbar\Omega_p e^{i\mathbf{k}_p\mathbf{r}}$. Considering that at $t = 0$ the cavity is empty and we are not pumping the system, $V_{eff}(t = 0) = 0$, we obtain the following stationary value for the excited state field

2.2 Derivation of the model

$$\psi_e(\mathbf{r}) = -\frac{1}{\delta_{ep}}\big(\hbar g_0 \cos(\mathbf{k}_c \mathbf{r})a + \hbar\Omega_p e^{i\mathbf{k}_p\mathbf{r}}\big)\psi_g(\mathbf{r}). \tag{2.8}$$

By substituting the stationary value of the excited state field (2.8) into the equation of motion for the ground state field (2.7), we will obtain an equation of motion formally identical to the one generated by the following effective Hamiltonian, in which have been considered only the two-photon resonant processes which involve one cavity photon and one pump photon

$$H = H_g + H_{int} + H_c + H_{ac}, \tag{2.9}$$

$$H_{ac} = -\frac{\hbar g_0 \Omega_p}{\delta_{ep}} \int d^3r \big(e^{i\mathbf{k}_p\mathbf{r}}a^\dagger + e^{-i\mathbf{k}_p\mathbf{r}}a\big)\cos(\mathbf{k}_c\mathbf{r})\psi_g^\dagger(\mathbf{r})\psi_g(\mathbf{r}). \tag{2.10}$$

In the case of a sufficiently deep optical lattice potential we can expand the bosonic fields into the corresponding Wannier basis of the lattice

$$\psi_g(\mathbf{r}) = \sum_{j,m=0,1} W(\mathbf{r} - \mathbf{R}_{m,j})b_{m,j} \tag{2.11}$$

where $\mathbf{R}_{m,j}$ is the position vector corresponding to the lattice site j on the leg $m = 0, 1$ and $b_{m,j}$ is the bosonic annihilation operator of the atoms. The Wannier functions for a site $\mathbf{R}$ are defined as the Fourier transform of the Bloch functions $u_k(\mathbf{r})$, $W(\mathbf{r} - \mathbf{R}) = \frac{1}{V_0}\int_{k\in FBZ} d^3k\, e^{-i\mathbf{k}\mathbf{R}}u_k(\mathbf{r})$. Substituting the expansion (2.11) into the Hamiltonian (2.9) and considering that we have hopping only between the nearest neighbors the first two terms of the Hamiltonian (2.9) become

$$H_g = -J_\parallel \sum_{j,m=0,1} (b_{m,j}^\dagger b_{m,j+1} + b_{m,j+1}^\dagger b_{m,j}),$$

$$H_{int} = \frac{U}{2} \sum_{j,m=0,1} n_{m,j}(n_{m,j} - 1). \tag{2.12}$$

The operator $n_{m,j} = b_{m,j}^\dagger b_{m,j}$ is the number operator. The tunneling amplitude along the legs of the ladder $J_\parallel$ and the strength of the on-site interaction U are defined by

$$J_{\parallel} = -\int d^3r \, W^*(\mathbf{r} - \mathbf{R}_{m,j})\left(-\frac{\hbar^2}{2m}\nabla^2 + V_g(\mathbf{r})\right)W(\mathbf{r} - \mathbf{R}_{m,j}),$$

$$U = g\int d^3r \, \left|W(\mathbf{r} - \mathbf{R}_{m,j})\right|^4, \tag{2.13}$$

where $V_g(\mathbf{r})$ now represents the external potential without the lattice potential.

For the last term the expansion reads

$$H_{ac} = -\frac{\hbar g_0 \Omega_p}{\delta_{ep}}\sum_{\substack{j,m=0,1 \\ j',m'=0,1}} b^\dagger_{m,j}b_{m',j'}\int d^3r\left(e^{i\mathbf{k}_p\mathbf{r}}a^\dagger + e^{-i\mathbf{k}_p\mathbf{r}}a\right)\cos(\mathbf{k}_c\mathbf{r})W^*(\mathbf{r} - \mathbf{R}_{m,j})W(\mathbf{r} - \mathbf{R}_{m',j'}). \tag{2.14}$$

In the considered setup we can evaluate the contributions to the integral from (2.14) for each direction independently, since they are separable. The most important contribution for the y-direction comes from the on-site overlap of the Wannier functions, as the hopping in the y-direction is not pump-cavity assisted.

$$e^{\pm i\varphi j}\phi_{\parallel} = e^{\pm i k_p d_{\parallel} j}\int dy \, W^*(y)W(y)e^{\mp i k_p y}, \tag{2.15}$$

with the imprinted phase $\varphi = k_p d_{\parallel}$, collected by an atom while tunneling around a plaquette.

In the x-direction we have multiple contributions, from the overlap of the Wannier functions between two adjacent sites

$$\phi_{\perp,\pm} = \int dx \, W^*(x)W(x \pm d_{\perp})\cos(k_c x), \tag{2.16}$$

where $d_{\perp}$ is the lattice spacing along the rungs of the ladder. The other contributions come from the on-site integrals, which have a different value on each leg, thus we have an oscillating energy offset between the two sites on the same rung.

9

2.2 Derivation of the model

$$\phi_{\perp,m=0} = \int dx \, W^*(x)W(x)\cos(k_c x),$$

$$\phi_{\perp,m=1} = \int dx \, W^*(x-d_\perp)W(x-d_\perp)\cos(k_c x). \tag{2.17}$$

We assume that all contributions for the x-direction are included in an effective parameter $\phi_\perp$ and its value can be controlled by the geometry of the lattice [93]. Thus H_{ac} is given by

$$H_{ac} = -\hbar\tilde{\Omega}(aK_\perp + a^\dagger K_\perp^\dagger), \tag{2.18}$$

$$K_\perp = \sum_j e^{i\varphi j} b_{0,j}^\dagger b_{1,j},$$

$$\hbar\tilde{\Omega} = \frac{\hbar g_0 \Omega_p}{\delta_{ep}}\phi_\parallel\phi_\perp.$$

In the tight-binding description the Hamiltonian describing the coupled system reads

$$H = H_c + H_\parallel + H_{int} + H_{ac} \tag{2.19}$$

$$H_c = \hbar\delta_{cp}a^\dagger a$$

$$H_\parallel = -J_\parallel \sum_{j,m=0,1} (b_{m,j}^\dagger b_{m,j+1} + b_{m,j+1}^\dagger b_{m,j})$$

$$H_{int} = \frac{U}{2} \sum_{j,m=0,1} n_{m,j}(n_{m,j} - 1)$$

$$H_{ac} = -\hbar\tilde{\Omega}(aK_\perp + a^\dagger K_\perp^\dagger)$$

$$K_\perp = \sum_j e^{i\varphi j} b_{0,j}^\dagger b_{1,j}.$$

The setup involving just one pump beam, described by the Hamiltonian (2.19), has the following shortcoming, for small photon numbers in the cavity the transition which involves the annihilation of a pump photon and creation of a cavity photon is more favorable. Thus, over long times we effectively pump the atoms from one leg to the other, in the direction of $K_\perp$, creating a density imbalance. In order to prevent the privileged direction of tunneling, we couple
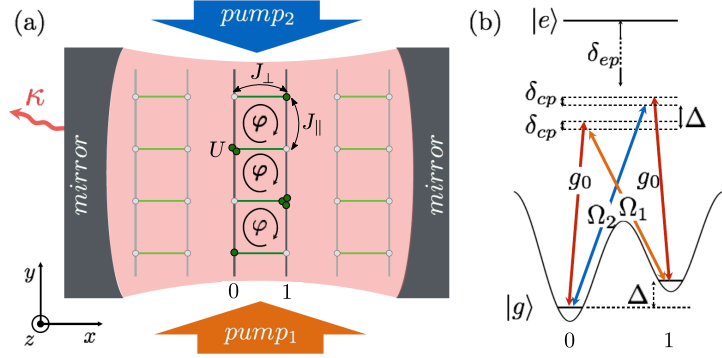
Figure 2.2.: (a) Sketch of the setup involving two transverse pump beams, adapted from Ref. [98]. The bosonic atoms in an optical cavity are subjected to an optical super-lattice potential which creates an array of ladders. The atoms tunnel along the legs with the amplitude $J_{\parallel}$, via the cavity-induced processes they tunnel along the rungs with an effective amplitude $J_{\perp}$ and have an on-site interaction of strength U. (b) Level scheme of the cavity-induced tunneling: $|g\rangle$, $|e\rangle$ denote the ground and excited internal electronic states. The energy offset between two neighboring wells, Δ, strongly suppresses the tunneling along the rungs. This is restored by two Raman processes each of which involve the cavity mode with vacuum Rabi frequency g_0 and a transverse pump beam with Rabi frequency $\Omega_{1,2}$, respectively.

the tunneling in each direction to both the creation and annihilation operators of the cavity field, using two pump laser beams [26] (see Fig. 2.2). In this case, the tunneling is restored by two balanced Raman transitions each of them involving a standing-wave cavity mode and a running-wave pump laser. The pump laser beams have the frequencies $\omega_{p,i=1,2}$ and the wave-vectors $\mathbf{k}_p = k_{p,i=1,2}\mathbf{e}_y$. The difference between the two pump beam frequencies is chosen such $\hbar(\omega_{p,2} - \omega_{p,1}) \approx 2\Delta$. In the following we will use the rotating frame with the frequency $\omega_p = (\omega_{p,2} + \omega_{p,1})/2$ and $\lambda_p = \lambda_{p,1,(2)}$ as the wavelengths of the pump beams are approximately the same, i.e. $\lambda_{p,1} \approx \lambda_{p,2}$. The amplitude of the Raman process will be now $\hbar\tilde{\Omega} = \frac{\hbar\Omega_{p,1}g_0}{\omega_e - \omega_{p,1}}\phi_{\parallel}\phi_{\perp}$, where $\Omega_{p,i=1}$ is the Rabi frequencies of the first Raman beam, and the effective parameters $\phi_{\parallel}$ and $\phi_{\perp}$ contain contributions of the overlap of the wavefunctions from neighboring sites. The two Raman processes are balanced due to the choice of the Rabi frequency for the second pump beam $\Omega_{p,2} = \Omega_{p,1}\frac{\omega_e - \omega_{p,2}}{\omega_e - \omega_{p,1}}$. The modified Hamiltonian is given by

2.2 Derivation of the model

$$H = H_c + H_\parallel + H_{int} + H_{ac} \tag{2.20}$$

$$H_c = \hbar \delta_{cp} a^\dagger a$$

$$H_\parallel = -J_\parallel \sum_{j,m=0,1} (b^\dagger_{m,j} b_{m,j+1} + b^\dagger_{m,j+1} b_{m,j})$$

$$H_{int} = \frac{U}{2} \sum_{j,m=0,1} n_{m,j}(n_{m,j} - 1)$$

$$H_{ac} = -\hbar \tilde{\Omega}(a + a^\dagger)(K_\perp + K_\perp^\dagger)$$

$$K_\perp = \sum_j e^{i\varphi j} b^\dagger_{0,j} b_{1,j}.$$

As a short summary, the term H_c gives the dynamics of the cavity mode in the rotating frame. $H_\parallel$ describes the tunneling of the atoms along the legs of the ladder with the tunneling amplitude $J_\parallel$. The term H_{int} represents the repulsive on-site interaction of strength $U > 0$. The coupling between the atoms and the cavity field is described by H_{ac}, where a tunneling event along the rungs occurs by creation or annihilation of a cavity photon. The tunneling along the rungs with the spatially dependent phase imprint is represented by the operator $K_\perp$, coupled to both the creation and annihilation operators of the cavity field. L denotes the number of rungs of the ladder and the total number of bosons is N. The filling per site is defined as $\rho = N/(2L)$.

Beside the unitary dynamics given by the Hamiltonian (2.20), dissipative processes are present due to the imperfections of the cavity mirrors where losses of the cavity photons occur. The dissipative dynamics is approximated by a Lindblad master equation, which gives the evolution of the density matrix ρ

$$\frac{\partial}{\partial t}\rho = \frac{i}{\hbar}[H, \rho] + \mathcal{D}(\rho), \tag{2.21}$$

with the dissipator $\mathcal{D}(\rho) = \kappa \left(2a\rho a^\dagger - \rho a^\dagger a - a^\dagger a\rho\right)$, which gives the loss of cavity photons, via the imperfect mirrors [99]. In the derivation of the master equation one assumes the Markov approximation, namely the reservoir does not have memory. In our ultracold atoms coupled to the optical cavity system, the time scale of the dynamics, given by the cavity decay rate is much larger than the correlation time of the fluctuations from the reservoir, represented by the vac-

uum modes of the external electromagnetic field [99]. In this limit, the Markov approximation is valid.

2.3. Adiabatic elimination of the cavity field

In this section we will derive an effective model for the bosonic atoms, obtained from the adiabatic elimination of the cavity field [21, 93, 95, 98]. We approximate the expectation value of the cavity field with its steady state value, which fulfills the condition $\partial_t \langle a \rangle = 0$. The evolution of an operator O is given by

$$\frac{\partial}{\partial t} O = \frac{i}{\hbar} [H, O] + \mathcal{D}(O), \tag{2.22}$$

with the dissipator $\mathcal{D}(O) = \kappa \left(2a^\dagger O a - O a^\dagger a - a^\dagger a O \right)$.

Using Eq.(2.22) the condition for the cavity field is given by

$$i\partial_t \langle a \rangle = -\tilde{\Omega} \langle K_\perp + K_\perp^\dagger \rangle + (\delta_{cp} - i\kappa)\langle a \rangle = 0. \tag{2.23}$$

This condition relates the expectation value of the directed rung tunneling to the expectation value of the cavity field by

$$\alpha = \langle a \rangle = \frac{\tilde{\Omega}}{\delta_{cp} - i\kappa} \langle K_\perp + K_\perp^\dagger \rangle. \tag{2.24}$$

The Heisenberg equations of motion of the atomic operators read

$$i\hbar\partial_t \langle b_{0,j} \rangle = -J_\| \langle b_{0,j+1} + b_{0,j-1} \rangle - U \langle b_{0,j}(1 - n_{0,j}) \rangle$$
$$\qquad\qquad -\hbar\tilde{\Omega}\langle a + a^\dagger \rangle e^{i\varphi j} \langle b_{1,j} \rangle$$
$$i\hbar\partial_t \langle b_{1,j} \rangle = -J_\| \langle b_{1,j+1} + b_{1,j-1} \rangle - U \langle b_{1,j}(1 - n_{1,j}) \rangle$$
$$\qquad\qquad -\hbar\tilde{\Omega}\langle a + a^\dagger \rangle e^{-i\varphi j} \langle b_{0,j} \rangle. \tag{2.25}$$

In the derivation of the equations for the expectation values of the bosonic operators we have

2.3 Adiabatic elimination of the cavity field

used a mean-field decoupling of the atomic and cavity degrees of freedom, $\langle ab_{m,j}\rangle \approx \langle a\rangle\langle b_{m,j}\rangle$. The model exhibits a $\mathbb{Z}_2$ symmetry, associated with the inversion of the sign of both the cavity field, $a + a^\dagger$, and the rung tunneling, $K_\perp + K_\perp^\dagger$. In an experiment this symmetry will be spontaneously broken, thus we choose without loss of generality $\langle K_\perp + K_\perp^\dagger\rangle > 0$ and even find for the considered phases that we can choose $\langle K_\perp\rangle > 0$.

We substitute the expectation value for the cavity field, Eq. (2.24), into the equations of motion of the bosonic operators, Eq. (2.25) and obtain

$$
\begin{aligned}
i\hbar\partial_t\langle b_{0,j}\rangle &= -J_\parallel\langle b_{0,j+1} + b_{0,j-1}\rangle - U\langle b_{0,j}(1 - n_{0,j})\rangle \\
&\quad - \frac{2\hbar\tilde{\Omega}\delta_{cp}}{\delta_{cp}^2 + \kappa^2}\langle K_\perp + K_\perp^\dagger\rangle e^{i\varphi j}\langle b_{1,j}\rangle \\
i\hbar\partial_t\langle b_{1,j}\rangle &= -J_\parallel\langle b_{1,j+1} + b_{1,j-1}\rangle - U\langle b_{1,j}(1 - n_{1,j})\rangle \\
&\quad - \frac{2\hbar\tilde{\Omega}\delta_{cp}}{\delta_{cp}^2 + \kappa^2}\langle K_\perp + K_\perp^\dagger\rangle e^{-i\varphi j}\langle b_{0,j}\rangle.
\end{aligned}
\tag{2.26}
$$

The dynamics given by the obtained Eqs. (2.26) can be described by an effective Hamiltonian for the atoms. Here we neglect the dissipative term that would appear from substituting the expectation value for the cavity field into the dissipator $\mathcal{D}(\rho)$.

$$
\begin{aligned}
H &= H_\parallel + H_\perp + H_{int} \tag{2.27}\\
H_\parallel &= -J_\parallel \sum_{j,m=0,1} (b_{m,j}^\dagger b_{m,j+1} + b_{m,j+1}^\dagger b_{m,j}) \\
H_\perp &= -J_\perp (K_\perp + K_\perp^\dagger) \\
H_{int} &= \frac{U}{2} \sum_{j,m=0,1} n_{m,j}(n_{m,j} - 1)
\end{aligned}
$$

and typically the ground state is reached as a steady state of the coupled cavity-atomic system. The parameter $J_\perp$, which represents the rung tunneling amplitude, has to be determined self-consistently as it depends on the expectation value of the rung directed tunneling, $\langle K_\perp\rangle$, $J_\perp = A\langle K_\perp\rangle$, with the pump strength $A = \frac{4\hbar\tilde{\Omega}^2\delta_{cp}}{\delta_{cp}^2 + \kappa^2}$. Since $\langle K_\perp\rangle$ and $J_\perp$ have the same sign, a non-trivial solution ($\alpha \neq 0$) of the self-consistency condition requires $A > 0$, which implies $\delta_{cp} > 0$.

2.4. Stability analysis

The non-trivial self-consistent solution(s) derived from the effective Hamiltonian, Eq. (2.27), might not be stable. Thus, in this section we derive a stability condition for our model using pertubations around the steady state [21]. We use the notations introduced in Ref. [100] and follow the analysis we performed in Ref. [98].

Starting from the equation of motion for the cavity field, given by Eq. (2.23), we introduce the expectation values of the coordinate and momentum quadratures of the cavity field, $x_a = \langle a + a^\dagger \rangle$ and $p_a = -i\langle a - a^\dagger \rangle$. Using Eq. (2.23) and its hermitain conjugate we have

$$\frac{\partial}{\partial t} x_a = -\kappa x_a + \delta_{cp} p_a \tag{2.28}$$
$$\frac{\partial}{\partial t} p_a = -\delta_{cp} x_a - \kappa p_a + 4\tilde{\Omega}\langle K_\perp \rangle.$$

The stationary solutions of these equations, which satisfy the conditions $\partial_t x_a^{(s)} = 0$ and $\partial_t p_a^{(s)} = 0$ are

$$x_a^{(s)} = \frac{4\delta_{cp}\tilde{\Omega}\langle K_\perp \rangle^{(s)}}{\delta_{cp}^2 + \kappa^2}, \tag{2.29}$$
$$p_a^{(s)} = \kappa\delta_{cp}x_a^{(s)},$$

where the expectation value of the directed tunneling $\langle K_\perp \rangle$ is computed in the ground state of the effective model, Eq. (2.27), and can have a nonlinear dependence on the stationary coordinate quadrature $x_a^{(s)}$.

We will consider linear fluctuations around the stationary solutions, i.e., $x_a = x_a^{(s)} + \tilde{x}_a$ and $p_a = p_a^{(s)} + \tilde{p}_a$, and also linearize the expectation value of the directed tunneling in terms of the fluctuations

$$\langle K_\perp \rangle = \langle K_\perp \rangle^{(s)} + \frac{d\langle K_\perp \rangle^{(s)}}{dx_a^{(s)}} \tilde{x}_a \,, \tag{2.30}$$

where $\langle K_\perp \rangle^{(s)}$ is the value of the directed rung tunneling corresponding to the stationary solution $x_a^{(s)}$. From Eqs. (2.28) and (2.30) we can derive a set of differential equations for the

2.4 Stability analysis

fluctuations $\tilde{x}_a$ and $\tilde{p}_a$

$$\frac{\partial}{\partial t}\tilde{x}_a = -\kappa\tilde{x}_a + \delta_{cp}\tilde{p}_a \tag{2.31}$$
$$\frac{\partial}{\partial t}\tilde{p}_a = \left(-\delta_{cp} + 4\tilde{\Omega}\frac{d\langle K_\perp\rangle^{(s)}}{dx_a^{(s)}}\right)\tilde{x}_a - \kappa\tilde{p}_a.$$

The eigenvalues of the Jacobian of this set of differential equations are given by

$$\lambda_\pm = -\kappa \pm \sqrt{\left(-\delta_{cp}^2 + 4\delta_{cp}\tilde{\Omega}\frac{d\langle K_\perp\rangle^{(s)}}{dx_a^{(s)}}\right)}. \tag{2.32}$$

The stable stationary solutions are the ones for which the eigenvalues have a negative real part. Thus the stability condition for the system with $\delta_{cp} > 0$ is

$$\frac{\delta_{cp}^2 + \kappa^2}{4\delta_{cp}\tilde{\Omega}} > \frac{d\langle K_\perp\rangle^{(s)}}{dx_a^{(s)}}. \tag{2.33}$$

We can rewrite this condition in a form that we can use in our model with ease, using the relation $J_\perp^{(s)} = \hbar\tilde{\Omega}x_a^{(s)}$

$$\frac{d\langle K_\perp\rangle^{(s)}}{dJ_\perp^{(s)}} < \frac{1}{A}. \tag{2.34}$$

We can interpret the stability condition (Eq. (2.34)) by thinking about the effect of slightly increasing the pump strength $A \to A + dA$, with $dA > 0$. For a stable solution, which fulfills Eq. (2.34), the solution will shift to a point with a larger value of $\langle K_\perp\rangle$ and $J_\perp$. However if the stability condition is not fulfilled the solution corresponds now to a point with a smaller value of $\langle K_\perp\rangle$ and $J_\perp$. Thus if we increase the pump strength for a stable solution we increase the rung hopping amplitude and for an unstable solution we decrease the rung hopping amplitude.

3. Properties of the effective Hamiltonian

In this chapter we will investigate the properties of the effective Hamiltonian (Eq. 2.27) as a stand-alone model describing bosonic two-leg ladders with repulsive contact interaction in the presence of a uniform, external gauge field. In Sec. 3.1 we will look at the single-particle physics described by the Hamiltonian (2.27). In Sec. 3.2 we will derive a Bogoliubov theory for the weakly interacting bosons on the ladder under the magnetic flux. And in Sec. 3.3 we will briefly summarize the phases observed in the rich phase diagram explored by previous studies and introduce the observables used to identify these phases.

3.1. Non-interacting limit

In this section we will analyze the effective Hamiltonian (2.27) in the non-interacting limit, $U = 0$, in order to gain a better intuition of the low-energy physics of the system. In this limit the Hamiltonian becomes

$$H_0 = -J_\parallel \sum_{j,m=0,1} (b^\dagger_{m,j} b_{m,j+1} + b^\dagger_{m,j+1} b_{m,j}) - J_\perp \sum_j (e^{-i\varphi j} b^\dagger_{1,j} b_{0,j} + e^{i\varphi j} b^\dagger_{0,j} b_{1,j}). \qquad (3.1)$$

In the following we will diagonalize this Hamiltonian, by using a unitary transformation. But the first step is to go to momentum space by performing a Fourier transformation along the two legs of the ladder, which we define as

$$b_{m,kd_\parallel} = \frac{1}{\sqrt{L}} \sum_j e^{ikd_\parallel j} b_{m,j}, \qquad (3.2)$$

where L is the number of the rungs of the ladder, $d_\parallel$ the lattice spacing along the legs of the ladder, and $b_{m,k}$ are the bosonic annihilation operators in momentum space, satisfying the bosonic commutation relations $\left[b_{m,kd_\parallel}, b^\dagger_{m',k'd_\parallel} \right] = \delta_{m,m'} \delta_{k,k'}$. In the Fourier space the Hamiltonian (3.1) reads:

$$H_0 = -2J_\parallel \sum_{k,m=0,1} \cos\left(kd_\parallel\right) b^\dagger_{m,kd_\parallel} b_{m,kd_\parallel} - J_\perp \sum_k (b^\dagger_{1,kd_\parallel-\varphi/2} b_{0,kd_\parallel+\varphi/2} + b^\dagger_{0,kd_\parallel+\varphi/2} b_{1,kd_\parallel-\varphi/2}).$$

$$(3.3)$$

3.1 Non-interacting limit

We can observe that the parallel part of the Hamiltonian (3.3) is diagonal, but the perpendicular part couples states with different momenta. We diagonalize the Hamiltonian by performing the following unitary transformation [77, 101–104]

$$\gamma_{+,k} = v_k b_{0,kd_\parallel+\varphi/2} - u_k b_{1,kd_\parallel-\varphi/2},$$

$$\gamma_{-,k} = u_k b_{0,kd_\parallel+\varphi/2} + v_k b_{1,kd_\parallel-\varphi/2},$$

(3.4)

where $\gamma_{+,k}$ and $\gamma_{-,k}$ are the annihilation operator of the bosonic quasi-particles. From the bosonic commutation relations $\left[\gamma_{i,k}, \gamma_{i',k'}^\dagger\right] = \delta_{i,i'}\delta_{k,k'}$, with $i, i' = \pm$, and by imposing that the non-diagonal terms of the Hamiltonian vanish, we obtain the coefficients of the transformation

$$u_k^2 = \frac{1}{2}\left(1 + \frac{2\sin\left(kd_\parallel\right)\sin(\varphi/2)}{\sqrt{(J_\perp/J_\parallel)^2 + 4\sin\left(kd_\parallel\right)^2\sin(\varphi/2)^2}}\right),$$

(3.5)

$$v_k^2 = \frac{1}{2}\left(1 - \frac{2\sin\left(kd_\parallel\right)\sin(\varphi/2)}{\sqrt{(J_\perp/J_\parallel)^2 + 4\sin\left(kd_\parallel\right)^2\sin(\varphi/2)^2}}\right).$$

The diagonal form of the Hamiltonian is

$$H_0 = \sum_k \left(E_+(k)\gamma_{+,k}^\dagger\gamma_{+,k} + E_-(k)\gamma_{-,k}^\dagger\gamma_{-,k}\right).$$

(3.6)

The energy spectrum of the quasi-particles consists in two bands given by

$$\frac{E_\pm(k)}{J_\parallel} = -2\cos\left(kd_\parallel\right)\cos(\varphi/2) \pm \sqrt{(J_\perp/J_\parallel)^2 + 4\sin\left(kd_\parallel\right)^2\sin(\varphi/2)^2}.$$

(3.7)

We have plotted the two energy bands in Fig. 3.1 for different values of the rung tunneling amplitude $J_\perp$ and the magnetic flux φ.

We can observe from Fig. 3.1(a)-(c) that for $J_\perp$, the legs of the ladder are not coupled, the two bands are shaped like two cosine functions, shifted by the quasimomentum $\pm\frac{\varphi}{2d_\parallel}$, which cross at $k = 0$ and at the edges of the Brillouin zone. By increasing the value of the rung tunneling amplitude (see Fig. 3.1(d)-(i)), the curvature of the bands decreases and the two minima
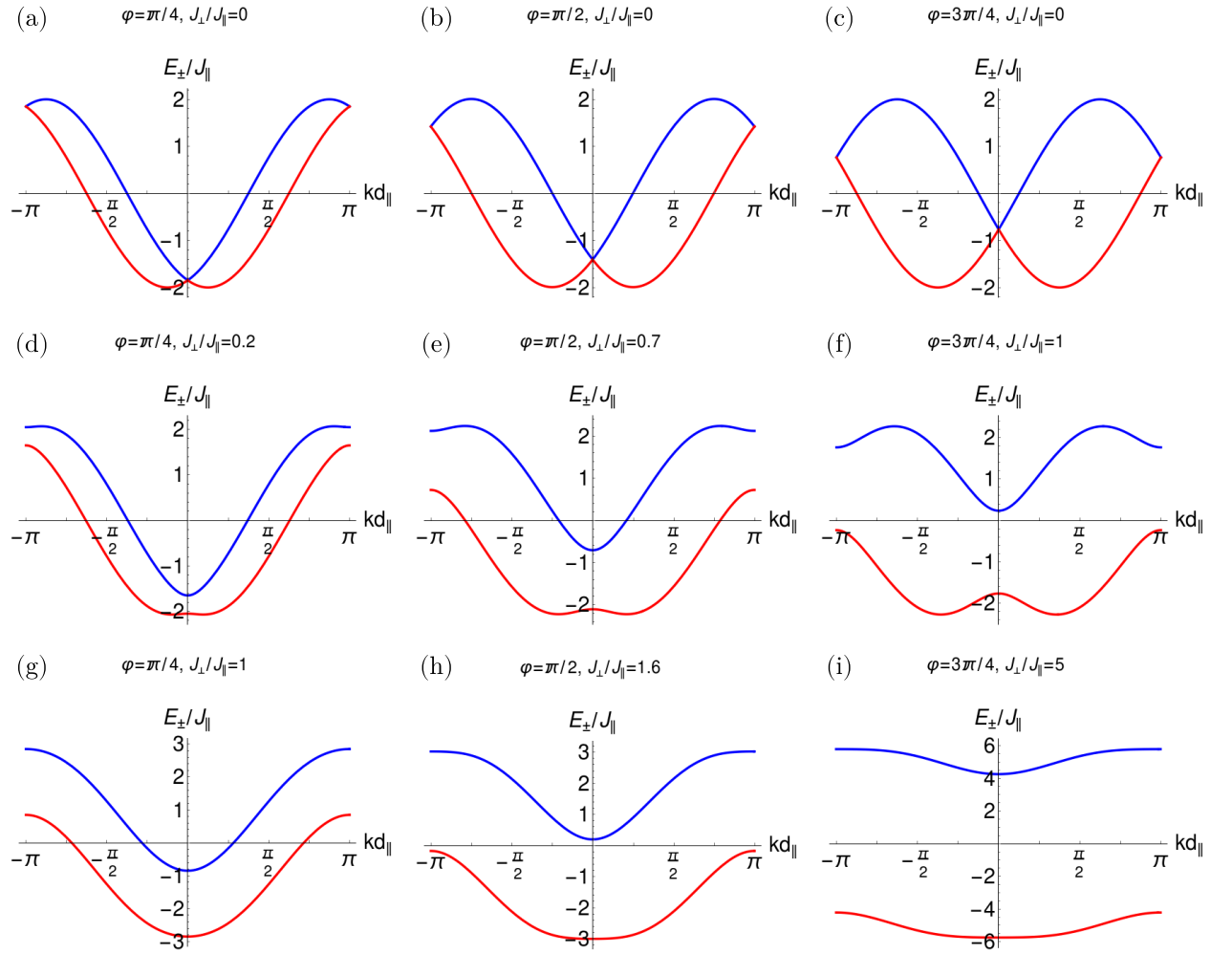
Figure 3.1.: The quasi-particle energy bands $E_+(k)$ (red line) and $E_-(k)$ (blue line) for three values of the magnetic flux $\varphi = \frac{\pi}{4}, \frac{\pi}{2}, \frac{3\pi}{4}$, and several values of the rung tunneling amplitude $J_\perp$. As the energy bands reflect only the single particle physics, they are the same with the ones obtained in the fermionic case in Ref. [95]

move towards smaller values of the quasimomentum. Above a critical value of $J_\perp$ the minima merge into one minimum situated at $k = 0$ (Fig. 3.1(g)-(i)). Also, the increasing of the value of $J_\perp$ leads to a splitting of the energy band crossing into avoided crossings, thus for $J_\perp/J_\parallel < 2|\cos(\varphi/2)|$ the two bands overlap in energy, but for $J_\perp/J_\parallel > 2|\cos(\varphi/2)|$ the two energy bands are separated by an energy gap. If we look at the extrema of the lower bands we see that for $J_\perp/J_\parallel < 2|\sin(\varphi/2)\tan(\varphi/2)|$ the band has two minima (e.g. Fig. 3.1(f)), which are located at

$$k_\pm = \pm\frac{1}{d_\parallel}\arccos\left(\sqrt{(J_\perp/2J_\parallel)^2\cot(\varphi/2)^2 + \cos(\varphi/2)^2}\right). \tag{3.8}$$

In contrast, for $J_\perp/J_\parallel > 2|\sin(\varphi/2)\tan(\varphi/2)|$ only one minimum at the quasimomentum $k = 0$ exists.

3.2. Weakly interacting bosons

In this section we will consider the full Hamiltonian (2.27), for small values of the interaction strength U. We will describe the ground state of the system and the excitations on top of the ground state, using the perturbation technique, known as Bogoliubov theory. We will start by describing the general framework of a 3-dimensional Bose-Einstein condensate with weak interactions [105] in Sec. 3.2.1, and then proceed to apply the Bogoliubov theory for the ladder, system in Sec. 3.2.2 and Sec. 3.2.3.

3.2.1. General framework

The Hamiltonian for an interacting bosonic gas, without any external potentials, in momentum space reads [105]

$$H = \sum_{\mathbf{p}} \frac{p^2}{2m} a_{\mathbf{p}}^\dagger a_{\mathbf{p}} + \frac{g}{2V} \sum_{\mathbf{p}_1,\mathbf{p}_2,\mathbf{q}} a_{\mathbf{p}_1+\mathbf{q}}^\dagger a_{\mathbf{p}_2-\mathbf{q}}^\dagger a_{\mathbf{p}_1} a_{\mathbf{p}_2} \tag{3.9}$$

where $a_{\mathbf{p}}$ is the annihilation operator for a particle with the momentum $\mathbf{p}$. We considered the interaction parameter of the form $g = \frac{4\pi\hbar a}{m}$, with a is the s-wave scattering length, which characterizes all the effects of the interaction in the gas. We neglect all the configuration where three or more particles are interacting simultaneously, by imposing a diluteness condition. In order for a gas to be considered dilute, the gas parameter $n|a^3|$ should be very small, $n|a^3| \ll 1$,

where $n = N/V$ is the density of the gas.

The Bogoliubov prescription for obtaining the ground state energy consists in, firstly, ignoring all contributions from momenta $\mathbf{p} \neq 0$ and replacing the operator a_0 with a complex number, $a_0 = \sqrt{N_0}$. Where, N_0 is the number of atoms in the condensate. In an non-interacting gas, at $T = 0$, all the atoms would be in the condensate, $N_0 = N$. In this approximation the ground state energy is given by $E_0 = \frac{1}{2}Nng$.

Furthermore, in order to obtain the excitation spectrum on top of the condensate, one needs to consider higher-order terms. Thus, from the Hamiltonian (3.9) we retain only the quadratic terms in the particle operators with $\mathbf{p} \neq 0$, we do not have any linear terms due to momentum conservation.

$$H = \frac{g}{2V}a_0^\dagger a_0^\dagger a_0 a_0 + \sum_{\mathbf{p}} \frac{p^2}{2m}a_{\mathbf{p}}^\dagger a_{\mathbf{p}} + \frac{g}{2V}\sum_{\mathbf{p}\neq 0}\left(4a_0^\dagger a_{\mathbf{p}}^\dagger a_0 a_{\mathbf{p}} + a_{\mathbf{p}}^\dagger a_{-\mathbf{p}}^\dagger a_0 a_0 + a_0^\dagger a_0^\dagger a_{\mathbf{p}} a_{-\mathbf{p}}\right) \quad (3.10)$$

Next, we will replace the operators $a_0^\dagger$ and a_0 with $\sqrt{N}$, but in the first term of Eq. (3.10), we need to work with higher accuracy. Thus, by using the normalization condition $a_0^\dagger a_0 + \sum_{\mathbf{p}\neq 0} a_{\mathbf{p}}^\dagger a_{\mathbf{p}} = N$ and neglecting higher-order terms we obtain

$$a_0^\dagger a_0^\dagger a_0 a_0 = N^2 - N\sum_{\mathbf{p}\neq 0} a_{\mathbf{p}}^\dagger a_{\mathbf{p}} \quad (3.11)$$

Substituting everything back into Eq. (3.10), we obtain the following quadratic Hamiltonian

$$H = \frac{g}{2V}N^2 + \sum_{\mathbf{p}} \frac{p^2}{2m}a_{\mathbf{p}}^\dagger a_{\mathbf{p}} + \frac{1}{2}gn\sum_{\mathbf{p}\neq 0}\left(2a_{\mathbf{p}}^\dagger a_{\mathbf{p}} + a_{\mathbf{p}}^\dagger a_{-\mathbf{p}}^\dagger + a_{\mathbf{p}}a_{-\mathbf{p}}\right) \quad (3.12)$$

This Hamiltonian can be diagonalized by the means of a Bogoliubov transformation, which is a linear transformation of the form

$$a_{\mathbf{p}} = u_{\mathbf{p}}b_{\mathbf{p}} + v_{-\mathbf{p}}^* b_{-\mathbf{p}}^\dagger, \quad (3.13)$$
$$a_{\mathbf{p}}^\dagger = u_{\mathbf{p}}^* b_{\mathbf{p}}^\dagger + v_{-\mathbf{p}}b_{-\mathbf{p}}.$$

3.2 Weakly interacting bosons

This transformation introduces a new set of operators, $b_{\mathbf{p}}$ and $b_{\mathbf{p}}^{\dagger}$, for quasi-particles representing the collective excitations. We impose for these operators the bosonic commutation relations, $\left[b_{\mathbf{p}}, b_{\mathbf{p}'}^{\dagger} \right] = \delta_{\mathbf{p},\mathbf{p}'}$. The commutation relations are satisfied if

$$|u_{\mathbf{p}}|^2 - |v_{-\mathbf{p}}|^2 = 1 \tag{3.14}$$

If we perform the transformation (3.13) of the Hamiltonian (3.12) and we impose the non-diagonal terms $b_{\mathbf{p}}b_{\mathbf{p}}$ and $b_{-\mathbf{p}}b_{-\mathbf{p}}$ to vanish, we obtain the following condition for the coefficients of the transformation

$$\frac{gn}{2}\left(|u_{\mathbf{p}}|^2 + |v_{-\mathbf{p}}|^2\right) + \left(\frac{p^2}{2m} + gn\right)u_{\mathbf{p}}v_{-\mathbf{p}} = 0. \tag{3.15}$$

We can solve the Eqs. (3.14) and (3.15) and obtain the expression of the coefficients $u_{\mathbf{p}}$ and $v_{\mathbf{p}}$

$$u_{\mathbf{p}}, v_{-\mathbf{p}} = \pm\sqrt{\frac{p^2/2m + gn}{2\epsilon(p)} \pm \frac{1}{2}}, \tag{3.16}$$

where $\epsilon(p)$ is defined by

$$\epsilon(p) = \sqrt{\frac{gn}{m}p^2 + \left(\frac{p^2}{2m}\right)^2}. \tag{3.17}$$

Knowing the form of the coefficients, by performing the Bogoliubov transformation, the Hamiltonian (3.12) can be reduced to the diagonal form

$$H = E_0 + \sum_{\mathbf{p}} \epsilon(p)b_{\mathbf{p}}^{\dagger}b_{\mathbf{p}}, \tag{3.18}$$

with the ground state energy

$$E_0 = \frac{g}{2V}N^2 + \frac{1}{2}\sum_{\mathbf{p}\neq 0}\left(\epsilon(p) - gn - \frac{p^2}{2m}\right). \tag{3.19}$$

Thus it has been shown [105] that the original system of weakly-interacting bosons can be described in terms of independent quasi-particles with the energy spectrum $\epsilon(p)$.

3.2.2. Bogoliubov spectra

In this section we aim at performing the same type of excitations over a mean-field approxima-tion as described in the previous section for the ladder system, described by the Hamiltonian (2.27). We distinguish two cases, based on the shape of the lower energy band of the non-interacting system, in the case with just one minimum the bosons will condense at $k = 0$ and the expansion will resemble the one we have seen before in Sec. 3.2.1. In the case of two minima, we will have to distinguish between the situation with two distinct condensates at each mini-mum and only one condensate in one of the minima. But first, we make a gauge transformation which simplifies the further calculations

$$
b_{0,j} \to b_{0,j} e^{ij\varphi/2}, \tag{3.20}
$$
$$
b_{1,j} \to b_{1,j} e^{-ij\varphi/2}.
$$

By making this transformation, the phase imprint will be realized while the atoms are hopping on the y-direction and the Hamiltonian (2.27) becomes

$$
H = H_\parallel + H_\perp + H_{int} \tag{3.21}
$$
$$
H_\parallel = -J_\parallel \sum_j \left(b_{0,j}^\dagger b_{0,j+1} e^{i\varphi/2} + b_{1,j}^\dagger b_{1,j+1} e^{-i\varphi/2} + h.c. \right)
$$
$$
H_\perp = -J_\perp \sum_j \left(b_{1,j}^\dagger b_{0,j} + h.c. \right)
$$
$$
H_{int} = \frac{U}{2} \sum_{j,m=0,1} n_{m,j}(n_{m,j} - 1)
$$

The unitary transformation (3.4) that we used in order to diagonalize the kinetic part, in Sec. 3.1, will be slightly modified under this gauge transformation and it becomes

$$
\gamma_{+,k} = v_k b_{0,kd_\parallel} - u_k b_{1,kd_\parallel}, \tag{3.22}
$$
$$
\gamma_{-,k} = u_k b_{0,kd_\parallel} + v_k b_{1,kd_\parallel},
$$

3.2 Weakly interacting bosons

where the coefficients u_k and v_k are the same as before

$$
u_k^2 = \frac{1}{2} \left(1 + \frac{2 \sin\left(kd_\parallel\right) \sin(\varphi/2)}{\sqrt{(J_\perp/J_\parallel)^2 + 4 \sin\left(kd_\parallel\right)^2 \sin(\varphi/2)^2}} \right),
$$

$$
v_k^2 = \frac{1}{2} \left(1 - \frac{2 \sin\left(kd_\parallel\right) \sin(\varphi/2)}{\sqrt{(J_\perp/J_\parallel)^2 + 4 \sin\left(kd_\parallel\right)^2 \sin(\varphi/2)^2}} \right).
$$

(3.23)

In order to be able to perform the expansion around the minima, we need to rewrite the Hamiltonian (3.21) in the basis of quasi-particle operators $\{\gamma_+, \gamma_-\}$. The kinetic part becomes diagonal under this transformation, but the interaction term, which is of the form $\sum_{k_1,k_2,q} b^\dagger_{k_1+q} b^\dagger_{k_2-q} b_{k_1} b_{k_2}$ in momentum space, will be more intricate. As we are interested in the excitations near the condensate ground state, we neglect the terms which are more than quadratic in the operator γ_+, corresponding to the upper band. Thus the transformation of the Hamiltonian (3.21) yields

$$
H = \sum_k \left(E_+(k)\gamma^\dagger_{+,k}\gamma_{+,k} + E_-(k)\gamma^\dagger_{-,k}\gamma_{-,k} \right)
$$
$$
+ \frac{U}{2L} \sum_{k_1,k_2,q} [(a) + (b) + (c) + (d) + (e) + (f) + (g) + (h)],
$$

(3.24)

where the interaction terms are listed in the following

$$(a) \equiv \left(\gamma^\dagger_{+,k_1+q}\gamma^\dagger_{+,k_2-q}\gamma_{-,k_1}\gamma_{-,k_2} + \gamma^\dagger_{-,k_1+q}\gamma^\dagger_{-,k_2-q}\gamma_{+,k_1}\gamma_{+,k_2}\right) \tag{3.25}$$
$$\times \left(u_{k_1+q}u_{k_2-q}v_{k_1}v_{k_2} + v_{k_1+q}v_{k_2-q}u_{k_1}u_{k_2}\right),$$

$$(b) \equiv \left(\gamma^\dagger_{+,k_1+q}\gamma^\dagger_{-,k_2-q}\gamma_{+,k_1}\gamma_{-,k_2} + \gamma^\dagger_{-,k_1+q}\gamma^\dagger_{+,k_2-q}\gamma_{-,k_1}\gamma_{+,k_2}\right)$$
$$\times \left(u_{k_1+q}v_{k_2-q}u_{k_1}v_{k_2} + v_{k_1+q}u_{k_2-q}v_{k_1}u_{k_2}\right),$$

$$(c) \equiv \left(\gamma^\dagger_{+,k_1+q}\gamma^\dagger_{-,k_2-q}\gamma_{-,k_1}\gamma_{+,k_2} + \gamma^\dagger_{-,k_1+q}\gamma^\dagger_{+,k_2-q}\gamma_{+,k_1}\gamma_{-,k_2}\right)$$
$$\times \left(u_{k_1+q}v_{k_2-q}v_{k_1}u_{k_2} + v_{k_1+q}u_{k_2-q}u_{k_1}v_{k_2}\right),$$

$$(d) \equiv \left(\gamma^\dagger_{+,k_1+q}\gamma^\dagger_{-,k_2-q}\gamma_{-,k_1}\gamma_{-,k_2}\right) \times \left(v_{k_1+q}u_{k_2-q}u_{k_1}u_{k_2} - u_{k_1+q}v_{k_2-q}v_{k_1}v_{k_2}\right),$$

$$(e) \equiv \left(\gamma^\dagger_{-,k_1+q}\gamma^\dagger_{+,k_2-q}\gamma_{-,k_1}\gamma_{-,k_2}\right) \times \left(u_{k_1+q}v_{k_2-q}u_{k_1}u_{k_2} - v_{k_1+q}u_{k_2-q}v_{k_1}v_{k_2}\right),$$

$$(f) \equiv \left(\gamma^\dagger_{-,k_1+q}\gamma^\dagger_{-,k_2-q}\gamma_{+,k_1}\gamma_{-,k_2}\right) \times \left(u_{k_1+q}u_{k_2-q}v_{k_1}u_{k_2} - v_{k_1+q}v_{k_2-q}u_{k_1}v_{k_2}\right),$$

$$(g) \equiv \left(\gamma^\dagger_{-,k_1+q}\gamma^\dagger_{-,k_2-q}\gamma_{-,k_1}\gamma_{+,k_2}\right) \times \left(u_{k_1+q}u_{k_2-q}u_{k_1}v_{k_2} - v_{k_1+q}v_{k_2-q}v_{k_1}u_{k_2}\right),$$

$$(h) \equiv \left(\gamma^\dagger_{-,k_1+q}\gamma^\dagger_{-,k_2-q}\gamma_{-,k_1}\gamma_{-,k_2}\right) \times \left(u_{k_1+q}u_{k_2-q}u_{k_1}u_{k_2} - v_{k_1+q}v_{k_2-q}v_{k_1}v_{k_2}\right).$$

3.2.2.1. One minimum case

Firstly, we will consider the case when the non-interacting lower energy band has only one minimum at $k = 0$. In this case, the rung tunneling amplitude satisfies the following inequality $J_\perp/J_\parallel > 2|\sin(\varphi/2)\tan(\varphi/2)|$. We assume that at $T = 0$ only the mode $\gamma_{-,k=0}$ is macroscopically occupied, and we will retain the operators $\gamma_{+,k}$ and $\gamma_{-,k\neq0}$ only up to second order in the expansion of the Hamiltonian (3.24). Using the facts $u_0^2 = v_0^2 = 1/2$ and $u_{-k} = v_k$ the interaction terms (3.25) can be approximated by

3.2 Weakly interacting bosons

$$\sum_{k_1,k_2,q} (a) \approx \sum_{k} u_k v_k \left(\gamma^\dagger_{+,k} \gamma^\dagger_{+,-k} \gamma_{-,0} \gamma_{-,0} + \gamma^\dagger_{-,0} \gamma^\dagger_{-,0} \gamma_{+,k} \gamma_{+,-k} \right) \qquad (3.26)$$

$$\sum_{k_1,k_2,q} (b) \approx \sum_{k} \gamma^\dagger_{+,k} \gamma^\dagger_{-,0} \gamma_{+,k} \gamma_{-,0}$$

$$\sum_{k_1,k_2,q} (c) \approx \sum_{k} \gamma^\dagger_{+,k} \gamma^\dagger_{-,0} \gamma_{+,k} \gamma_{-,0}$$

$$\sum_{k_1,k_2,q} (d) \approx \frac{1}{2} \sum_{k \neq 0} \left(v_k^2 - u_k^2 \right) \gamma^\dagger_{+,k} \gamma^\dagger_{-,-k} \gamma_{-,0} \gamma_{-,0}$$

$$\sum_{k_1,k_2,q} (e) \approx \frac{1}{2} \sum_{k \neq 0} \left(v_k^2 - u_k^2 \right) \gamma^\dagger_{-,-k} \gamma^\dagger_{+,k} \gamma_{-,0} \gamma_{-,0}$$

$$\sum_{k_1,k_2,q} (f) \approx \frac{1}{2} \sum_{k \neq 0} \left(v_k^2 - u_k^2 \right) \gamma^\dagger_{-,0} \gamma^\dagger_{-,0} \gamma_{+,k} \gamma_{-,-k}$$

$$\sum_{k_1,k_2,q} (g) \approx \frac{1}{2} \sum_{k \neq 0} \left(v_k^2 - u_k^2 \right) \gamma^\dagger_{-,0} \gamma^\dagger_{-,0} \gamma_{-,-k} \gamma_{+,k}$$

$$\sum_{k_1,k_2,q} (h) \approx \frac{1}{2} \sum_{k \neq 0} \left[2 \gamma^\dagger_{-,0} \gamma^\dagger_{-,k} \gamma_{-,0} \gamma_{-,k} + u_k v_k \left(\gamma^\dagger_{-,k} \gamma^\dagger_{-,-k} \gamma_{-,0} \gamma_{-,0} + \gamma^\dagger_{-,0} \gamma^\dagger_{-,0} \gamma_{-,-k} \gamma_{-,k} \right) \right]$$

$$+ \frac{1}{2} \gamma^\dagger_{-,0} \gamma^\dagger_{-,0} \gamma_{-,0} \gamma_{-,0}$$

In this approximation the Hamiltonian (3.24) becomes

$$H = \sum_{k} \left(E_+(k) \gamma^\dagger_{+,k} \gamma_{+,k} + E_-(k) \gamma^\dagger_{-,k} \gamma_{-,k} \right) \qquad (3.27)$$

$$+ \frac{U}{2L} \sum_{k} u_k v_k \left(\gamma^\dagger_{+,k} \gamma^\dagger_{+,-k} \gamma_{-,0} \gamma_{-,0} + \gamma^\dagger_{-,0} \gamma^\dagger_{-,0} \gamma_{+,k} \gamma_{+,-k} \right)$$

$$+ \frac{U}{L} \sum_{k} \left(\gamma^\dagger_{+,k} \gamma^\dagger_{-,0} \gamma_{+,k} \gamma_{-,0} + \gamma^\dagger_{-,k} \gamma^\dagger_{-,0} \gamma_{-,k} \gamma_{-,0} \right)$$

$$+ \frac{U}{2L} \sum_{k} \left(v_k^2 - u_k^2 \right) \left(\gamma^\dagger_{+,k} \gamma^\dagger_{-,-k} \gamma_{-,0} \gamma_{-,0} + \gamma^\dagger_{-,0} \gamma^\dagger_{-,0} \gamma_{+,k} \gamma_{-,-k} \right)$$

$$+ \frac{U}{2L} \sum_{k \neq 0} u_k v_k \left(\gamma^\dagger_{-,k} \gamma^\dagger_{-,-k} \gamma_{-,0} \gamma_{-,0} + \gamma^\dagger_{-,0} \gamma^\dagger_{-,0} \gamma_{-,k} \gamma_{-,-k} \right)$$

$$+ \frac{U}{4L} \gamma^\dagger_{-,0} \gamma^\dagger_{-,0} \gamma_{-,0} \gamma_{-,0}$$

As described in Sec. 3.2.1, we will use the Bogoliubov prescription and replace the operators $\gamma^\dagger_{-,0}$ and $\gamma_{-,0}$ with the complex number $\sqrt{N_0} \approx \sqrt{N}$. Again for the last term from Eq. 3.27 we will use the normalization condition $\gamma^\dagger_{-,0}\gamma_{-,0} + \sum_{k \neq 0} \gamma^\dagger_{-,k}\gamma_{-,k} + \sum_k \gamma^\dagger_{+,k}\gamma_{+,k} = N$ and by neglecting higher-order terms we obtain

$$\gamma^\dagger_{-,0}\gamma^\dagger_{-,0}\gamma_{-,0}\gamma_{-,0} = N^2 - 2N\left(\sum_{k \neq 0} \gamma^\dagger_{-,k}\gamma_{-,k} + \sum_k \gamma^\dagger_{+,k}\gamma_{+,k} \right). \tag{3.28}$$

After performing these substitutions and changing the summation interval from $k \in (-\pi, \pi)$ to $k \in (0, \pi)$ the resulting quadratic Hamiltonian reads

$$\begin{aligned}
H = H_0 &+ \sum_{k>0} \left(E_-(k) + \frac{1}{2}Un \right) \left(\gamma^\dagger_{-,k}\gamma_{-,k} + \gamma^\dagger_{-,-k}\gamma_{-,-k} \right) \\
&+ \sum_{k \geq 0} \left(E_+(k) + \frac{1}{2}Un \right) \left(\gamma^\dagger_{+,k}\gamma_{+,k} + \gamma^\dagger_{+,-k}\gamma_{+,-k} \right) \\
&+ Un \sum_{k \geq 0} u_k v_k \left(\gamma^\dagger_{+,k}\gamma^\dagger_{+,-k} + \gamma_{+,k}\gamma_{+,-k} \right) \\
&+ Un \sum_{k \geq 0} u_k v_k \left(\gamma^\dagger_{-,k}\gamma^\dagger_{-,-k} + \gamma_{-,k}\gamma_{-,-k} \right) \\
&+ Un \sum_{k \geq 0} \left(v_k^2 - u_k^2 \right) \left(\gamma^\dagger_{+,k}\gamma^\dagger_{-,-k} - \gamma^\dagger_{+,-k}\gamma^\dagger_{-,k} + \gamma_{+,k}\gamma_{-,-k} - \gamma_{+,-k}\gamma_{-,k} \right),
\end{aligned} \tag{3.29}$$

where we have defined the one-dimensional density $n = N/L$.

Before proceeding with the diagonalization of the Hamiltonian (3.29), we must shift the non-interacting spectrum such that the minimum coresponds to zero energy [106, 107]. This means that we add a chemical potential term in the Hamiltonian

$$H' = H + \mu \sum_{k>0} \left(\gamma^\dagger_{-,k}\gamma_{-,k} + \gamma^\dagger_{-,-k}\gamma_{-,-k} \right) + \mu \sum_{k \geq 0} \left(\gamma^\dagger_{+,k}\gamma_{+,k} + \gamma^\dagger_{+,-k}\gamma_{+,-k} \right). \tag{3.30}$$

with $\mu = -E_-(0)$. Thus, we have $E'_-(k = 0) = E_-(k = 0) + \mu = 0$, and the shifted non-interacting energy bands are

3.2 Weakly interacting bosons

$$E'_{\pm}(k) = E_{\pm}(k) + \mu \tag{3.31}$$

$$= -2J_{\parallel}\cos\left(kd_{\parallel}\right)\cos(\varphi/2) \pm \sqrt{J_{\perp}^2 + 4J_{\parallel}^2\sin\left(kd_{\parallel}\right)^2\sin(\varphi/2)^2} + 2J_{\parallel}\cos(\varphi/2) + J_{\perp}.$$

For simplicity, from now on we use $E_{\pm}(k)$ instead of the shifted energies $E'_{\pm}(k)$.

In the following we will continue with the diagonalization of the quadratic Hamiltonian (3.29). First, we rewrite the Hamiltonian as

$$H = \sum_k \left[\sum_{i,j} A_{k;i,j} a^{\dagger}_{k;i} a_{k;j} + \frac{1}{2}\sum_{i,j}\left(B_{k;i,j}a^{\dagger}_{k;i}a^{\dagger}_{k;j} + B_{k;i,j}a_{k;i}a_{k;j}\right) \right], \tag{3.32}$$

where the constant term H_0 is not considered for now. A_k and B_k are the following matrices

$$A_k = \begin{pmatrix} E_-(k) + \frac{1}{2}Un & 0 & 0 & 0 \\ 0 & E_-(k) + \frac{1}{2}Un & 0 & 0 \\ 0 & 0 & E_+(k) + \frac{1}{2}Un & 0 \\ 0 & 0 & 0 & E_+(k) + \frac{1}{2}Un \end{pmatrix}, \tag{3.33}$$

$$B_k = \begin{pmatrix} 0 & Unu_kv_k & 0 & -\frac{1}{2}Un(v_k^2 - u_k^2) \\ Unu_kv_k & 0 & \frac{1}{2}Un(v_k^2 - u_k^2) & 0 \\ 0 & \frac{1}{2}Un(v_k^2 - u_k^2) & 0 & Unu_kv_k \\ -\frac{1}{2}Un(v_k^2 - u_k^2) & 0 & Unu_kv_k & 0 \end{pmatrix},$$

and the vector $a_k = (\gamma_{-,k}, \gamma_{-,-k}, \gamma_{+,k}, \gamma_{+,-k})^t$. Now we can rewrite the Hamiltonian into a matrix notation

$$H = \sum_{k>0} H_k, \tag{3.34}$$

$$H_k = \frac{1}{2}\alpha_k^{\dagger}M_k\alpha_k - \frac{1}{2}Tr(A_k),$$

with $\alpha_k = \left(a_k^t, a_k^{\dagger}\right)^t = \left(\gamma_{-,k}, \gamma_{-,-k}, \gamma_{+,k}, \gamma_{+,-k}, \gamma_{-,k}^{\dagger}, \gamma_{-,-k}^{\dagger}, \gamma_{+,k}^{\dagger}, \gamma_{+,-k}^{\dagger}\right)^t$ and

$$M_k = \begin{pmatrix} A_k & B_k \\ B_k & A_k \end{pmatrix}. \tag{3.35}$$

The diagonalization of the Hamiltonian (3.34) consists in finding the linear canonical transformation which defines the quasi-particles operators $d_k = T_k \alpha_k$, such that the bosonic commutation relations are fulfilled by the new operators d_k [108, 109]. In order to preserve the bosonic commutation relations, one needs to diagonalize the matrix ηM_k, where

$$\eta = \begin{pmatrix} 1 & 0 \\ 0 & -1 \end{pmatrix}, \tag{3.36}$$

$$\eta M_k = \begin{pmatrix} A_k & B_k \\ -B_k & -A_k \end{pmatrix}.$$

In terms of the quasi-particle operators the Hamiltonian reads

$$H = \frac{1}{2} \sum_{k>0} d_k^\dagger \eta T_k \eta M_k T_k^{-1} d_k - \frac{1}{2} \sum_{k>0} Tr(A_k). \tag{3.37}$$

The transformation given by the matrix T_k brings the Hamiltonian into a diagonal form, such that $T_k \eta M_k T_k^{-1} = \Omega_k$, where Ω_k is the diagonal matrix

$$\Omega_k = \begin{pmatrix} \omega_k & 0 \\ 0 & -\omega_k \end{pmatrix}, \tag{3.38}$$

where ω_k is a 4×4 diagonal matrix, with the eigenenergies of the Hamiltonian on the diagonal. Due to the structure of the matrix ηM_k, its eigenvalues appear in pairs of the form $(\omega_{k;i}, -\omega_{k;i})$ [108, 109]. Thus we can write the Hamiltonian as in the case of non-interacting quasi-particles

$$H = \frac{1}{2} \sum_{k>0} d_k^\dagger \eta \Omega_k d_k - \frac{1}{2} \sum_{k>0} Tr(A_k). \tag{3.39}$$

Let $d_k^\dagger = \left(d_{1,k}^\dagger, d_{1,-k}^\dagger, d_{2,k}^\dagger, d_{2,-k}^\dagger, d_{1,k}, d_{1,-k}, d_{2,k}, d_{2,-k} \right)$, then equation (3.39) becomes

3.2 Weakly interacting bosons

$$H = H_0 - \sum_{k>0} \left(E_-(k) + E_+(k) + Un \right) + \sum_{k>0} \left(E_1(k) + E_2(k) \right) \tag{3.40}$$
$$+ \sum_{k \neq 0} \left(E_1(k) d_{1,k}^\dagger d_{1,k} + E_2(k) d_{2,k}^\dagger d_{2,k} \right).$$

where the constant term H_0 from Eq. (3.29) is included, and the ground state energy is given by

$$E_0 = \frac{U}{4L} N^2 - \sum_{k>0} \left(E_-(k) + E_+(k) + Un \right) + \sum_{k>0} \left(E_1(k) + E_2(k) \right). \tag{3.41}$$

The energy spectrum of the quasi-particles consists in two bands given by

$$E_{1,2}^2 = \frac{1}{2} \left(E_-^2 + E_+^2 + (E_- + E_+)nU \right) \tag{3.42}$$
$$\pm \frac{1}{2} \sqrt{(E_- - E_+)^2 ((E_- + E_+)(E_- + E_+ + 2nU) + n^2 U^2 (1 - (v_k^2 - u_k^2)^2))}.$$

The transformation between the γ_k basis and the d_k basis reads

$$\begin{pmatrix} d_{1,k} \\ d_{1,-k} \\ d_{2,k} \\ d_{2,-k} \\ d_{1,k}^\dagger \\ d_{1,-k}^\dagger \\ d_{2,k}^\dagger \\ d_{2,-k}^\dagger \end{pmatrix} = T_k \begin{pmatrix} \gamma_{-,k} \\ \gamma_{-,-k} \\ \gamma_{+,k} \\ \gamma_{+,-k} \\ \gamma_{-,k}^\dagger \\ \gamma_{-,-k}^\dagger \\ \gamma_{+,k}^\dagger \\ \gamma_{+,-k}^\dagger \end{pmatrix}, \tag{3.43}$$

with T_k of the form

$$T_k = \begin{pmatrix} x_{1,k} & 0 & x_{2,k} & 0 & 0 & -x_{3,k} & 0 & -x_{4,k} \\ 0 & x_{1,-k} & 0 & x_{2,-k} & -x_{3,-k} & 0 & -x_{4,-k} & 0 \\ x_{5,k} & 0 & x_{6,k} & 0 & 0 & -x_{7,k} & 0 & -x_{8,k} \\ 0 & x_{5,-k} & 0 & x_{6,-k} & -x_{7,-k} & 0 & -x_{8,-k} & 0 \\ 0 & -x_{3,k} & 0 & -x_{4,k} & x_{1,k} & 0 & x_{2,k} & 0 \\ -x_{3,-k} & 0 & -x_{4,-k} & 0 & 0 & x_{1,-k} & 0 & x_{2,-k} \\ 0 & -x_{7,k} & 0 & -x_{8,k} & x_{5,k} & 0 & x_{6,k} & 0 \\ -x_{7,-k} & 0 & -x_{8,-k} & 0 & 0 & x_{5,-k} & 0 & x_{6,-k} \end{pmatrix}. \tag{3.44}$$

In order to have the bosonic commutation relations fulfilled, $\left[d_{i,k}, d_{j,k'}^{\dagger}\right] = \delta_{i,j}\delta_{k,k'}$, the coefficients of the transformation T_k have to satisfy the following relations

$$x_{1,k}^2 + x_{2,k}^2 - x_{3,k}^2 - x_{4,k}^2 = 1, \tag{3.45}$$
$$x_{5,k}^2 + x_{6,k}^2 - x_{7,k}^2 - x_{8,k}^2 = 1,$$
$$x_{1,k}x_{5,k} + x_{2,k}x_{6,k} - x_{3,k}x_{7,k} - x_{4,k}x_{8,k} = 0,$$
$$x_{1,k}x_{3,-k} - x_{1,-k}x_{3,k} + x_{2,k}x_{4,-k} - x_{2,-k}x_{4,k} = 0,$$
$$x_{1,k}x_{7,-k} + x_{2,k}x_{8,-k} - x_{3,k}x_{5,-k} - x_{4,k}x_{6,-k} = 0.$$

The full expressions of the coefficients are given below

$$x_{1,k}(\varphi, J_\perp, nU) = A_1 \frac{1}{nU}\left(v_k^2 - u_k^2\right)(2E_+ + nU + 2E_1) \tag{3.46}$$
$$+ \frac{4A_1 u_k^2 v_k^2}{nU(v_k^2 - u_k^2)} \frac{(2E_- + nU + 2E_1)(E_+^2 - E_-^2 + nU(E_+ - E_-) + B)}{B - (E_+ - E_-)^2 + 2E_1(E_+ - E_-)},$$
$$x_{2,k}(\varphi, J_\perp, nU) = A_1 \frac{2(E_+ - E_-)nUu_k^2 v_k^2}{B - (E_+ - E_-)^2 + 2E_1(E_+ - E_-)},$$
$$x_{3,k}(\varphi, J_\perp, nU) = \frac{2A_1 u_k^2 v_k^2}{(v_k^2 - u_k^2)} \frac{E_+^2 - E_-^2 + nU(E_+ - E_-) + B}{B - (E_+ - E_-)^2 + 2E_1(E_+ - E_-)},$$
$$x_{3,k}(\varphi, J_\perp, nU) = -A_1,$$

$$x_{5,k}(\varphi, J_\perp, nU) = A_2 \frac{1}{nU}\left(v_k^2 - u_k^2\right)(2E_+ + nU + 2E_2) \tag{3.47}$$

$$+ \frac{4A_1 u_k^2 v_k^2}{nU(v_k^2 - u_k^2)} \frac{(2E_- + nU + 2E_2)(E_-^2 - E_+^2 - nU(E_+ - E_-) + B)}{B - (E_+ - E_-)^2 - 2E_2(E_+ - E_-)},$$

$$x_{6,k}(\varphi, J_\perp, nU) = A_2 \frac{2(E_- - E_+)nU u_k^2 v_k^2}{B + (E_+ - E_-)^2 - 2E_2(E_+ - E_-)},$$

$$x_{7,k}(\varphi, J_\perp, nU) = \frac{2A_2 u_k^2 v_k^2}{(v_k^2 - u_k^2)} \frac{E_+^2 - E_-^2 + nU(E_+ - E_-) - B}{B + (E_+ - E_-)^2 - 2E_1(E_+ - E_-)},$$

$$x_{8,k}(\varphi, J_\perp, nU) = -A_2.$$

With $E_\pm$ given by Eq. (3.31), u_k^2 and v_k^2 given by Eq. (3.23), and $E_{1,2}$ given by Eq. (3.42). The normalization constants A_1 and A_2 are obtained from Eqs. (3.45) and the term B reads

$$B = \sqrt{(E_- - E_+)^2\left((E_- + E_+)(E_- + E_+ + 2nU) + n^2 U^2\left(1 - (v_k^2 - u_k^2)^2\right)\right)}. \tag{3.48}$$

(a) $\varphi = \pi/2$, $J_\perp/J_\parallel = 3$, $U/J_\parallel = 1$ (b) $\varphi = \pi/4$, $J_\perp/J_\parallel = 1$, $U/J_\parallel = 0.5$
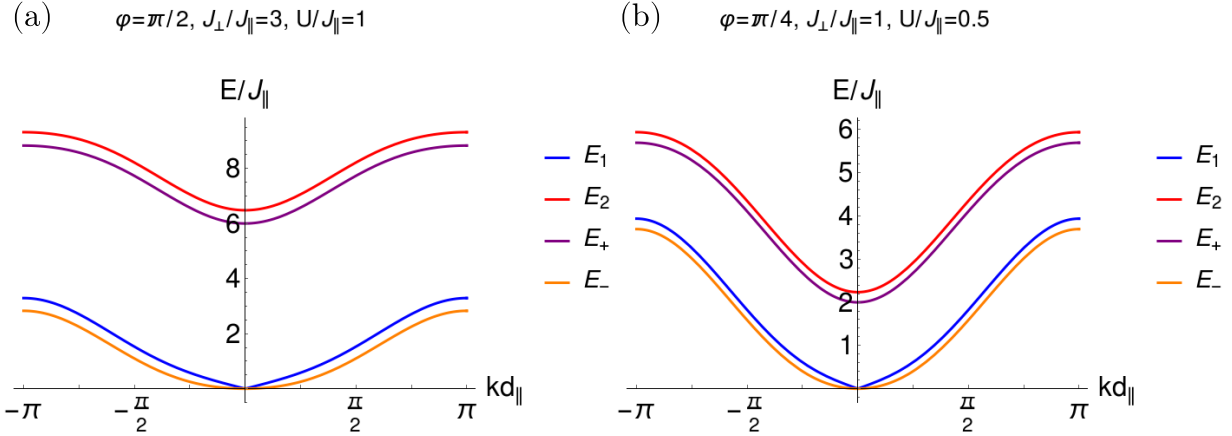
Figure 3.2.: The energy bands $E_1(k)$ (blue line) and $E_2(k)$ (red line), compared with the non-interacting energy bands $E_-(k)$ (orange line) and $E_+(k)$ (purple line), for the parameters (a) $\varphi = \pi/2$, $J_\perp = 3J_\parallel$, $U = 1J_\parallel$ and (b) $\varphi = \pi/4$, $J_\perp = 1J_\parallel$, $U = 0.5J_\parallel$. It can be observed that the interaction shifts the upper band to higher energies and in the lower band beside the shift for small quasi-momentum the quadratic dispersion becomes linear.

In Fig. 3.2(a)-(b) the spectrum of the quasi-particles has been plotted together with the energies of the non-interacting system for two parameter sets. We can observe that the interaction

(a) $\varphi=\pi/4$, $J_\perp/J_\parallel=2$, $U/J_\parallel=0.1$

(d) $\varphi=\pi/2$, $J_\perp/J_\parallel=5$, $U/J_\parallel=0.5$

(b) $\varphi=\pi/4$, $J_\perp/J_\parallel=2$, $U/J_\parallel=0.3$

(e) $\varphi=\pi/2$, $J_\perp/J_\parallel=5$, $U/J_\parallel=1$

(c) $\varphi=\pi/4$, $J_\perp/J_\parallel=2$, $U/J_\parallel=0.5$

(f) $\varphi=\pi/2$, $J_\perp/J_\parallel=5$, $U/J_\parallel=1.5$
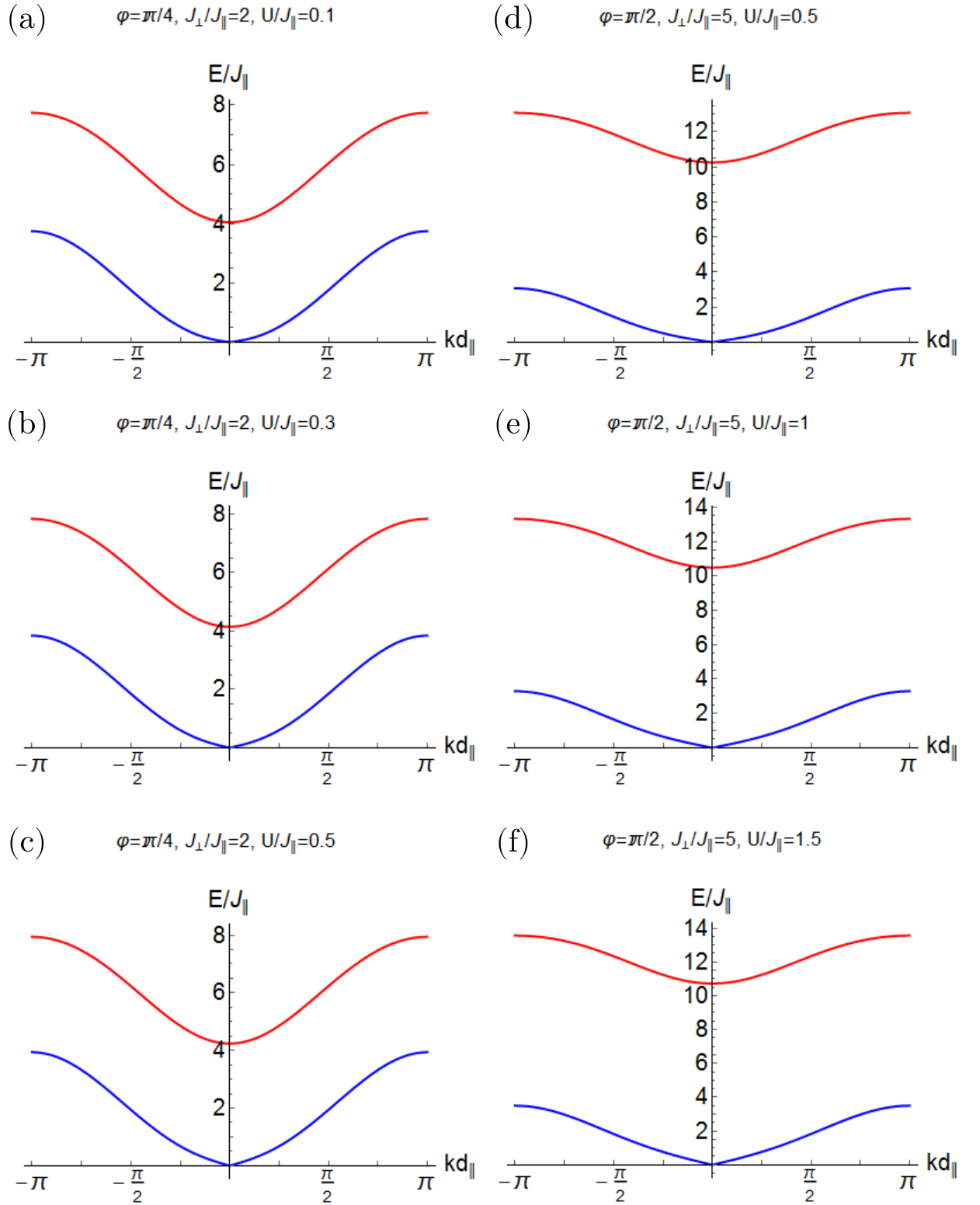
Figure 3.3.: The energy bands $E_1(k)$ (blue line) and $E_2(k)$ (red line), for the parameters (a)-(c) $\varphi = \pi/4$, $J_\perp = 2J_\parallel$, $U \in \{0.1, 0.2, 0.3\}J_\parallel$ and (d)-(f) $\varphi = \pi/2$, $J_\perp = 5J_\parallel$, $U \in \{0.5, 1, 1.5\}J_\parallel$. It can be observed that the extent of the linear dispersion is larger as the interaction strength increases.

changes the physics in the lower band close to minimum $k = 0$, thus a quadratic dispersion $E_-(k) \sim k^2$, particle-like, in the non-interaction system becomes a linear dispersion $E_1(k) \sim k$, phonon-like, in the interacting system. The emergence of the linear dependence close to $k \approx 0$ can be observed in Fig. 3.3(a)-(f) where the eigenenergies have been represented for different values of the interaction, signal of the superfluid nature of this phase.

We will expand the energy of the lower band as a function of the quasi-momentum, in order to compute the sound velocity of the excitations. For small momenta the lower band energy, Eq. (3.42), is approximated by a phonon-like linear dispersion

$$E_1(k) \approx c|k|, \tag{3.49}$$

$$c = \sqrt{nU\cos(\varphi/2) + 4\left(1 - 2\frac{nU + J_\perp/J_\parallel}{nU + 2J_\perp/J_\parallel}\right)\sin(\varphi/2)^2}.$$

which signals the superfluid regime. Here c is the sound velocity of the long wavelength (small momenta) excitations of the interacting Bose gas. Thus we can observe that for finite interactions we have a non-zero sound velocity and, via the Landau criterion, for fluid velocities smaller than the sound velocity, $v < c$, a flow without dissipation. In the case without magnetic flux, the sound velocity reduces to the usual expression in a weakly-interacting superfluid, $c(\varphi = 0) = \sqrt{nU}$ [105]. However, for a non-zero magnetic flux φ, the sound velocity increases monotonically with both the interaction strength U and the rung tunneling amplitude $J_\perp$.

3.2.2.2. Two minima case

In this subsection we will consider the case when the non-interacting lower energy band has two minimum at positions $k = k_\pm$, given by Eq. (3.8). In this case $J_\perp/J_\parallel < 2|\sin(\varphi/2)\tan(\varphi/2)|$.

In the following we will restrict ourselves to the one-band version of the Hamiltonian (3.24)

$$H = \sum_k E_-(k)\gamma^\dagger_{-,k}\gamma_{-,k} \tag{3.50}$$

$$+ \frac{U}{2L}\sum_{k_1,k_2,q}\left(\gamma^\dagger_{-,k_1+q}\gamma^\dagger_{-,k_2-q}\gamma_{-,k_1}\gamma_{-,k_2}\right)\left(u_{k_1+q}u_{k_2-q}u_{k_1}u_{k_2} - v_{k_1+q}v_{k_2-q}v_{k_1}v_{k_2}\right).$$

In this case for the ground state we consider the following N-body variational wavefunction as an ansatz, used in Refs. [83, 84]

$$|GS\rangle = \frac{1}{\sqrt{N!}}\left(\cos(\theta)\gamma^\dagger_{-,k_+} + \sin(\theta)\gamma^\dagger_{-,k_-}\right)|0\rangle, \tag{3.51}$$

where $0 \leq \theta \leq \pi/2$ is the variational parameter and $|0\rangle$ is the vacuum state. This wavefunction captures the condensation of the bosons in the two minima, $k_\pm$, while keeping the proportion of the total population in each minima as a free parameter. For $U = 0$ the ground state is degenerate for any value of θ, but any finite interaction can split this degeneracy [83].

The expectation value of the Hamiltonian (3.50) for the wavefunction (3.51) reads [83, 84]

$$\frac{E_0}{N} = E_-(k_\pm) + \frac{Un}{4}\left[\left(\frac{3}{2}\xi(k_\pm) - 1\right)\sin(2\theta)^2 - \xi(k_\pm) + 2\right] \tag{3.52}$$

where $\xi(k_\pm) = J_\perp^2/\left(J_\perp^2 + 4J_\parallel^2 \sin(k_\pm)^2 \sin(\varphi/2)^2\right)$ is a function which depends only on the physical parameters of the non-interacting system. The minimization of the ground state energy is reduced to finding the optimal value of the parameter θ.

Before performing the minimization, we can also look at the expectation values of the populations in each of the minima as a function of θ

$$\langle n_1 \rangle = \left\langle \gamma^\dagger_{-,k_-}\gamma_{-,k_-}\right\rangle = n\cos(\theta)^2, \tag{3.53}$$

$$\langle n_2 \rangle = \left\langle \gamma^\dagger_{-,k_+}\gamma_{-,k_+}\right\rangle = n\sin(\theta)^2.$$

If $\frac{3}{2}\xi(k_\pm) < 1$, the ground state energy is minimized by $\theta = \pi/4$ [83, 84]. Thus the population, at mean-field level, in each of the minima is the same $\langle n_1 \rangle = \langle n_2 \rangle = n/2$, and we expect two independent condensates in the ground state. In the other case, for $\frac{3}{2}\xi(k_\pm) > 1$, the ground state energy is minimized by $\theta = 0$ or $\theta = \pi/2$ [83, 84], and the population of the two minima are either $(n_1 = n, n_2 = 0)$, or $(n_1 = 0, n_2 = n)$. Thus there exists a condensate either at $k = k_-$, or at $k = k_+$. The mean-field theory shows that the $\mathbb{Z}_2$ symmetry, which represents the symmetry between the two legs of the ladder, is spontaneously broken in this regime. This leads to a density imbalance between the two legs of the ladder and the phase which is called the biased ladder phase (BLP) [83, 84].

The transition between these two phases will occur at $\frac{3}{2}\xi(k_\pm) = 1$, and this condition can be rewritten as [83, 84]

3.2 Weakly interacting bosons

$$J_{\perp,c} = 2\sqrt{\frac{\sin(\varphi/2)^4}{3/2 - \sin(\varphi/2)^2}}\, J_{\|}. \tag{3.54}$$

We note that the critical value of $J_{\perp,c}$ does not depend on the interaction strength U, thus in the following, in order to obtain higher-order dependence, we will try to capture also the impact of the excitations that occur on top of the condensates.

Following the same procedure as in Sec. 3.2.2.1, we derive a quadratic Hamiltonian from Eq. (3.50) by replacing the condensate operators, $\gamma_{-,k_\pm}$ and $\gamma^\dagger_{-,k_\pm}$, with complex numbers and neglecting higher order terms. The Hamiltonian for the case with two different condensates, neglecting the constant term, reads

$$
\begin{aligned}
H_{II} = &\sum_{p>0}[E_-(k_+ + p) + 2n_1 U(v_{k_+}^2 v_{k_++p}^2 + u_{k_+}^2 u_{k_++p}^2) \tag{3.55}\\
&+ 2n_2 U(u_{k_+}^2 v_{k_++p}^2 + v_{k_+}^2 u_{k_++p}^2) - n_1 U(v_{k_+}^4 + u_{k_+}^4) - 4n_2 U v_{k_+}^2 u_{k_+}^2]\gamma^\dagger_{R,p}\gamma_{R,p}\\
+ &\sum_{p>0}[E_-(k_+ - p) + 2n_1 U(v_{k_+}^2 v_{k_+-p}^2 + u_{k_+}^2 u_{k_+-p}^2)\\
&+ 2n_2 U(u_{k_+}^2 v_{k_+-p}^2 + v_{k_+}^2 u_{k_+-p}^2) - n_1 U(v_{k_+}^4 + u_{k_+}^4) - 4n_2 U v_{k_+}^2 u_{k_+}^2]\gamma^\dagger_{R,-p}\gamma_{R,-p}\\
+ &\sum_{p>0}[E_-(k_+ - p) + 2n_2 U(v_{k_+}^2 v_{k_+-p}^2 + u_{k_+}^2 u_{k_+-p}^2)\\
&+ 2n_1 U(u_{k_+}^2 v_{k_+-p}^2 + v_{k_+}^2 u_{k_+-p}^2) - n_2 U(v_{k_+}^4 + u_{k_+}^4) - 4n_1 U v_{k_+}^2 u_{k_+}^2]\gamma^\dagger_{L,p}\gamma_{L,p}\\
+ &\sum_{p>0}[E_-(k_+ + p) + 2n_2 U(v_{k_+}^2 v_{k_++p}^2 + u_{k_+}^2 u_{k_++p}^2)\\
&+ 2n_1 U(u_{k_+}^2 v_{k_++p}^2 + v_{k_+}^2 u_{k_+-p}^2) - n_2 U(v_{k_+}^4 + u_{k_+}^4) - 4n_1 U v_{k_+}^2 u_{k_+}^2]\gamma^\dagger_{L,-p}\gamma_{L,-p}\\
+ &\sum_{p>0} 2U\sqrt{n_1 n_2} v_{k_+} u_{k_+}(v_{k_++p}u_{k_+-p} + v_{k_+-p}u_{k_++p})(\gamma^\dagger_{R,p}\gamma_{L,p} + \gamma^\dagger_{R,-p}\gamma_{L,-p} + h.c.)\\
+ &\sum_{p>0} 4U\sqrt{n_1 n_2} v_{k_+} u_{k_+} v_{k_++p}u_{k_++p}(\gamma^\dagger_{R,p}\gamma^\dagger_{L,-p} + h.c.)\\
+ &\sum_{p>0} 4U\sqrt{n_1 n_2} v_{k_+} u_{k_+} v_{k_+-p}u_{k_+-p}(\gamma^\dagger_{R,-p}\gamma^\dagger_{L,p} + h.c.)\\
+ &\sum_{p>0} U n_1(v_{k_+}^2 v_{k_++p}v_{k_+-p} + u_{k_+}^2 u_{k_++p}u_{k_+-p})(\gamma^\dagger_{R,p}\gamma^\dagger_{R,-p} + h.c.)\\
+ &\sum_{p>0} U n_2(v_{k_+}^2 v_{k_++p}v_{k_+-p} + u_{k_+}^2 u_{k_++p}u_{k_+-p})(\gamma^\dagger_{L,p}\gamma^\dagger_{L,-p} + h.c.),
\end{aligned}
$$

where we have defined $\gamma_{L,p} \equiv \gamma_{-,k_-+p}$ and $\gamma_{R,p} \equiv \gamma_{-,k_++p}$. We note that in the derivation of the Hamiltonian we neglected the umklapp processes, which become important in the situations where the positions of the minima are commensurate with the magnetic flux [84]. We can particularize this Hamiltonian for the case with the condensate in one of the minima, thus we choose, without loss of generality, $n_1 = n$ and $n_2 = 0$. We obtain

$$H_I = \sum_{p>0}[E_-(k_+ + p) + 2nU(v_{k_+}^2 v_{k_++p}^2 + u_{k_+}^2 u_{k_++p}^2) - nU(v_{k_+}^4 + u_{k_+}^4)]\gamma_{R,p}^\dagger \gamma_{R,p} \qquad (3.56)$$

$$+ \sum_{p>0}[E_-(k_+ - p) + 2nU(v_{k_+}^2 v_{k_+-p}^2 + u_{k_+}^2 u_{k_+-p}^2) - nU(v_{k_+}^4 + u_{k_+}^4)]\gamma_{R,-p}^\dagger \gamma_{R,-p}$$

$$+ \sum_{p>0} Un(v_{k_+}^2 v_{k_++p}v_{k_+-p} + u_{k_+}^2 u_{k_++p}u_{k_+-p})(\gamma_{R,p}^\dagger \gamma_{R,-p}^\dagger + \gamma_{R,p}\gamma_{R,-p})$$
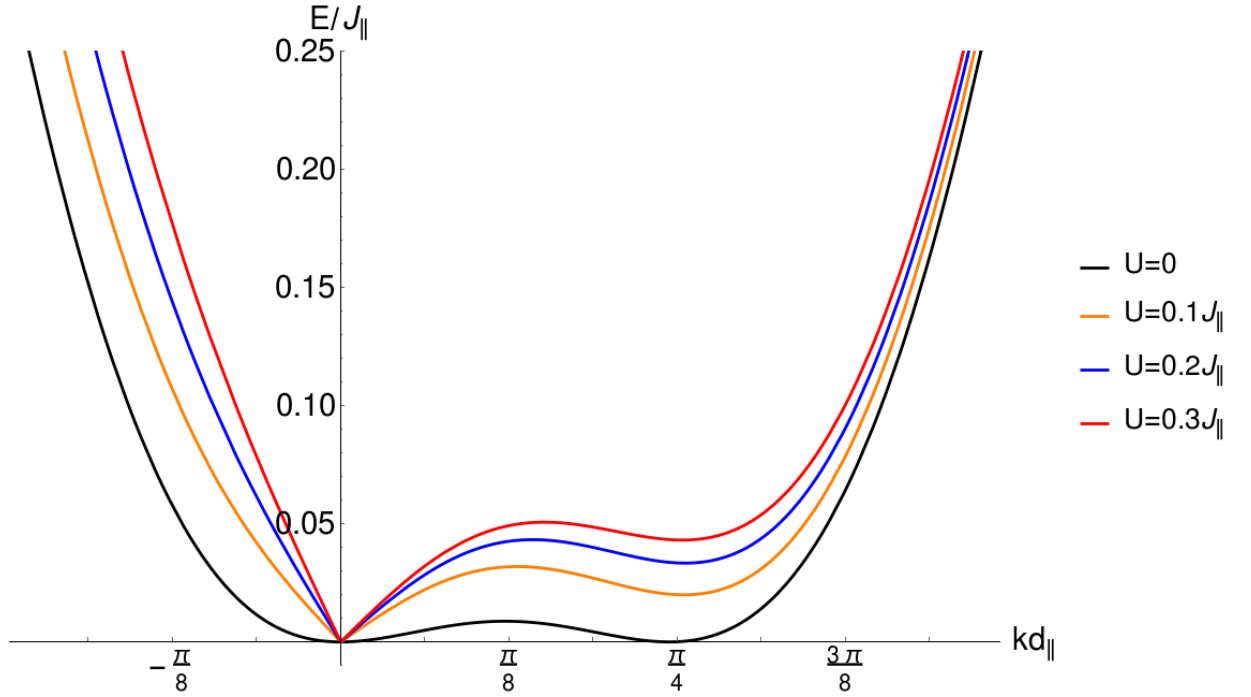
Figure 3.4.: The Bogoliubov excitation spectrum given by the Hamiltonian (3.56) in the biased ladder phase, for a magnetic flux $\varphi = \pi/2$, rung hopping amplitude $J_\perp = 1.2J_\parallel$ and three values of the interaction strength, $U = 0.1J_\parallel$ (orange line), $U = 0.2J_\parallel$ (blue line), $U = 0.1J_\parallel$ (red line), compared with the non-interacting, $U = 0$, dispersion relation (black line). One can observe the roton-like behavior which develops for finite interaction strengths.

3.2 Weakly interacting bosons

We perform the same diagonalization procedure we used in Sec. 3.2.2.1. For the Hamiltonian H_I given by Eq. (3.56), which corresponds to the excitation spectrum in the biased ladder phase, the lower energy band yields

$$E_1(p) = \frac{1}{2}(\zeta(-p) - \zeta(p)) + \sqrt{\frac{1}{4}(\zeta(-p) - \zeta(p))^2 - \eta(p)^2} \qquad (3.57)$$

$$\zeta(p) = E_-(k_- + p) + 2U\left(u_{k_-}^2 u_{k_-+p}^2 + v_{k_-}^2 v_{k_-+p}^2\right)$$

$$\eta(p) = U\left(u_{k_-}^2 u_{k_-+p} u_{k_--p} + v_{k_-}^2 v_{k_-+p} v_{k_--p}\right)$$
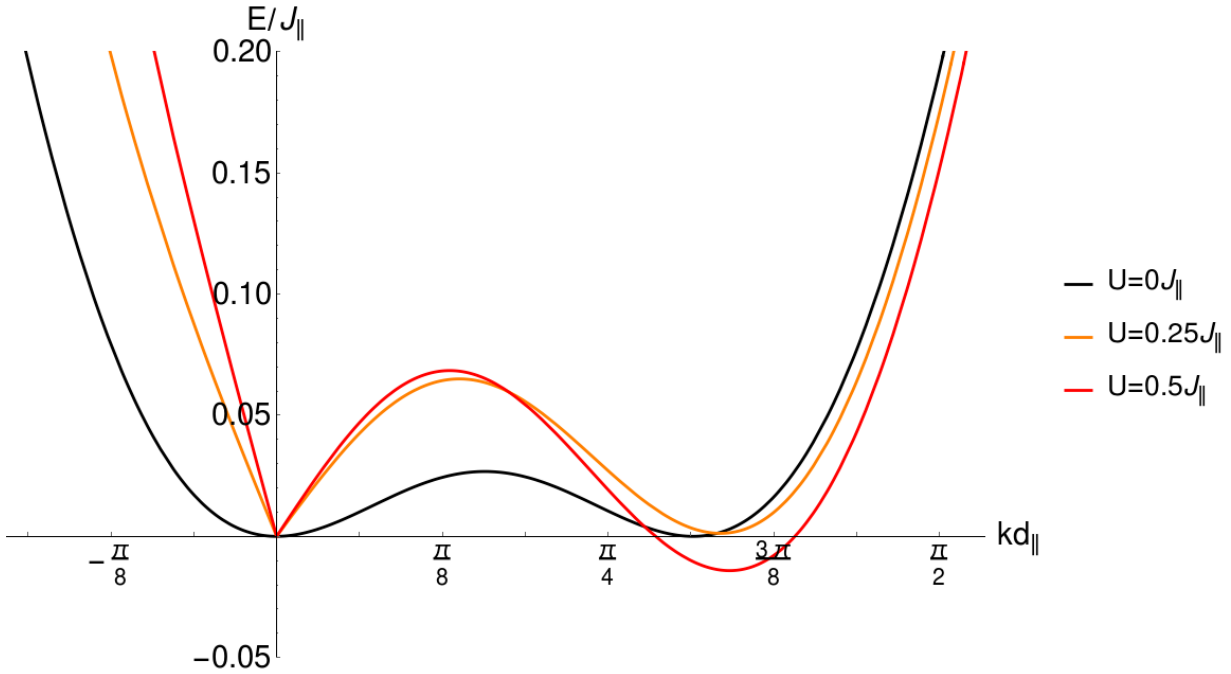
Figure 3.5.: The Bogoliubov excitation spectrum given by the Hamiltonian (3.56), for a magnetic flux $\varphi = \pi/2$, rung hopping amplitude $J_\perp = 1.05J_\parallel$ and two values of the interaction strength, $U = 0.25J_\parallel$ (orange line), $U = 0.5J_\parallel$ (red line), compared with the non-interacting, $U = 0$, dispersion relation (black line).

The Bogoliubov excitation spectrum is depicted in Fig. 3.4, for a magnetic flux $\varphi = \pi/2$, rung hopping amplitude $J_\perp = 1.2J_\parallel$ and three values of the interaction strength. One can observe that for $k \to 0$ the dispersion is linear, as we found in the previous case where the band had only one minimum. The linear dispersion signals the superfluid behavior of this phase. In addition, we also find a local minimum close to the value $k \approx 2k_+$, corresponding to a roton-like behavior. This can be interpreted as a massive excitation which comes from the breaking

of the $\mathbb{Z}_2$ symmetry [84]. In Fig. 3.5 we have represented the Bogoliubov spectrum for a rung hopping amplitude of $J_\perp = 1.05 J_\parallel$, we observe that for a lower value of $J_\perp$ the spectrum is softened. Thus, above a critical interaction strength the energy of the roton-like local minimum reaches negative values, this implies that the biased ladder phase becomes unstable. A more detailed discussion about the stability of the Bogoliubov theory will be given in the next section.
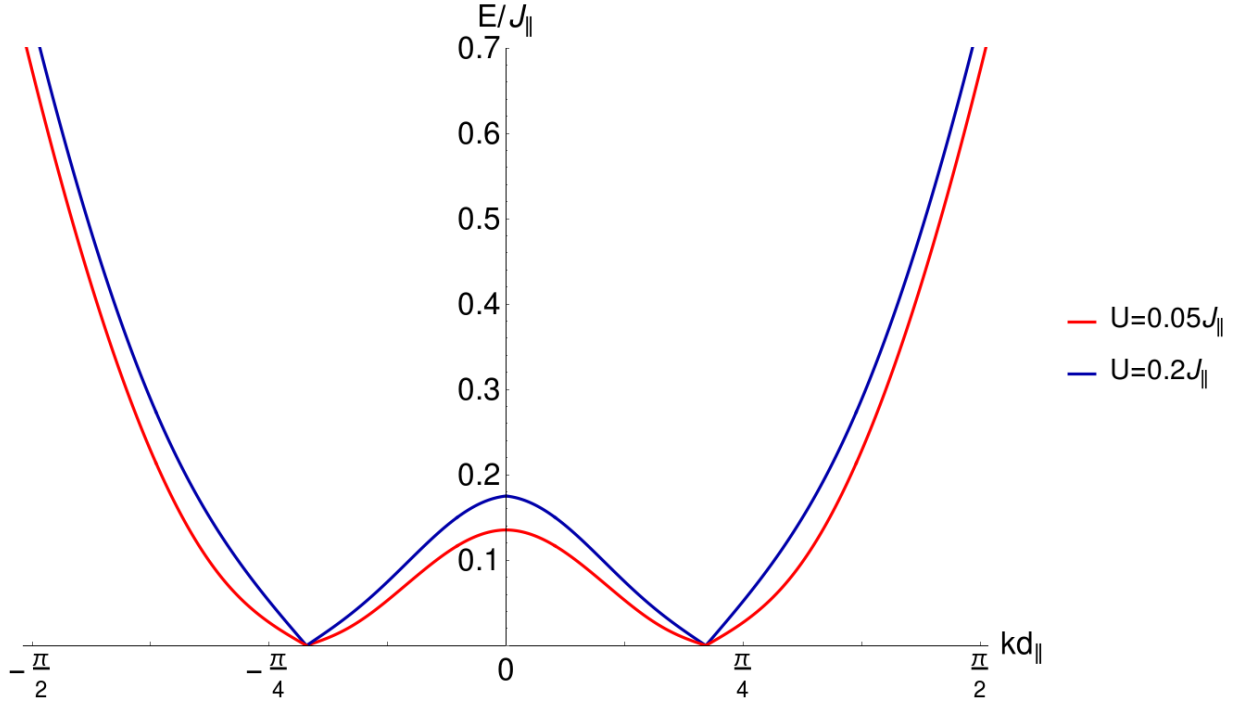
Figure 3.6.: The Bogoliubov excitation spectrum given by the Hamiltonian (3.55) for two independent condensates, for a magnetic flux $\varphi = \pi/2$, rung hopping amplitude $J_\perp = 0.7 J_\parallel$ and two values of the interaction strength, $U = 0.05 J_\parallel$ (red line), $U = 0.2 J_\parallel$ (dark blue line). We observe a linear dispersion close to the two minima.

In the following, we will compute the excitation spectrum for the case of two condensates, given by H_{II} in Eq. 3.55. Due to the intricate form of the Hamiltonian one can not obtain with ease an explicit expression for the dispersion relation, thus we will numerically diagonalize the Hamiltonian. The excitation spectrum is plotted in Fig. 3.6, for $\varphi = \pi/2$, $J_\perp = 0.7 J_\parallel$ and two values of the interaction strength $U = 0.05 J_\parallel$ and $U = 0.2 J_\parallel$. We can observe that around each of the minima we have a linear behavior of the energy as a function of the quasi-momentum, thus this phase is characterized by two independent phononic modes. One can also notice that if we increase the interaction strength the extent of the linear regime becomes larger.

The Hamiltonian H_{II}, Eq. (3.55), fails to describe the system for values of the rung tunneling

amplitude close to the critical value that gives the transition from one condensate to the two condensates, Eq. (3.54), for finite interaction strengths. As we can see in Fig. 3.7 the excitation energy has a finite imaginary part, which signals an instability in the model. In Fig. 3.7 the magnetic flux is $\varphi = \pi/2$ and the rung hopping amplitude is $J_\perp = 0.99 J_\parallel$. For this value of the magnetic flux the critical rung hopping amplitude is $J_{\perp,c} = 1 J_\parallel$. The parameter region and the reasons for which the quadratic Hamiltonians H_I and H_{II} (Eq. (3.55)-(3.56)) do not give physical results will be presented in the next section.
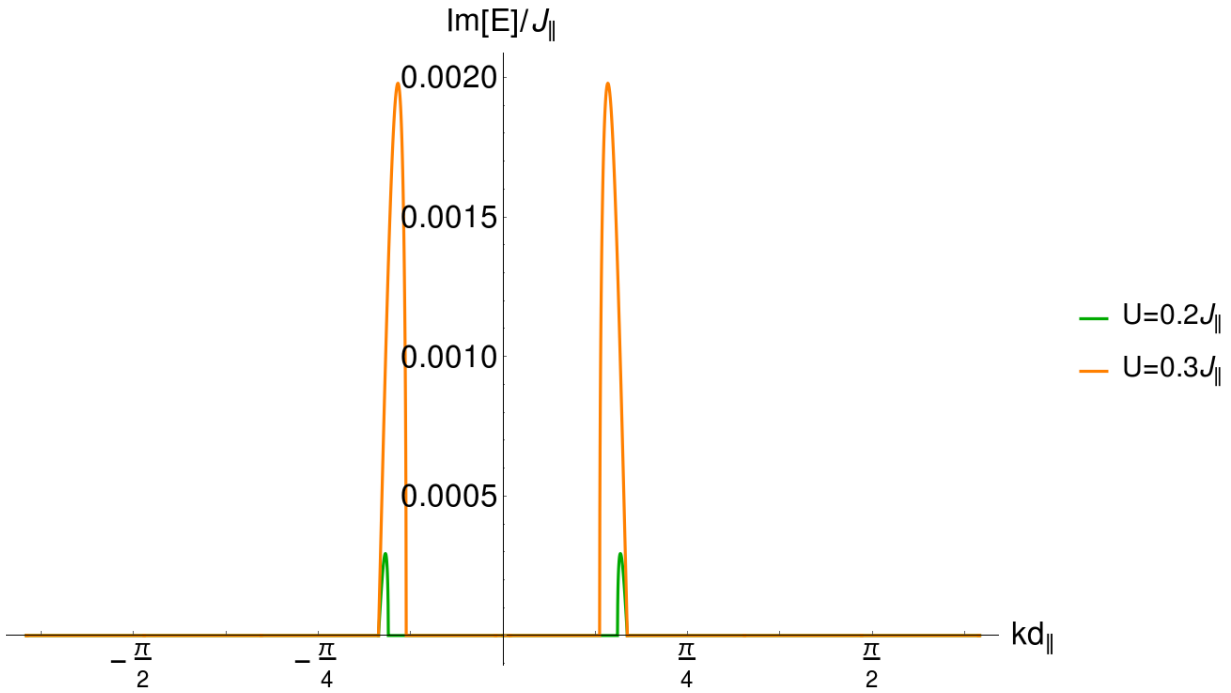
Figure 3.7.: The imaginary part of the Bogoliubov excitation spectrum given by the Hamiltonian (3.55) for two independent condensates, for a magnetic flux $\varphi = \pi/2$, rung hopping amplitude $J_\perp = 0.99 J_\parallel$ and two values of the interaction strength, $U = 0.2 J_\parallel$ (green line), $U = 0.3 J_\parallel$ (orange line). Close to the two minima the energies acquire a finite imaginary part.

3.2.3. Shortcomings of the Bogoliubov theory

We will first discuss the instabilities that appeared during the computation of the Bogoliubov excitation spectrum given by the two quadratic Hamiltonians H_I and H_{II}, (Eq. (3.55)-(3.56)), for the case of two minima. Fig. 3.8 shows different regions in the parameter space $(J_\perp/J_\parallel, U/J_\parallel)$ with stable and unstable results. The yellow region is where the two quadratic Hamiltonians give physical results. The blue region is where one of the two instabilities appear, either negative roton minimum for the one condensate regime, or imaginary energies for the regime with
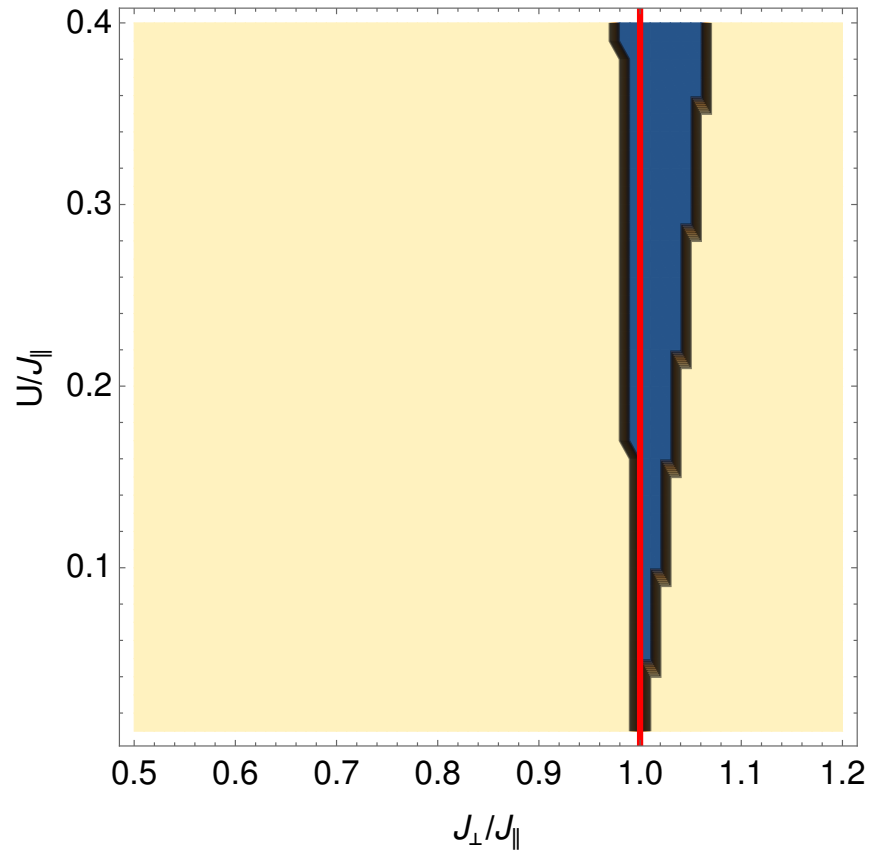
Figure 3.8.: With yellow the region where the two quadratic Hamiltonians, Eq. (3.55)-(3.56), give physical results, with blue the region where one of the two instabilities appear, negative roton minimum for the one condensate regime, or imaginary energies for the regime with two condensates, and the red line corresponds to the critical value given by Eq. (3.54).

two condensates. The red line corresponds to the critical value given by Eq. (3.54). We can observe that for interaction strengths close to zero, $U/J_\parallel \lesssim 0.02$, the transition from the biased ladder phase to the regime with two independent condensates preempts the instability. But for larger interaction strengths, we have a whole domain in the $(J_\perp/J_\parallel, U/J_\parallel)$ plane with unphysical results. A possible explanation for this is that in the derivation of the quadratic Hamiltonian (3.55), via the Bogoliubov prescription, the terms that represented the umklapp processes have been neglected. Thus between the biased ladder superfluid phase and the phase with two independent gapless modes (later we will see that this corresponds to the vortex liquid superfluid), it may exist a phase for which the commensurability of the magnetic flux plays an important role. In Chap. 5 we will find such a phase, namely the vortex lattice superfluid.

The second shortcoming is the presence of logarithmically divergences integrals in the computation of the expectation value of certain observables. We will exemplify this for the expectation value of the directed rung tunneling, $\langle K_\perp \rangle$, which we need for solving the self-consistency and stability conditions, as we showed in Sec. 2.3 and Sec. 2.4. For simplicity, we will consider the case of one minimum in the lower energy band, as considered in Sec. 3.2.2.1.

From expression of the directed rung tunneling given in Eq. (2.20) performing the gauge transformation (3.20) and going to the momentum space, we obtain

$$K_\perp = \sum_k b_{0,k}^\dagger b_{1,k}. \tag{3.58}$$

Furthermore, performing the transformation used for diagonalization of the kinetic part, Eq. (3.22)-(3.23) and taking the expectation value with the respect of the ground state we have

$$\langle K_\perp \rangle = K_0 + \sum_{k \neq 0} \langle u_k v_k (\gamma_{-,k}^\dagger \gamma_{-,k} - \gamma_{+,k}^\dagger \gamma_{+,k}) + v_k^2 \gamma_{+,k}^\dagger \gamma_{-,k} - u_k^2 \gamma_{-,k}^\dagger \gamma_{+,k} \rangle, \tag{3.59}$$

$$K_0 = u_0 v_0 \langle \gamma_{-,0}^\dagger \gamma_{-,0} \rangle = \frac{1}{2} N_0,$$

where $N_0 = N$ is the condensate population. Next step consists in transforming to the basis of the quasi-particles operators, given by Eqs. (3.43)-(3.44). We note that in the ground state no excitations exist, thus the terms which contain the quasi-particle operators do not have any contribution. We obtain

$$\langle K_\perp \rangle = \frac{1}{2}N + \sum_{k \neq 0} \left[u_k v_k \left(x_{3,k}^2 + x_{4,k}^2 - x_{7,k}^2 - x_{8,k}^2 \right) + \left(v_k^2 - u_k^2 \right) \left(x_{3,k} x_{4,k} + x_{7,k} x_{8,k} \right) \right], \quad (3.60)$$

with the coefficients $x_{i,k}$ given by Eqs. (3.46)-(3.47). In order to evaluate the expectation value we will take the continuum limit of $\langle K_\perp \rangle / L$ and convert the sum into an integral

$$\frac{\langle K_\perp \rangle}{L} = \frac{1}{2}n_0 + \int_0^\pi \frac{dk}{\pi} \left[u_k v_k \left(x_{3,k}^2 + x_{4,k}^2 - x_{7,k}^2 - x_{8,k}^2 \right) + \left(v_k^2 - u_k^2 \right) \left(x_{3,k} x_{4,k} + x_{7,k} x_{8,k} \right) \right].$$
$$(3.61)$$

Computing the integrand from Eq. (3.61) we obtain that its leading order behaves like $\sim 1/k$, thus the integral has a logarithmic divergence for small quasi-momenta, $k \to 0$, for finite interaction strengths. We obtain the same behavior for the regime with two minima. This is consistent with the results obtained in the literature for the condensate depletion for the bosonic quasi-one-dimensional ladder in a magnetic flux [110], or a two-dimensional lattice in a magnetic flux [111]. A solution to this problem can consist in the application of a small-momentum cutoff k_0 for the integral over k [111], with $k_0 \approx L^{-1}$, as a real system is finite. In this case $\langle K_\perp \rangle$ would be finite, but it would have a logarithmic dependence on the cutoff k_0. In our system, this approach does not work, because both the self-consistency and the stability conditions are highly sensitive on the value of $\langle K_\perp \rangle$ and the effect of the cutoff is too large. Thus, we cannot use the Bogoliubov theory in order to describe the coupled ladder and cavity system.

3.3. Ground state phases

As we described in Ref. [98], the effective model, Eq. (2.27), has been studied as a stand-alone model describing bosonic two-leg ladders with repulsive contact interaction in the presence of a uniform, static gauge field. DMRG and bosonization studies have explored the phase diagram beyond the weakly interacting regime [76–91], observing Meissner, vortex and vortex lattices phases on top of the superfluid or Mott-insulating states.

The phase transitions that occur in this model take place in two sectors. These sectors correspond, in the limit of weak coupling (i.e. $J_\perp / J_\parallel \ll 1$), to the symmetric $(b_{0,j} + b_{1,j})$ and

(a)   M-SF (c=1), M-MI (c=0): ρ_v =0, J_r =0, Δn=0

(b)   BLP-SF: c=1, ρ_v =0, J_r =0, Δn>0

(c)   V-SF: c=2, ρ_v>0, J_r>0, Δn=0

(d)   VL$_{1/2}$-SF: c=1, ρ_v =1/2, J_r>0, Δn=0

(e)   VL$_{1/3}$-SF: c=1, ρ_v =1/3, J_r>0, Δn=0
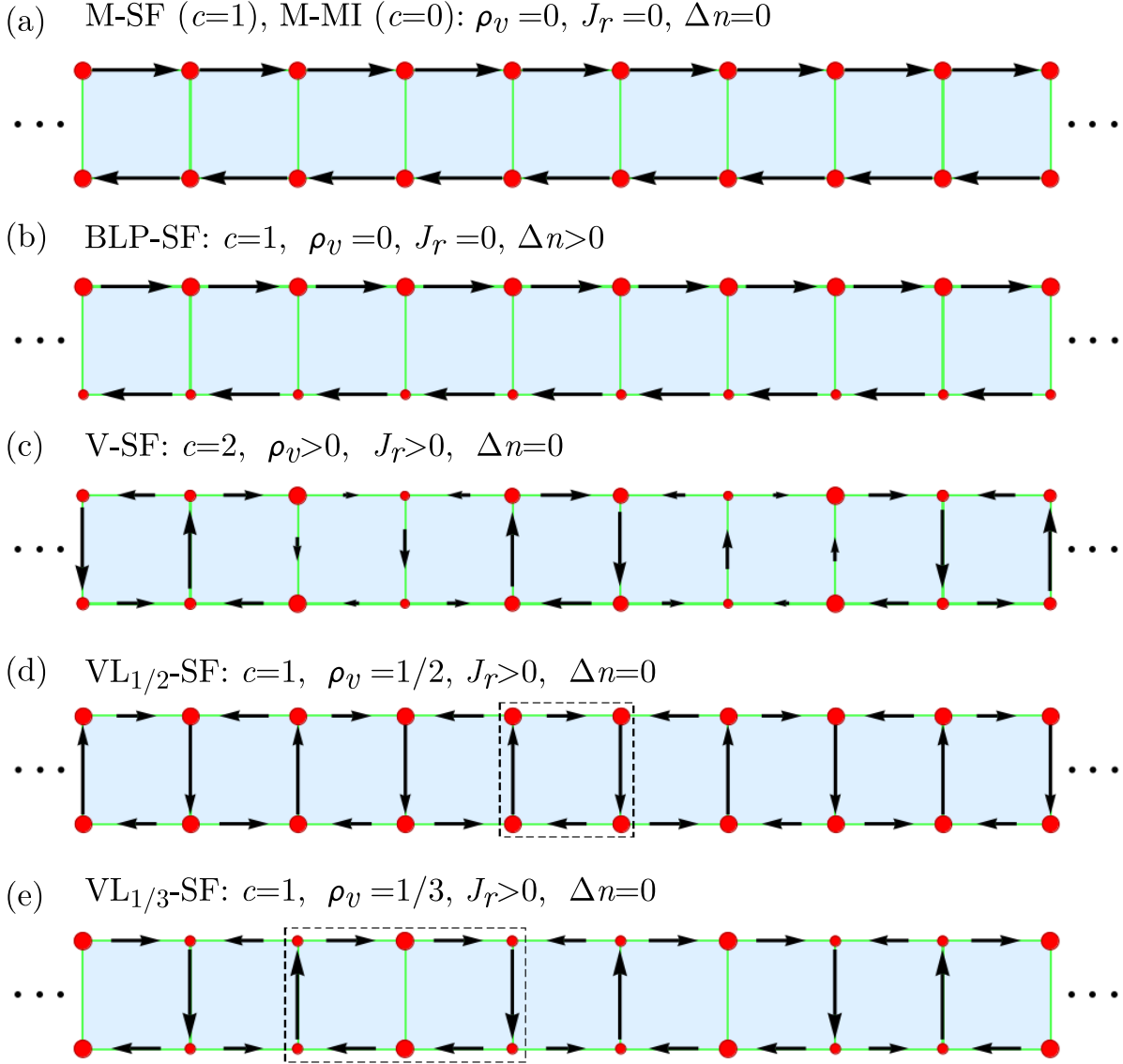
Figure 3.9.: Current patterns and on-site density for some of the different phases of the effective model, (a) the Meissner phase (M-SF, M-MI), (b) the biased-ladder superfluid phase (BLP-SF), (c) vortex liquid (V-SF) phase with a vortex density $1/3 < \rho_v < 2/5$, and (d)-(e) vortex lattices (VL$_{1/2,1/3}$-SF) with (d) $\rho_v = 1/2$, and (e) $\rho_v = 1/3$. The length of the arrows is proportional to the strength of the local currents and the size of the red circles scales with the on-site density (DMRG data). The dashed rectangles represent the unit cell for the vortex lattice phases. The definitions of the observables that describe each phase can be found in the main text. Figure adapted from Ref. [98].

antisymmetric $(b_{0,j} - b_{1,j})$ combination of the operators on the two legs. The Mott insulator to superfluid transition is located in the symmetric sector, while the Meissner to vortex phase transitions occur in the antisymmetric sector.

In the following we will describe the observables that indicate the nature of the phases obtain as ground states of the effective model, Eq. (2.27). One quantity which gives information on the phases is the central charge c, which can be interpreted as the number of gapless modes. The central charge can be extracted from the scaling of the von Neumann entanglement entropy $S_{vN}(l)$ of an embedded subsystem of length l in a chain of length L. The scaling behaviour for the different phases will be exemplified using DMRG data in Chap. 5. For open boundary conditions the entanglement entropy for the ground state of gapless phases scales as [112–114]

$$ S_{vN} = \frac{c}{6} \log \left(\frac{L}{\pi} \sin \frac{\pi l}{L} \right) + s_1, \tag{3.62} $$

where s_1 is a non-universal constant and we have neglected oscillatory terms [115] due to the finite size of the system, and logarithmic corrections [116].

The superfluid and Mott-insulating phases can be distinguished from the decay of the single particle correlation, here we will use $\langle b^\dagger_{m,L/4} b_{m,L/4+d} + h.c.\rangle$, with distance d. The correlations will decay algebraically with distance in a superfluid state and exponentially in a Mott-insulating state [117].

Other important characteristics of the quantum chiral phases (Meissner, vortex liquid, or vortex lattice) can be inferred from the configurations of the local currents, which is experimentally accessible in the bosonic ladder system [74, 118]. We define the local currents on the leg $j^{\parallel}_{m,j}$ and the rung $j^{\perp}_j$, respectively, as

$$ \begin{aligned} j^{\parallel}_{m,j} &= -i J_\parallel (b^\dagger_{m,j} b_{m,j+1} - h.c.), \\ j^{\perp}_j &= -i J_\perp (e^{i\varphi j} b^\dagger_{1,j} b_{0,j} - h.c.). \end{aligned} \tag{3.63} $$

In addition to the local currents, the chiral current J_c and the average rung current J_r are of interest and defined as

3.3 Ground state phases

$$J_c = \frac{1}{2L} \sum_j \langle j^{\parallel}_{0,j} - j^{\parallel}_{1,j} \rangle,$$

$$J_r = \frac{1}{L} \sum_j |\langle j^{\perp}_j \rangle|. \tag{3.64}$$

All non-trivial phases that we are presenting here have a finite chiral current. The Meissner phases are characterized by a vanishing average rung current, $J_r = 0$, and the vortex and vortex lattice phases by finite rung currents, $J_r > 0$. An additional quantity, the vortex density is defined as the inverse of the vortex length, $\rho_v = l_v^{-1}$. Where l_v is the typical size of the vortices and we extract it from the position of the peak of the Fourier transform of the local rung current configurations $\langle j_r^{\perp} \rangle$. From the value of ρ_v one identifies the periodicity of the vortex lattice phases.

For the rest of this section we will describe the phases that appear as steady states for the sets of parameters that will be considered in Chap. 5. In Fig. 3.9 we briefly explain the different phases. Fig. 3.9(a) shows a Meissner phase, which can be a Meissner superfluid (M-SF) or a Meissner Mott insulator (M-MI). Both of these phases have vanishing currents on the rungs in the bulk of the system and a finite chiral current. The distinction between the two phases can be made by calculating the central charge. The Meissner superfluid phase is gapless in the symmetric sector with $c = 1$, while the Meissner Mott insulator is totally gapped, with $c = 0$.

The biased-ladder phase (BLP) [79, 80, 83–85], (see Fig. 3.9(b)), breaks the discrete $\mathbb{Z}_2$ symmetry associated with the inversion of the two legs of the ladder and the sign of the flux. The characteristic signature of this phase is that the density is higher on one of the legs. The observable that we will use to identify this phase is the density imbalance, Δn. The imbalance is defined as

$$\Delta n = \frac{1}{2L} \left| \sum_j \langle n_{0,j} - n_{1,j} \rangle \right|. \tag{3.65}$$

The biased ladder phase has a gapless mode in the symmetric sector with $c = 1$, and a vanishing rung current.

The vortex superfluid phase (V-SF), with the local current and density pattern depicted in Fig. 3.9(c), has two gapless modes (symmetric and antisymmetric), thus it has a central charge

$c = 2$. It is also characterized by a finite vortex density, ρ_v, which is incommensurate with the ladder.

The existence of vortex lattice phases has been demonstrated in bosonic ladders by Refs. [79–82], for different vortex densities. In Fig. 3.9(d)-(e) we have represented the current and density pattern for the vortex lattice superfluid phases (VL$_{\rho_v}$-SF) with $\rho_v = 1/2$ and $1/3$. In these phases the vortices are commensurate with the ladder. Both of these two vortex lattices have a central charge $c = 1$, since the symmetric mode is gapless and the antisymmetric mode is gapped. Due to the spontaneous symmetry breaking of the translational symmetry in the vortex lattices, the unit cell becomes q-fold enlarged, with $q = 2$ and 3 in these cases. This can lead to a change in the sign of the chiral current, as described in Ref. [79].

The mentioned states do not represent an exhaustive list of the possible phases of the ground-state of the bosonic ladder under an artificial magnetic flux. We focused on the ones we can stabilize dynamically in the cavity, for the parameters considered in Chap. 5. Beside the mentioned phases there exists numerical evidence for vortex and vortex lattice Mott insulators [78, 79], vortex lattice superfluid with $\rho_v = 1/4$ and charge density waves [80], also Laughlin states have been proposed [86–88].

4. Numerical methods

We probe our model (Eq. 2.27) numerically with a density matrix renormalization group (DMRG) algorithm in the matrix product state form [119–122], using the ITensor Library [123]. In Sec. 4.1 we present briefly the basic concepts of the DMRG algorithm in the MPS form, afterwards in Sec. 4.2 we describe our implementation of the algorithm. At the end of this chapter in Sec. 4.3 and Sec. 4.4 we analyze the convergence of the method.

4.1. Introduction to the DMRG method in the matrix product states representation

The density matrix renormalization group (DMRG) is currently one of the most powerful methods in the study of one dimensional strongly correlated lattice systems. The method was introduced by S. R. White in 1992 [119]. The biggest challenge that arises in the simulation of quantum many-body systems is that the dimension of the Hilbert space of a system of size L grows exponentially with its size. DMRG is an iterative variational method, which has the goal to find the best approximate for a desired state of the system, by reducing and retaining only the most important degrees of freedom at each iteration. In the following we make use of the matrix product states formulation of the DMRG method [121].

One of the tools of linear algebra that is used extensively in the DMRG algorithm is the singular value decomposition (SVD). The theorem states that any arbitrary rectangular matrix M of dimensions $(m \times n)$ can be decomposed as

$$M = USV^\dagger, \tag{4.1}$$

where U is a unitary matrix, $UU^\dagger = \mathbb{1}$, of dimensions $(m \times \min(m, n))$; S is a diagonal matrix of dimensions $(\min(m, n) \times \min(m, n))$, with non-negative entries $\sqrt{\lambda_i} \geq 0$, called singular values; $V^\dagger$ is also a unitary matrix of dimensions $(\min(m, n)) \times n)$. The (Schmidt) rank r of matrix M is given by the number of non-zero singular values, $\sqrt{\lambda_i} > 0$.

As an application of the SVD, one can derive the Schimdt decomposition of an arbitrary quantum state $|\Psi\rangle$. Let us consider a one-dimensional system, which can be divided into two subsystems A and B. The wavefunction $|\Psi\rangle$ describes the full system AB and it can be written as

$$|\Psi\rangle = \sum_{i,j} \Psi_{i,j} |i\rangle_A |j\rangle_B , \tag{4.2}$$

where $\{|i\rangle_A\}$ and $\{|j\rangle_B\}$ are the orthonormal basis of the subsystem A, of dimension m, and B, of dimension n, respectively. By the matrix Ψ we will understand a matrix with the entries $\Psi_{i,j}$. We can now perform the singular value decomposition of the matrix Ψ, which gives

$$\begin{aligned}
|\Psi\rangle &= \sum_{i,j} \sum_{a=1}^{\min(m,n)} U_{i,a} S_{a,a} V_{a,j}^* |i\rangle_A |j\rangle_B \\
&= \sum_{a=1}^{\min(m,n)} S_{a,a} \left(\sum_i U_{i,a} |i\rangle_A \right) \left(\sum_j V_{a,j} |j\rangle_B \right) \\
&= \sum_{a=1}^{r} \sqrt{\lambda_a} |a\rangle_A |a\rangle_B ,
\end{aligned} \tag{4.3}$$

where the sum runs only over the non-zero singular values $\sqrt{\lambda_a} > 0$, as we mentioned the upper bound is given by the rank $r \leq \min(m,n)$ of S. Due to the unitarity of the matrices U and V, the sets $\{|a\rangle_A\}$ and $\{|a\rangle_B\}$ are the orthonormal basis on A and B respectively. The Schmidt decomposition is important in our context, as it can be used to quantify the entanglement between the two subsystems A and B. Thus for the value of the Schmidt rank $r = 1$, $|\Psi\rangle$ can be written as a product state, and the entanglement between A and B increases for larger values of the rank r.

Now we want to construct a state $\left|\tilde{\Psi}\right\rangle$ of a maximal rank $D < r$, $\left|\tilde{\Psi}\right\rangle = \sum_{a=1}^{D} \sqrt{\lambda_a} |a\rangle_A |a\rangle_B$, which approximates the state $|\Psi\rangle$ the best. We perform this by minimizing the norm,

$$\left\| |\Psi\rangle - \left|\tilde{\Psi}\right\rangle \right\|^2 = 1 - \sum_{a=D}^{r} \lambda_a. \tag{4.4}$$

The singular values are ordered $\lambda_1 \geq \lambda_2 \geq ...$, such that we retain the biggest D singular values. The approximation becomes better if λ_a decay quickly for increasing a, we note that the approximation becomes exact if $D \geq r$.

Now we have all the necessary tools in order to exemplify the construction and compression of the matrix product states. We can write any quantum state for a lattice system with L sites

4.1 Introduction to the DMRG method in the matrix product states representation

and the dimension of the local Hilbert space d for each site as

$$|\Psi\rangle = \sum_{\sigma_1,...,\sigma_L} c_{\sigma_1,...,\sigma_L} |\sigma_1, ..., \sigma_L\rangle, \qquad (4.5)$$

where $\{|\sigma_j\rangle\}$ is the local basis and $|\vec{\sigma}\rangle \equiv |\sigma_1, ..., \sigma_L\rangle \equiv \{|\sigma_1\rangle\} \otimes ... \otimes \{|\sigma_L\rangle\}$. We have exponentially many coefficients $c_{\sigma_1,...,\sigma_L}$, which contain the information of the state.

The matrix product state is a more convenient notation of $|\Psi\rangle$, which gives a more local notion of the state [121]. From now on we assume that $|\Psi\rangle$ is normalized, and its matrix product state notation reads

$$|\Psi\rangle = \sum_{\sigma_1,...,\sigma_L} M^{\sigma_1} M^{\sigma_2}...M^{\sigma_L} |\sigma_1, ..., \sigma_L\rangle, \qquad (4.6)$$

where M^{σ_j}, $j = 1...L$, are a collection of matrices. But the matrix product will result in a scalar, namely $c_{\sigma_1,...,\sigma_L}$, as M^{σ_1} is a row vector and M^{σ_L} is a column vector. The matrix product state representation can be constructed by applying the singular value decomposition repeatedly, starting from the left or from the right of the matrix product. This results in a so-called left-canonical or right-canonical matrix product state. In the following we will exemplify this by constructing the left-canonical matrix product state. We begin by reshaping the d^L coefficients $c_{\sigma_1,...,\sigma_L}$ into a matrix $\Psi_{\sigma_1,(\sigma_2...\sigma_L)}$ of dimensions $\left(d \times d^{L-1}\right)$ and performing the singular value decomposition of this matrix

$$\Psi_{\sigma_1,(\sigma_2...\sigma_L)} = \sum_{a_1} U_{\sigma_1,a_1} S_{a_1,a_1} V^{\dagger}_{a_1,(\sigma_2...\sigma_L)} \equiv \sum_{a_1} U_{\sigma_1,a_1} c_{a_1,\sigma_2,...,\sigma_L}, \qquad (4.7)$$

where in the last equality we performed the matrix multiplication and reshaped the result back into a vector $c_{a_1,\sigma_2,...,\sigma_L}$. From this vector we construct a new matrix $\Psi_{(a_1,\sigma_2),(\sigma_3...\sigma_L)} \equiv c_{a_1,\sigma_2,...,\sigma_L}$. We also reshape the matrix U into a row vector A^{σ_1}, with $A^{\sigma_1}_{a_1} = U_{\sigma_1,a_1}$. After these operations we have

$$c_{\sigma_1,...,\sigma_L} = \sum_{a_1} A^{\sigma_1}_{a_1} \Psi_{(a_1\sigma_2),(\sigma_3...\sigma_L)}. \qquad (4.8)$$

If we successively apply these operations, the singular value decomposition and reshaping, we obtain

$$c_{\sigma_1,...,\sigma_L} = ... \tag{4.9}$$

$$= \sum_{a_1}\sum_{a_2} A_{a_1}^{\sigma_1} U_{(a_1\sigma_2),a_2} S_{a_2,a_2} V_{a_2,(\sigma_3...\sigma_L)}^{\dagger}$$

$$= \sum_{a_1}\sum_{a_2} A_{a_1}^{\sigma_1} A_{a_1,a_2}^{\sigma_2} \Psi_{(a_2\sigma_3),(\sigma_4...\sigma_L)} = ...$$

$$= \sum_{a_1..a_{L-1}} A_{a_1}^{\sigma_1} A_{a_1,a_2}^{\sigma_2}...A_{a_{L-2},a_{L-1}}^{\sigma_{L-1}} A_{a_{L-1}}^{\sigma_L}$$

$$= A^{\sigma_1} A^{\sigma_2}...A^{\sigma_L},$$

where A^{σ_j} is a matrix with the elements $A_{a_{j-1},a_j}^{\sigma_j} = U_{(a_{j-1}\sigma_j),a_j}$ and of dimensions $(r_{j-1} \times r_j)$. The maximum dimensions that the collection of A-matrices can have are $(1 \times d), (d \times d^2), ..., (d^{L/2-1} \times d^{L/2}), (d^{L/2} \times d^{L/2-1}), ..., (d \times 1)$. The maximum dimensions are reached if all singular values are non-zero, in each of the singular value decompositions. Inserting this result in Eq. (4.6), the new representation of the state reads

$$|\Psi\rangle = \sum_{\sigma_1,...,\sigma_L} A^{\sigma_1} A^{\sigma_2}...A^{\sigma_L} |\sigma_1, ..., \sigma_L\rangle, \tag{4.10}$$

with

$$\sum_{\sigma_j} A^{\sigma_j\dagger} A^{\sigma_j} = \mathbb{1}, \tag{4.11}$$

these relations define the left-canonical matrix product state. Analogously, one can define a right-canonical matrix product state, by starting the reshaping procedure from the right

$$c_{\sigma_1,...,\sigma_L} = \Psi_{(\sigma_1...\sigma_{L-1}),\sigma_L,} = ... \tag{4.12}$$

$$= \sum_{a_{L-1}} U_{(\sigma_1...\sigma_{L-1}),a_{L-1}} S_{a_{L-1},a_{L-1}} V_{a_{L-1}\sigma_L}^{\dagger}$$

$$= \sum_{a_{L-1}} \Psi_{(\sigma_1...\sigma_{L-2}),(\sigma_{L-1}a_{L-1})} B_{a_{L-1}}^{\sigma_L} = ...$$

$$= \sum_{a_1..a_{L-1}} B_{a_1}^{\sigma_1} B_{a_1,a_2}^{\sigma_2}...B_{a_{L-2},a_{L-1}}^{\sigma_{L-1}} B_{a_{L-1}}^{\sigma_L}$$

$$= B^{\sigma_1} B^{\sigma_2}...B^{\sigma_L},$$

where B^{σ_j} is a matrix with the elements $B^{\sigma_j}_{a_{j-1},a_j} = V^\dagger_{a_{j-1},(\sigma_j a_j)}$. In this case the state becomes

$$|\Psi\rangle = \sum_{\sigma_1,...,\sigma_L} B^{\sigma_1} B^{\sigma_2}...B^{\sigma_L} |\sigma_1, ..., \sigma_L\rangle, \qquad (4.13)$$

with

$$\sum_{\sigma_j} B^{\sigma_j} B^{\sigma_j\dagger} = \mathbb{1}, \qquad (4.14)$$

these relations define the right-canonical matrix product state.

We can also perform a mixed decomposition from both right and left, resulting in a mixed canonical product state

$$|\Psi\rangle = \sum_{\sigma_1,...,\sigma_L} A^{\sigma_1}...A^{\sigma_l} S B^{\sigma_{l+1}}...B^{\sigma_L} |\sigma_1, ..., \sigma_L\rangle, \qquad (4.15)$$

where the A matrices are left-normalized and the B matrices are right-normalized. The S matrix has the components $S_{a_l,a_l} = \sqrt{\lambda_{a_l}}$, which represent the singular values on the link $(l, l+1)$. The mixed canonical product state is equivalent to the Schmidt decomposition of a system of length L divided into a subsystem A from site 1 to l and a subsystem B from site $l+1$ to L. The mixed canonical state becomes

$$|\Psi\rangle = \sum_{a_l} \sqrt{\lambda_{a_l}} |a_l\rangle_A |a_l\rangle_B, \qquad (4.16)$$

where

$$|a_l\rangle_A = \sum_{\sigma_1,...,\sigma_l} \left(A^{\sigma_1}...A^{\sigma_{2l}}\right)(1, a_l) |\sigma_1, ..., \sigma_l\rangle, \qquad (4.17)$$

$$|a_l\rangle_B = \sum_{\sigma_{l+1},...,\sigma_L} (B^{\sigma_{l+1}}...B^{\sigma_L})(a_l, 1) |\sigma_{l+1}, ..., \sigma_L\rangle,$$

with $\{|a_l\rangle_A\}$ an orthonormal basis for the subsystem A and $\{|a_l\rangle_B\}$ an orthonormal basis for the subsystem B.

The matrices A and B involved in this representation can be, in principle, exponentially large, as the maximal dimension scales as $d^{L/2}$, thus their size has to be truncated in order to be numerically feasible. If the singular values decay fast enough we can employ a cutoff D in the sum from Eq. (4.17) and obtain a state that approximates $|\Psi\rangle$ the best, as in Eq. (4.4). This step

can be applied iteratively for $l = 1..L$, the error accumulated at each truncation is given by Eq. (4.4).

In order to act with an operator on a state represented as a matrix product state, it is useful to construct matrix product operators, analogue to the procedure presented above.

$$\hat{O} = \sum_{\vec{\sigma},\vec{\sigma}'} c_{(\sigma_1,...,\sigma_L),(\sigma_1',...,\sigma_L')} \ket{\vec{\sigma}} \bra{\vec{\sigma}'}, \tag{4.18}$$
$$= \sum_{\vec{\sigma},\vec{\sigma}'} W^{\sigma_1,\sigma_1'}...W^{\sigma_L,\sigma_L'} \ket{\vec{\sigma}} \bra{\vec{\sigma}'},$$

where the matrices $W^{\sigma,\sigma'}$ are analogous to the matrices M_σ, but with two physical indices, which represent the outgoing and ingoing states. If we act with a matrix product operator onto a matrix product state we obtain

$$\hat{O} \ket{\Psi} = \sum_{\vec{\sigma},\vec{\sigma}'} W^{\sigma_1,\sigma_1'}...W^{\sigma_L,\sigma_L'} \ket{\vec{\sigma}} \bra{\vec{\sigma}'} \left(\sum_{\vec{\sigma}''} M^{\sigma_1''}...M^{\sigma_L''} \ket{\vec{\sigma}''} \right), \tag{4.19}$$
$$= \sum_{\vec{\sigma},\vec{\sigma}'} W^{\sigma_1,\sigma_1'}...W^{\sigma_L,\sigma_L'} M^{\sigma_1'}...M^{\sigma_L'} \ket{\vec{\sigma}},$$
$$= \sum_{\vec{\sigma}} \left(\sum_{\sigma_1'} W^{\sigma_1,\sigma_1'} M^{\sigma_1'} \right)...\left(\sum_{\sigma_L'} W^{\sigma_L,\sigma_L'} M^{\sigma_L'} \right) \ket{\vec{\sigma}},$$
$$= \sum_{\vec{\sigma}} N^{\sigma_1}...N^{\sigma_L} \ket{\vec{\sigma}},$$

with $N^{\sigma_j}_{(b_{j-1}a_{j-1}'),(b_j a_j')} = \sum_{\sigma_j} W^{\sigma_j,\sigma_j'}_{b_{j-1},b_j} M^{\sigma_j'}_{a_{j-1}',a_j'}$ a matrix, such that the result is also a matrix product state. Note that the dimensions of the new matrices N are larger than the dimensions of the matrices M.

The matrix product state representation together with the approximation considering a cutoff D in the dimension of the matrices, can be employed to iteratively and variationally compute the ground state of a Hamiltonian, or to determine the time evolution of a system. In the following we present the ground state calculation with matrix product states, for some Hamiltonian $\hat{H}$. Firstly we write the Hamiltonian $\hat{H}$ in a matrix product operator representation (Eq.(4.18)) and the optimal approximation of the ground state will be given by a matrix product state $\ket{\Psi}$, with

4.2 The implementation of the algorithm

maximal dimension D, that minimizes the energy as

$$E = \frac{\langle \Psi | \hat{H} | \Psi \rangle}{\langle \Psi | \Psi \rangle}. \tag{4.20}$$

We solve this problem by minimizing the following quantity

$$\langle \Psi | \hat{H} | \Psi \rangle - \lambda \langle \Psi | \Psi \rangle , \tag{4.21}$$

where at the end of the minimization procedure, $|\Psi\rangle$ will be the ground state wavefunction and the Lagrange multiplier λ will be the ground state energy. We write the quantity from Eq. (4.21) in the matrix product representation and we iteratively optimize two matrices $M^{\sigma_j} M^{\sigma_{j+1}}$ at a time, while keeping all other M^{σ_i}, $i \neq j, j+1$ fixed. Afterwards we shift the optimized matrix pair $M^{\sigma_j} M^{\sigma_{j+1}}$ through the entire system. If the accuracy goal is not reached after optimizing the matrices at the edge of the system, $M^{\sigma_{L-1}} M^{\sigma_L}$, i.e. after performing a sweep, one performs another sweep optimizing all the matrices, until the error goal is reached. The optimization is performed by constructing a generalized eigenvalue problem and solving for the lowest eigenvector and eigenvalue, which will give us an estimate for the ground state energy. Because the dimensions of the matrices in the eigenvalue problem are, typically, too large for an exact diagonalization, an iterative eigensolver that aims for the lowest eigenvalue is used. In this work we use the Jacobi-Davidson method for large sparse matrices. One can make use of the symmetries of the Hamiltonian in order to restrict the DMRG search to the a certain symmetry sector, reducing the dimension of the subspace in which the search is performed, enhancing the efficiency of the algorithm. For the full description of the ground state search algorithm, the challenges that it involves and other applications of the matrix product states within the DMRG method see Ref. [121].

4.2. The implementation of the algorithm

For the implementation of the finite-size density matrix renormalization group (DMRG) we wrote a C++ code, using the ITensor Library [123]. ITensor is a C++ library for implementing tensor network calculations [123], developed by E. M. Stoudenmire and S.R. White. The code that we wrote, complementary to what exists in the ITensor Library, is listed in the Appendix and it consists in two header files and a main routine file. In the rest of the section we will briefly describe the structure of the code and the main features that we had to implement in

order to obtain the desired results. We will not discuss the syntax of the library, as it is not in the scope of this work and a complete documentation can be found in Ref. [123].

In the header file *bosehubbard.h* (see Appendix A.1), using the *SiteSet* class for specifying the local Hilbert space of each site of a lattice, we construct a class that contains the elements of the Bose-Hubbard model. We use the local number of bosons as the local quantum number and implement the possibility of defining a state by specifying the number of bosons on each site. As our model is particle conserving, the total number of bosons is a good quantum number and we restrict our ground-state search to a symmetry sector with a fixed number of bosons. We define the action of the creation and annihilation bosonic operators, and the number operator. The cutoff for local dimension of the Hilbert space can be passed as an argument of the created class.

In the DMRG routine one has to specify the number of sweeps as the stopping condition of the routine. Since we are considering parameters for several different phases in which the convergence of the method can vary, we introduce an error goal as the stopping condition in the DMRG routine. In the header file *dmrg_modified.h* (see Appendix A.2), if the energy difference between the last two sweeps is smaller than $10^{-8} J_\parallel$, the ground state search will stop and the resulting wavefunction will be our estimate for the ground state. Other modification is the introduction of the possibility to realize measurements of the expectation value of certain observables, e.g. H^2, in between the sweeps.

In the main file, *BH_ladder.cc* (see Appendix A.3), we start by reading the parameters of the model and the DMRG method from the input file. We continue by defining a series of states with different fillings and occupation patterns, that will be used as the initial states in the ground state search. The Hamiltonian is constructed using the operators previously defined and transformed in the matrix product operator representation using ITensor's *AutoMPO* function. The next step is to execute the DMRG sweeps and obtain the ground state estimate. In the following, we perform measurements on this wavefunction, thus we compute the expectation values of the: local and global density, the currents flowing on the rungs and legs of the ladder, the directed rung tunneling $\langle K_\perp \rangle$, the single particle correlations along the legs of the ladder, and the von Neumann entanglement entropy.

4.3. Convergence tests

We simulate the presented model Eq. (2.27) typically for a ladder with $L = 120$ rungs and with the bond dimension up to 1500 in the matrix product state representation. Since we are
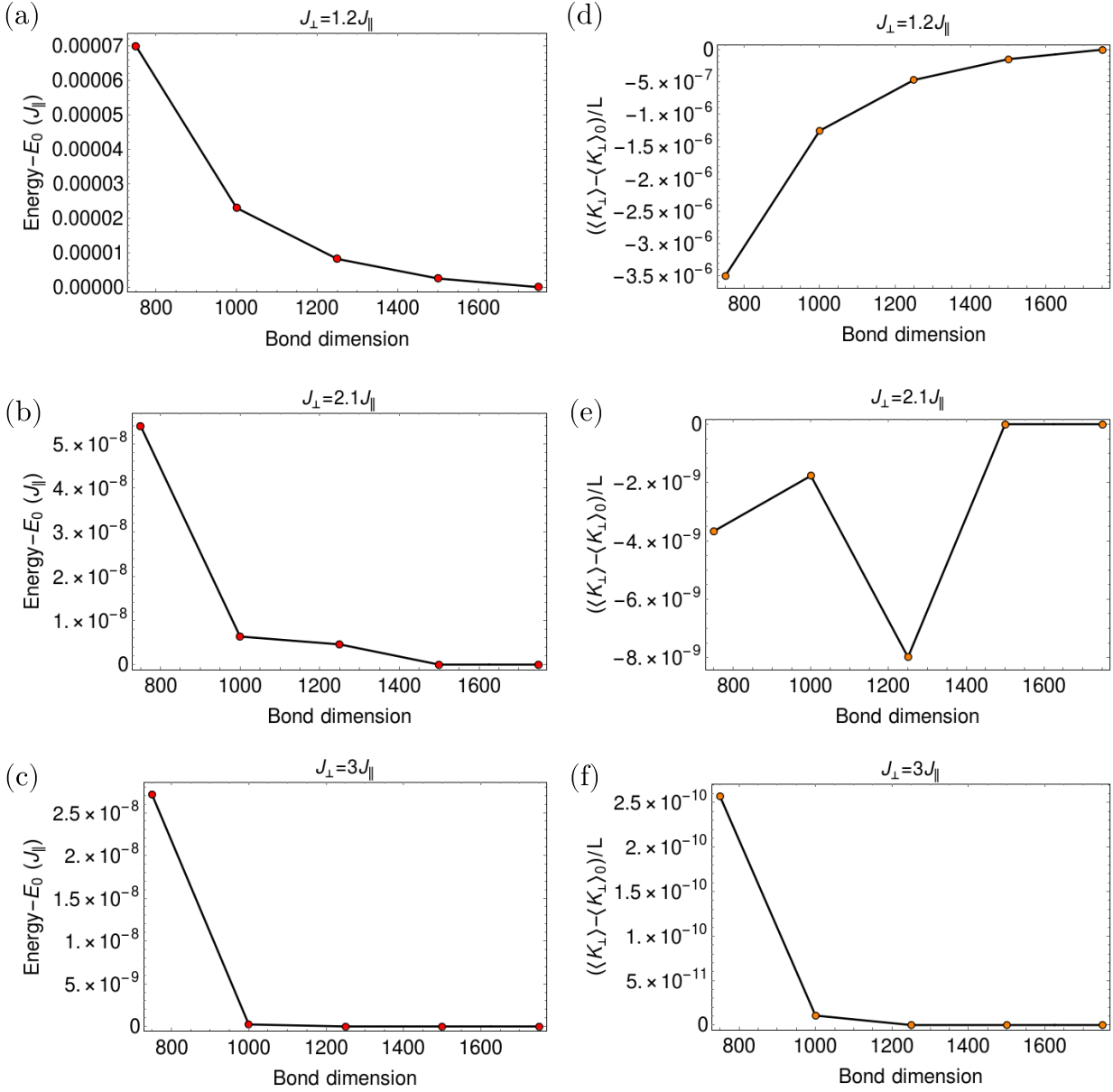
Figure 4.1.: (a)-(c) The energy of the ground state as a function of the bond dimension m used in the matrix product state representation compared to the energy, E_0, for $m = 1750$, for three value of the rung tunneling amplitude $J_\perp \in \{1.2, 2.1, 3\}J_\parallel$, which correspond to different phases. (d)-(f) The expectation value of the directed rung tunneling $\langle K_\perp \rangle/L$ as a function of the bond dimension m, compared to the value of the directed rung tunneling, $\langle K_\perp \rangle_0/L$, for $m = 1750$, for three value of the rung tunneling amplitude $J_\perp \in \{1.2, 2.1, 3\}J_\parallel$. The set of parameters used is $L = 240$, $\varphi = 0.9$, $\rho = 0.5$ and $U = 1.5J_\parallel$.

dealing with finite interactions the local Hilbert space of bosons is infinite, thus a cutoff for its dimension is needed. We use a maximal local dimension of five bosons per site.
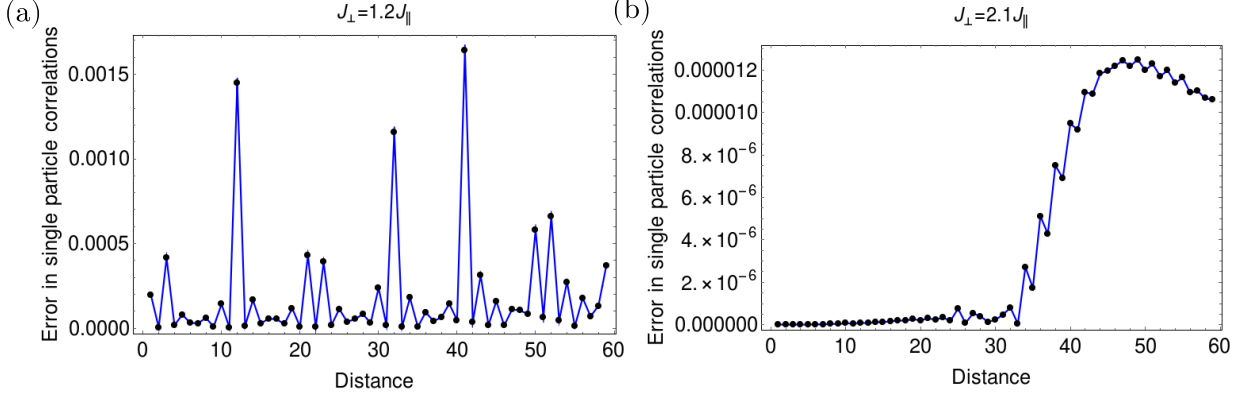
Figure 4.2.: (a) The relative error in the single particle correlations, $|(\xi(d)(m = 1750) - \xi(d)(m = 1500))/\xi(d)(m = 1750)|$, as a function of the distance, for (a) $J_\perp = 1.2J_\parallel$, (b) $J_\perp = 2.1J_\parallel$. The set of parameters used is $L = 240$, $\varphi = 0.9$, $\rho = 0.5$ and $U = 1.5J_\parallel$.

In this section we present the convergence checks of the method for different bond dimensions, m, and bosonic cutoffs, N_b, for a part of the parameter sets used in Chap.5. We will check the convergence with the aid of the following observable: the ground state energy, as the stopping condition of the algorithm is based on an error goal in the energy; the expectation value of the directed rung tunneling $\langle K_\perp \rangle / L$, because it is involved in the self-consistency and stability condition; the single particle correlations, $\xi(d) = \langle b^\dagger_{m,L/4} b_{m,L/4+d} + h.c. \rangle$, which exhibit, typically, the slowest converge.

4.3.1. Convergence of the method at $\varphi = 0.9$, $\rho = 0.5$ and $U = 1.5J_\parallel$

As the convergence of the algorithm can depend strongly on the nature of the ground state is, we consider different values of the rung tunneling amplitude $J_\perp$ which correspond to different phases. Thus in this section we consider: $J_\perp = 1.2J_\parallel$ when the state is a vortex superfluid; $J_\perp = 2.1J_\parallel$ when the state is a vortex lattice superfluid with a vortex density of $\rho_v = 1/2$; $J_\perp = 3J_\parallel$ when the state is a Meissner Mott-insulator (the full identification of these phases will be discussed in Chap.5).

In Fig. 4.1, we investigated the influence of the bond dimension used in the matrix product state representation for three value of the rung tunneling amplitude $J_\perp \in \{1.2, 2.1, 3\}J_\parallel$, on the ground state energy and the directed rung tunneling $\langle K_\perp \rangle$. The largest difference between the energy for $m = 1500$ and $m = 1750$, appears of $J_\perp = 1.2J_\parallel$ (see Fig. 4.1(a)), and it is of
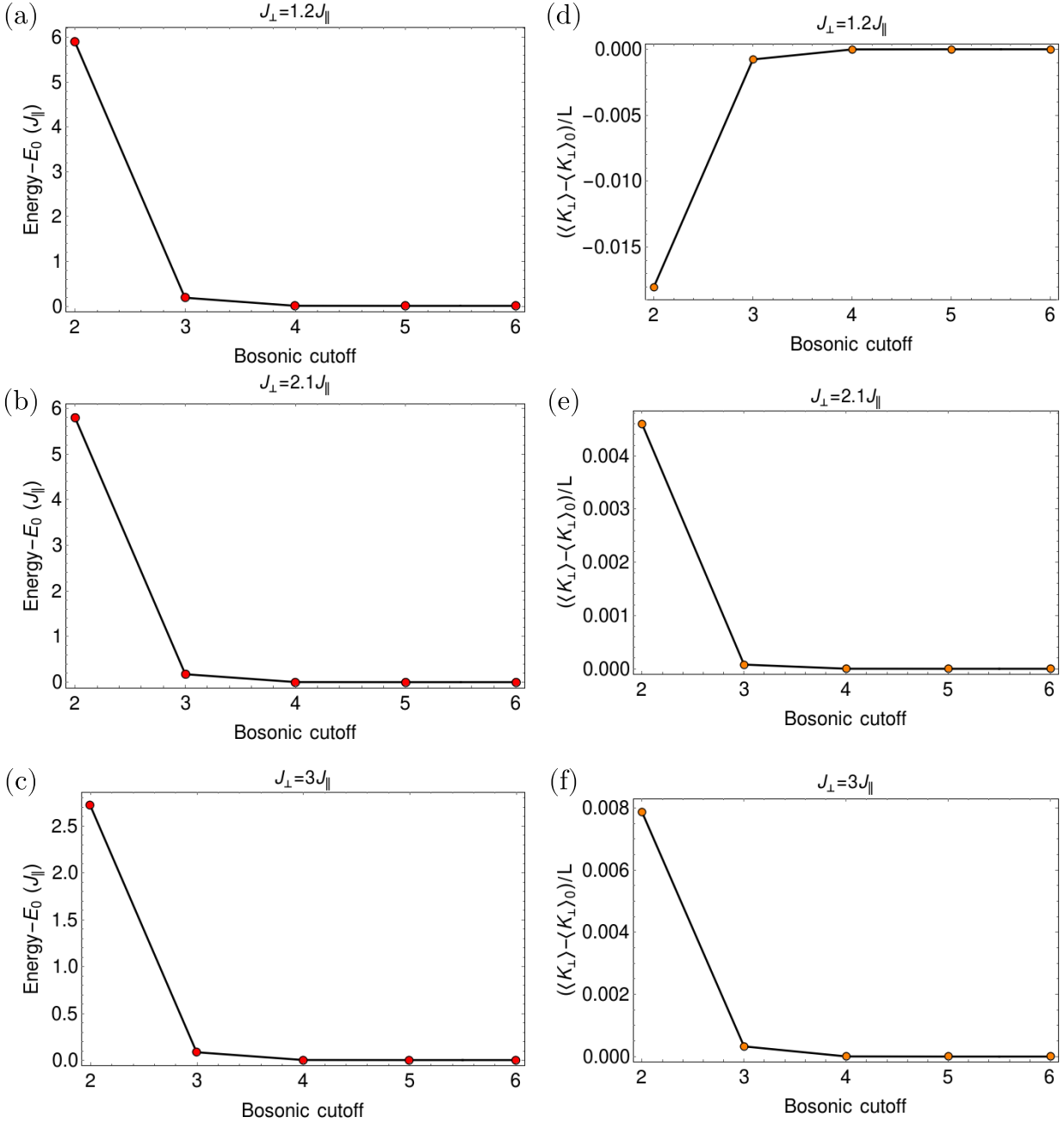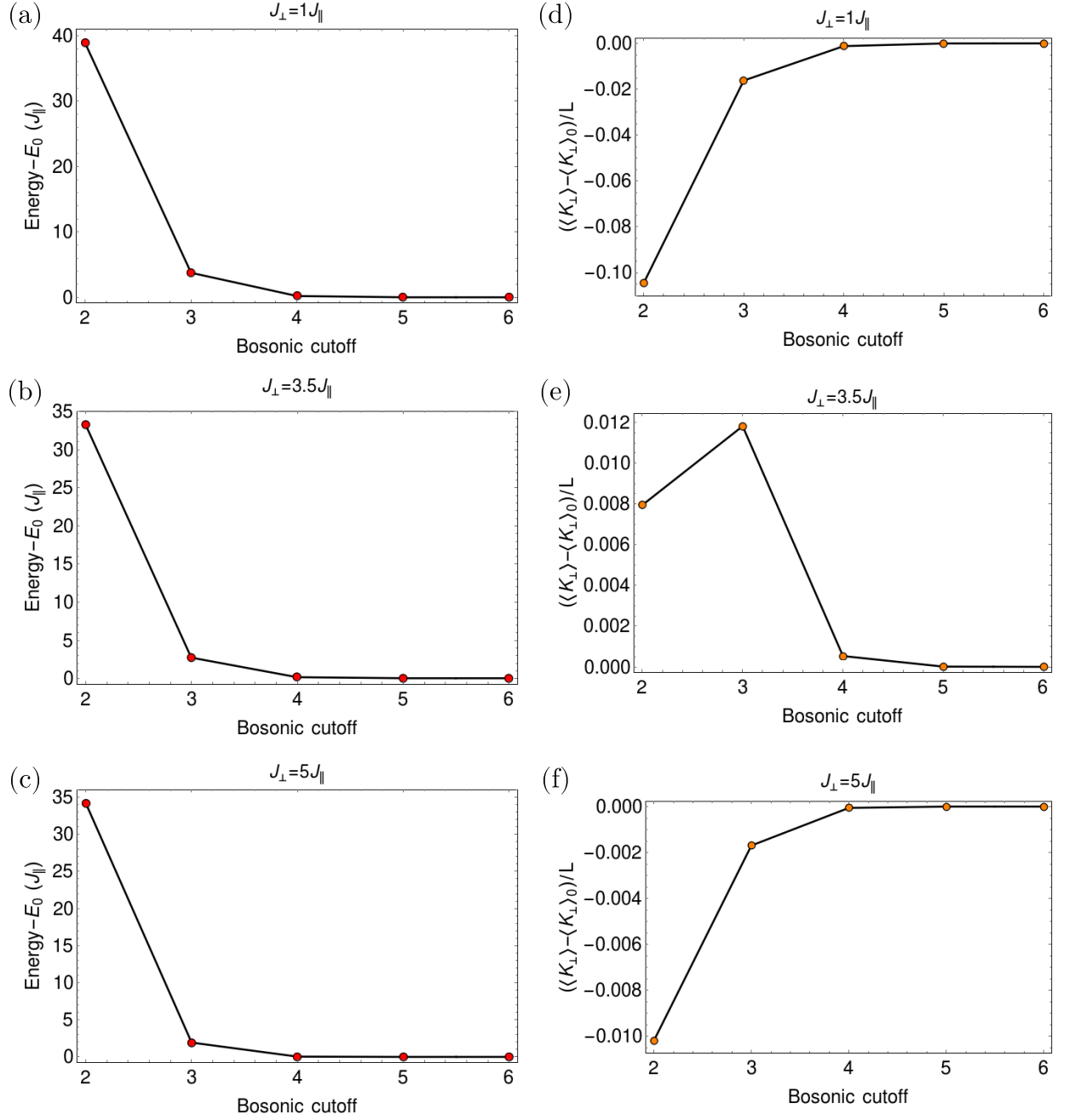
Figure 4.3.: (a)-(c) The energy of the ground state as a function of the bosonic cutoff of the local dimension N_b, compared to the energy, E_0, for $N_b = 6$, for three value of the rung tunneling amplitude $J_\perp \in \{1.2, 2.1, 3\} J_\parallel$, which correspond to different phases. The energy is measured in units of $J_\parallel$. (d)-(f) The expectation value of the directed rung tunneling $\langle K_\perp \rangle / L$ as a function of the bosonic cutoff of the local dimension N_b, compared to the value of the directed rung tunneling, $\langle K_\perp \rangle_0 / L$, for $N_b = 6$, for three value of the rung tunneling amplitude $J_\perp \in \{1.2, 2.1, 3\} J_\parallel$. The set of parameters used is $L = 240$, $\varphi = 0.9$, $\rho = 0.5$ and $U = 1.5 J_\parallel$.

the order of $10^{-6}J_{\parallel}$. In the case of $\langle K_{\perp} \rangle / L$, for the same value of $J_{\perp} = 1.2J_{\parallel}$ (Fig. 4.1(d)), the difference between the value at $m = 1500$ and the value at $m = 1750$ is of the order of 10^{-7}. For the other two values of $J_{\perp}$ depicted in Fig. 4.1, the error in the ground state energy is under $10^{-8}J_{\parallel}$, which is the error goal of the method. One should not give an interpretation to the variations in the expectation values of the observable which are under the error goal of the method, as the non-monotonic behavior of $\langle K_{\perp} \rangle / L$ in Fig. 4.1(e), as they are affected by numerical noise.

In Fig. 4.2, we have represented the relative error in the single particle correlations, $|(\xi(d)(m = 1750) - \xi(d)(m = 1500))/\xi(d)(m = 1750)|$, we can see that the error does not exceed 0.1%. Under these considerations we are confident that the choice of the bond dimension $m = 1500$ is appropriate for this system length and set of parameters. For $J_{\perp} = 1.2J_{\parallel}$ the single particle correlations show an oscillating behavior, thus we can explain the peaks in the relative error from Fig. 4.2(a) as due to the error in the period of the oscillations of the single particle correlations.

The next step consists in looking at the influence of the bosonic cutoff of the local dimension, Fig. 4.3. The difference of the ground state energy computed with a local dimension of five bosons per site and ground state energy computed with a local dimension of six bosons per site, is of the order of $10^{-6}J_{\parallel}$ for $J_{\perp} = 1.2J_{\parallel}$ and $J_{\perp} = 2.1J_{\parallel}$, and of the order of $10^{-4}J_{\parallel}$ for $J_{\perp} = 3J_{\parallel}$. The change in the expectation value of the directed rung tunneling $\langle K_{\perp} \rangle / L$ computed with a local dimension of five bosons per site and with a local dimension of six bosons per site is smaller than 10^{-6}, for all values of $J_{\perp}$ represented in Fig. 4.3(d)-(f). Thus, we can see that the results obtained for a local dimension of five and six bosons per site are consistent.

4.3.2. Convergence of the method at $\varphi = 0.8$, $\rho = 0.8$ and $U = 1J_{\parallel}$

In this section we consider the following phases: a vortex superfluid phase with $J_{\perp} = 1J_{\parallel}$; a biased ladder phase with $J_{\perp} = 3.5J_{\parallel}$; a Meissner superfluid with $J_{\perp} = 5J_{\parallel}$.

In Fig. 4.4, we investigated the influence of the bond dimension used in the matrix product state representation for three value of the rung tunneling amplitude $J_{\perp} \in \{1, 3.5, 5\}J_{\parallel}$, on the ground state energy and the directed rung tunneling $\langle K_{\perp} \rangle$. The difference between the energy for $m = 1500$ and $m = 1750$ is of the order of $10^{-6}J_{\parallel}$ for $J_{\perp} = 1J_{\parallel}$ (see Fig. 4.4(a)), while for the other two values of $J_{\perp}$ is under the desired energy error goal of $10^{-8}J_{\parallel}$, (see Fig. 4.4(b)-(c)). The deviations from a monotonic behavior from Fig. 4.4(c) are due to numerical noise. In the
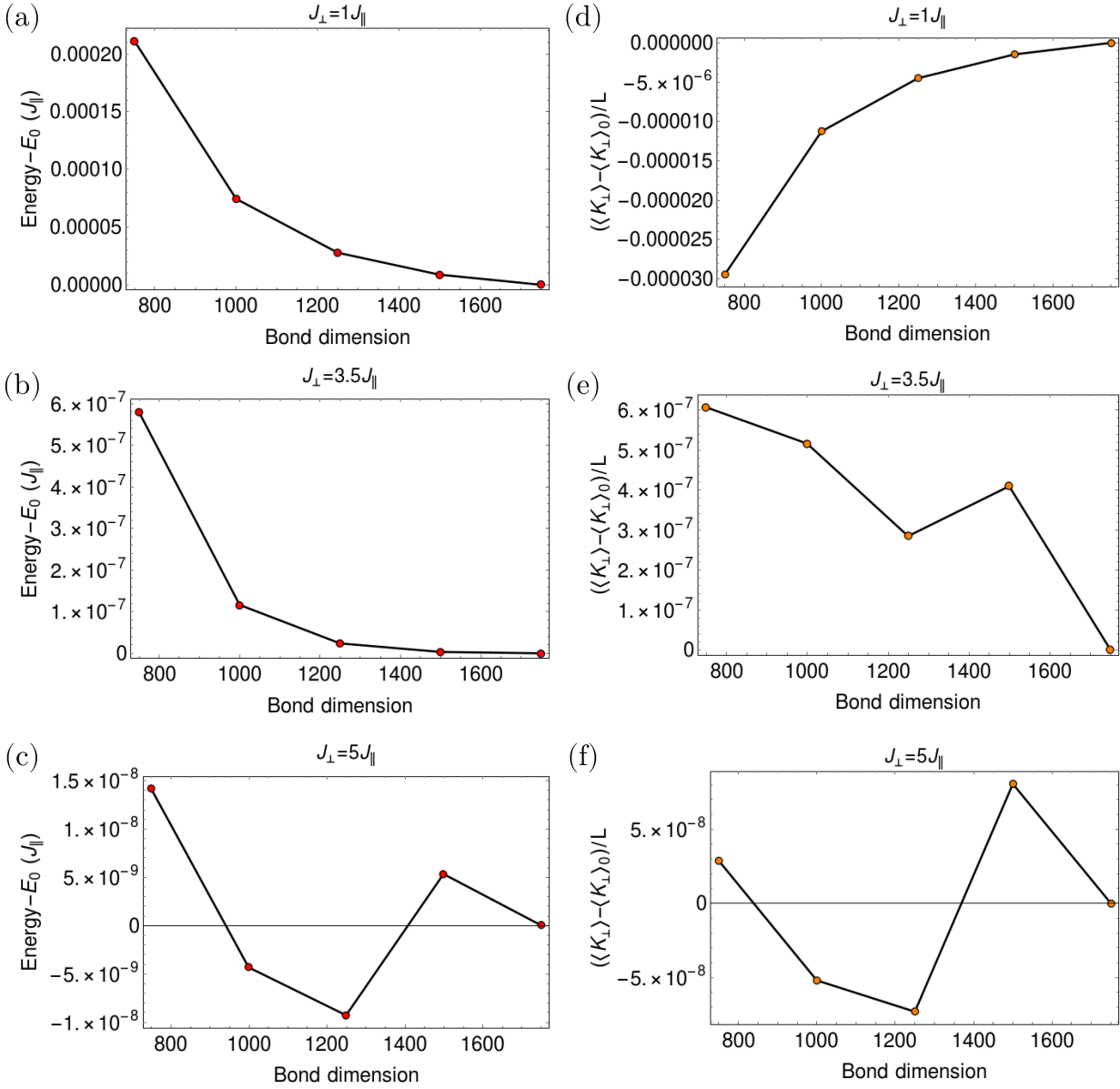
Figure 4.4.: (a)-(c) The energy of the ground state as a function of the bond dimension m used in the matrix product state representation compared to the energy, E_0, for $m = 1750$, for three value of the rung tunneling amplitude $J_\perp \in \{1, 3.5, 5\}J_\parallel$, which correspond to different phases. The energy is measured in units of $J_\parallel$. (d)-(f) The expectation value of the directed rung tunneling $\langle K_\perp \rangle / L$ as a function of the bond dimension m, compared to the value of the directed rung tunneling, $\langle K_\perp \rangle_0 / L$, for $m = 1750$, for three value of the rung tunneling amplitude $J_\perp \in \{1, 3.5, 5\}J_\parallel$. The set of parameters used is $L = 240$, $\varphi = 0.8$, $\rho = 0.8$ and $U = 1J_\parallel$.

Figure 4.5.: (a)-(c) The energy of the ground state as a function of the bosonic cutoff of the local dimension N_b, compared to the energy, E_0, for $N_b = 6$, for three value of the rung tunneling amplitude $J_\perp \in \{1, 3.5, 5\}J_\parallel$, which correspond to different phases. The energy is measured in units of $J_\parallel$. (d)-(f) The expectation value of the directed rung tunneling $\langle K_\perp \rangle / L$ as a function of the bosonic cutoff of the local dimension N_b, compared to the value of the directed rung tunneling, $\langle K_\perp \rangle_0 / L$, for $N_b = 6$, for three value of the rung tunneling amplitude $J_\perp \in \{1, 3.5, 5\}J_\parallel$. The set of parameters used is $L = 240$, $\varphi = 0.8$, $\rho = 0.8$ and $U = 1J_\parallel$.

case of $\langle K_\perp \rangle / L$ the difference between the value at $m = 1500$ and the value at $m = 1750$ is of the order of 10^{-6}, for $J_\perp = 1 J_\parallel$, of the order of 10^{-7}, for $J_\perp = 3.5 J_\parallel$, and of the order of 10^{-8}, for $J_\perp = 5 J_\parallel$ (Fig. 4.4(d)-(f)). Thus, a bond dimension of $m = 1500$ is appropriate for capturing the properties of the mentioned phases.

The effect of the bosonic cutoff of the local dimension is presentend in Fig. 4.5. The difference of the ground state energy computed with a local dimension of five bosons per site and ground state energy computed with a local dimension of six bosons per site, is of the order of $10^{-3} J_\parallel$ for $J_\perp = 1 J_\parallel$ and $J_\perp = 3 J_\parallel$, and of the order of $10^{-4} J_\parallel$ for $J_\perp = 5 J_\parallel$. The change in the expectation value of the directed rung tunneling $\langle K_\perp \rangle / L$ computed with a local dimension of five bosons per site and with a local dimension of six bosons per site is smaller than 10^{-5}, for all values of $J_\perp$ represented in Fig. 4.5(d)-(f). Even though the error in the ground state energy due to the cutoff of the local dimension is several order of magnitude larger than the other errors in energy presented so far in this section, we are confident that it is still small enough such that it does not have an effect on the nature of the phase.

In Fig. 4.6, we observe that the relative error in the single particle correlations is under 1% in the biased ladder phase. Thus a cutoff of the local dimension of five bosons per site represents an optimal trade-off between computational costs and good results.
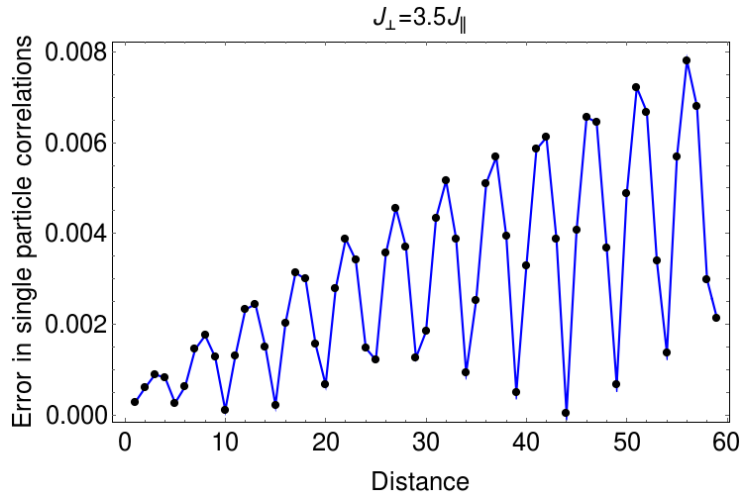
Figure 4.6.: The relative error in the single particle correlations, $|(\xi(d)(N_b = 6) - \xi(d)(N_b = 5))/\xi(d)(N_b = 6)|$, as a function of the distance, for $J_\perp = 3.5 J_\parallel$, $L = 240$, $\varphi = 0.8$, $\rho = 0.8$ and $U = 1 J_\parallel$.

4.4. The challenges of numerically stabilizing the biased ladder phase

In this section we will analyze the procedure we employ in order to numerically stabilize the biased ladder phase, introduced in Ref. [98]. The biased ladder phase spontaneously breaks the $\mathbb{Z}_2$ symmetry between the two legs of the ladder, thus the ground state is two-fold degenerate. The DMRG ground state search can choose any state within this degenerate subspace, resulting in an arbitrary value of the density imbalance between zero and the maximal value. In order to unequivocally identify the extend of the biased ladder ladder we want to obtain the ground state with maximal value of the imbalance Δn, defined by Eq. (3.65). After numerically obtaining one of the ground states, $|\psi_1\rangle$, we compute the orthogonal wavefunction, $|\psi_2\rangle$, which is degenerate in energy with $|\psi_1\rangle$. For this, the second ground state search is performed enforcing the orthogonality by the following Hamiltonian

$$\tilde{H} = H + w \, |\psi_1\rangle \langle \psi_1| , \tag{4.22}$$

where H is the Hamiltonian given in Eq. (2.27) and the weight $w > 0$ introduces an energy penalty for any finite overlap with $|\psi_1\rangle$ and guarantees the orthogonality with it, to a good accuracy. We use a typical value of $w = 10 J_\parallel$ and checked the consistency with higher values up to $w = 100 J_\parallel$. As an initial state for the DMRG search we use a state with an inverse density imbalance compared to the state $|\psi_1\rangle$. Having obtained an orthonormal basis in the ground state manifold, $\{|\psi_1\rangle, |\psi_2\rangle\}$, we move on to construct the superposition of these two states

$$|\psi_\lambda\rangle = \lambda \, |\psi_1\rangle + \sqrt{1 - \lambda^2} \, |\psi_2\rangle , \tag{4.23}$$

with $\lambda \in [0, 1]$, and maximize the density imbalance Δn as a function of the variational parameter λ

$$\Delta n_{max} = \max_{\lambda \in [0,1]} \left| \langle \psi_\lambda | \sum_j (n_{0,j} - n_{1,j}) | \psi_\lambda \rangle \right|. \tag{4.24}$$

After calculating $|\psi_1\rangle$ in the first DMRG search and $|\psi_2\rangle$ in the second one, we need to check if they have the same energy in order to confirm the degeneracy of the ground state. In Fig. 4.7, we represented the energy difference between $|\psi_1\rangle$ and $|\psi_2\rangle$ and we observe that for $2.7 J_\parallel \leq J_\perp \leq 3.9 J_\parallel$ the ground state is degenerate.

In Fig. 4.8(a), we computed the density imbalance between the two legs of the ladder for $|\psi_\lambda\rangle$ (Eq, (4.23)) as a function of the variational parameter λ, for the parameters $L = 120$, $\varphi = 0.8$,

4.4 The challenges of numerically stabilizing the biased ladder phase
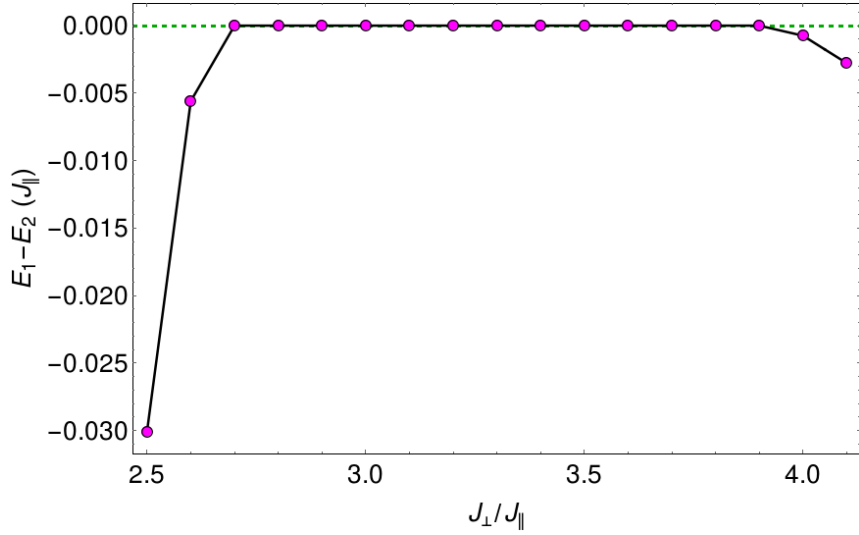
Figure 4.7.: (a) The energy difference between the energy of the ground state $|\psi_1\rangle$, E_1, and the energy of the first orthogonal state $|\psi_2\rangle$, E_2, for the parameters $L = 120$, $\varphi = 0.8$, $\rho = 0.8$ and $U = 1J_\parallel$.
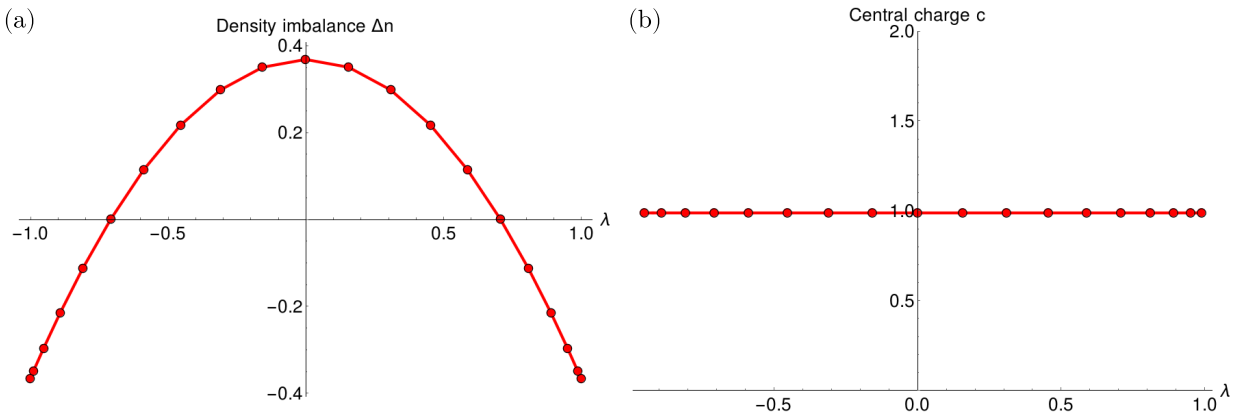
Figure 4.8.: (a) The density imbalance, (b) the central charge computed for the state $|\psi_\lambda\rangle$ as a function of λ, for the parameters $L = 120$, $\varphi = 0.8$, $\rho = 0.8$, $U = 1J_\parallel$, and $J_\perp = 3.5J_\parallel$.

$\rho = 0.8$, $U = 1J_\parallel$ and $J_\perp = 3.5J_\parallel$. The maximal value of the imbalance is $\Delta n = 0.3675$. The finite density imbalance indicates that we are in the biased ladder phase, this is also confirmed by looking at the central charge as a function of λ (see Fig. 4.8(b)) which is close to 1 for all values of λ. For $J_\perp = 3.5J_\parallel$ we have a degenerate ground state, as the energy difference is approximately 0, $|E_1 - E_2| < 10^{-8}J_\parallel$ (see Fig. 4.7).

In the following we will compare this method with a procedure that uses an induced symmetry breaking by an externally applied potential [80]. In this case one performs the ground state search with the following Hamiltonian

$$\tilde{H} = H + \sum_{m,j}(-1)^m \mu_j n_{m,j}, \tag{4.25}$$

with H given by Eq. (2.27) and μ the external potential that breaks the $\mathbb{Z}_2$ symmetry of the model. One has to perform the ground state search for different values of μ and compute the density imbalance and use the data $\Delta n(\mu)$ to extrapolate the value of the imbalance in the limit of zero external potential, $\mu = 0$.
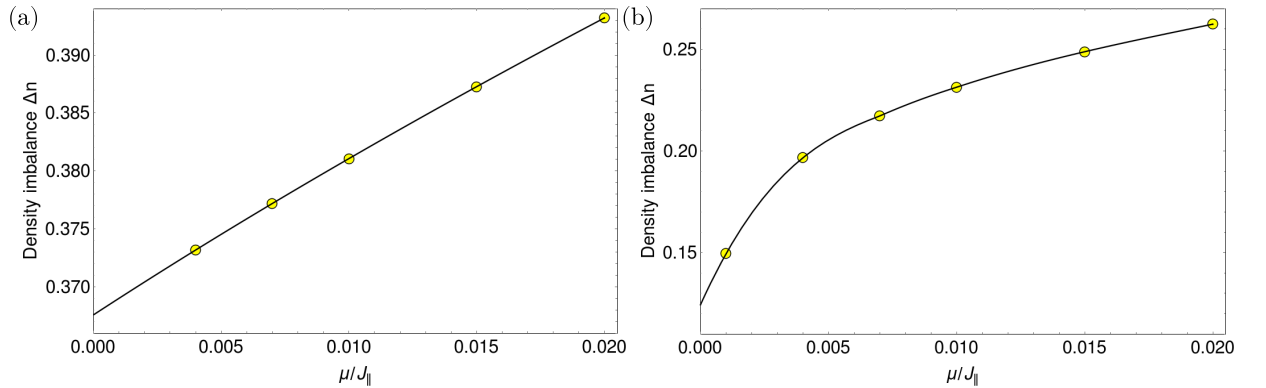
Figure 4.9.: The density imbalance as a function of the external bias potential, μ, for the parameters $L = 120$, $\varphi = 0.8$, $\rho = 0.8$, $U = 1J_\parallel$ and (a) $J_\perp = 3.5J_\parallel$, (b) $J_\perp = 4J_\parallel$. We extrapolate the of the imbalance towards zero external potential, $\mu = 0$

If we compare the previous result with the one obtained with the method of applying an external potential, for $J_\perp = 3.5J_\parallel$, the value of the imbalance agrees up to the fourth digit, $\Delta n = 0.3675$. The density imbalance as a function of the external potential and the extrapolation towards $\mu = 0$ can be seen in Fig. 4.9(a), for $J_\perp = 3.5J_\parallel$.

Inside the biased ladder phase the two methods are matching really well. The differences arise when you consider a point outside this phase, for example $J_\perp = 4J_\parallel$ (that corresponds to the
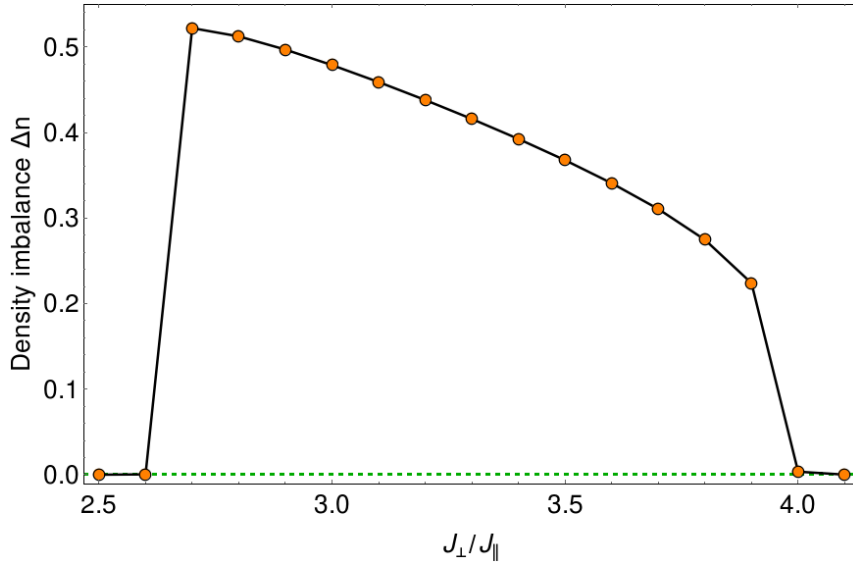
Figure 4.10.: The density imbalance as a function of the rung tunneling amplitude $J_\perp$, for the parameters $L = 120$, $\varphi = 0.8$, $\rho = 0.8$ and $U = 1J_\parallel$. The density imbalance has been computed using Eq. (4.24) if we have a degenerate ground state, i.e. $E_1 - E_2 = 0$, and as the imbalance of the ground state $|\psi_1\rangle$ otherwise.

Meissner superfluid phase, as we will see in Chap. 5). If we look in Fig. 4.7, we can see that the energy difference between the two orthogonal states is finite, $|E_1 - E_2| > 0$, which indicates that $|\psi_2\rangle$ is an excited state and we do not have a degenerate ground state. But for the method with an external field the extrapolation towards zero external potential seems to show a finite value of the density imbalance, see Fig. 4.9(b). We see a different behavior of Δn as a function of μ compared to the case $J_\perp = 3.5J_\parallel$ (Fig. 4.9(a)), such that it is not clear that if one considers smaller values of the external potential, the imbalance still has a finite value.

In Fig. 4.10, we have plotted the density imbalance for the parameters $L = 120$, $\varphi = 0.8$, $\rho = 0.8$ and $U = 1J_\parallel$. For the values of $J_\perp$ for which the ground state is degenerate, i.e. $E_1 - E_2 = 0$ in Fig. 4.7, we employed the method described in the beginning to compute the imbalance, Eq. (4.24), and as the imbalance of the ground state $|\psi_1\rangle$ otherwise. We found this method to more reliably identify the imbalanced phase, compared to the induced symmetry breaking by an externally applied potential.

5. Numerical Results

5.1. Self-consistent solutions

In the following sections we determine the stable steady states of the coupled cavity-atomic model for different parameter sets. In order to do this we use the three steps outlined in Ref. [98], first we perform a ground-state search using the DMRG method for the effective model Eq. (2.27), for fixed flux φ, filling ρ and on-site interaction $U/J_\parallel$, while varying the rung tunneling amplitude $J_\perp/J_\parallel$. We compute the expectation value $\langle K_\perp \rangle$ obtaining its dependence on $J_\perp/J_\parallel$. In the second step we find the solution of the self-consistent problem reformulated as

$$\frac{\langle K_\perp \rangle}{L} = \frac{J_\parallel}{AL}\frac{J_\perp}{J_\parallel}. \tag{5.1}$$

The left-hand side contains the nonlinear behavior of $\langle K_\perp \rangle$ given by the effective model and the right-hand side is a linear function with slope $\frac{J_\parallel}{AL}$. In a graphical interpretation, the solutions are determined as the crossings of the two curves. The last step is to work out which of these solutions are stable. The stability condition, Eq. (2.34), tells us that we need to compare the slope of the two curves at their intersection point(s). The solution is stable if the slope of $\langle K_\perp \rangle/L$ is smaller than the slope of the linear function. We evaluate the derivative numerically by computing the left and right finite derivatives with the help of the two adjacent points. We consider a solution stable if both the left and right finite derivatives satisfy the condition given by Eq. (2.34).

In the next two sections we extend the results we presented in Ref. [98], for more values of the interaction strength. For the parameter sets that overlap with the ones presented in Ref. [98], the figures are adapted from the mentioned work.

5.2. Steady state diagram at flux $\varphi = 0.9$ and filling $\rho = 0.5$

In this section, we will present which steady states can be dynamically organized for the parameters $\varphi = 0.9$ and $\rho = 0.5$, for three values of the interaction strength $U \in \{1.5J_\parallel, 2J_\parallel, 2.5J_\parallel\}$. We show that a dynamical stabilization of a vortex superfluid, a $VL_{1/2}$-SF, and a Meissner Mott-insulating state is possible. In Fig. 5.1 (a),(c),(e) the expectation value of the directed rung tunneling $\langle K_\perp \rangle/L$ has been plotted for $L = 120$ and $L = 60$. In all the three cases, for small $J_\perp$, corresponding to the vortex phases, $\langle K_\perp \rangle$ increases rapidly with $J_\perp$, whereas for large $J_\perp$, in

5.2 Steady state diagram at flux $\varphi = 0.9$ and filling $\rho = 0.5$
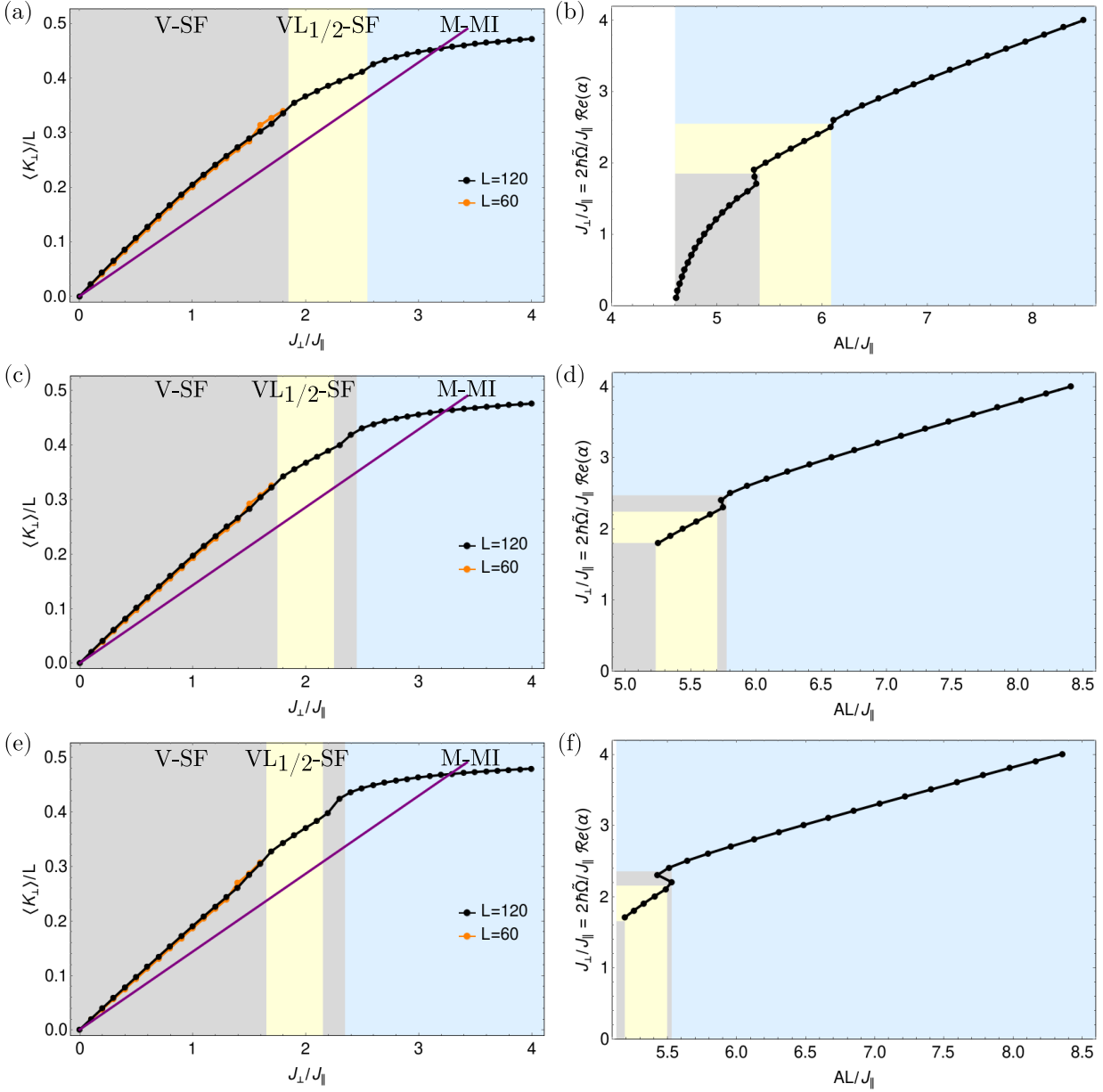
Figure 5.1.: On the left is graphical interpretation of the self-consistency condition for the parameters $\varphi = 0.9$, $\rho = 0.5$ with (a) $U = 1.5J_\parallel$, (c) $U = 2J_\parallel$, (e) $U = 2.5J_\parallel$. The directed rung tunneling $\langle K_\perp \rangle / L$ is represented for two system sizes, $L = 120$ and $L = 60$. The straight (purple) line represents the right-hand side of the self-consistency condition, which is a linear function with slope $\frac{J_\parallel}{AL}$. The crossings of the two curves give the solutions of the self-consistency condition. On the right are plotted the solutions $J_\perp / J_\parallel$ of the self-consistency equation which are proportional to the cavity field $Re(\alpha)$ versus the pump strength $AL/J_\parallel$, for (b) $U = 1.5J_\parallel$, (d) $U = 2J_\parallel$, (f) $U = 2.5J_\parallel$. The filled colored areas represent the extent of different phases. In the grey area the stability of the solutions is not clear for all system sizes.

the Meissner phase, $\langle K_\perp \rangle$ has a slow increase. In the regime where the two system sizes agree (for $J_\perp > 1.8J_\parallel$), $\langle K_\perp \rangle$ is monotonic and concave, with small jumps near the phase transitions, these jumps become more evident for higher interaction, $U = 2J_\parallel$ and $U = 2.5J_\parallel$. From the intersection of this curve with a line with the slope $\frac{J_\parallel}{AL}$ and checking the stability condition (2.34), we compute the stable solutions plotted in Fig. 5.1 (b),(d),(f).

For $U = 1.5J_\parallel$ and the size $L = 120$ a stable solution can be found in the entire parameter regime shown, beside close to the phase transitions. For smaller systems for $U = 1.5J_\parallel$ it is not clear that a stable solution exists for $J_\perp < 1.8J_\parallel$. For the other two values of the interaction considered, the stability of the solutions cannot be decided from the available data for small values of $J_\perp$. Due to the shape of $\langle K_\perp \rangle$, one can find non-trivial solutions above a certain value of the pump strength $A \approx 4.6J_\parallel/L$ (see Fig. 5.1(b)), where the cavity field takes a finite value. The coupling between a many-body system and an optical cavity can result in the presence of bifurcation points in its phase diagram [100]. In the case of $U = 1.5J_\parallel$ and $L = 120$ we can see that around $A \approx 4.6J_\parallel/L$ the steady state diagram shows a transition from a trivial stable solution to one of the two nontrivial solutions, $J_\perp(A)$ or $-J_\perp(A)$. In the regions where the phase transitions take place $5.3J_\parallel/L \lesssim A \lesssim 5.4J_\parallel/L$ and $6.07J_\parallel/L \lesssim A \lesssim 6.1J_\parallel/L$, for $U = 1.5J_\parallel$; $5.7J_\parallel/L \lesssim A \lesssim 5.8J_\parallel/L$, for $U = 2J_\parallel$; and $5.4J_\parallel/L \lesssim A \lesssim 5.55J_\parallel/L$, for $U = 2.5J_\parallel$ multiple solutions of the self-consistency condition can exist for the same value of the pump strength. Due to the limited numerical resolution, we cannot decide which solutions are stable.

In the following, we characterize the steady states which correspond to the stable solutions. As the considered values of the interaction strength do not change the nature of the phases and only change the phase transitions points, we will, firstly, do the analysis for $U = 1.5J_\parallel$ and, afterwards, mention the changes that appear while increasing the interaction to $U = 2J_\parallel$ and $U = 2.5J_\parallel$.

In Fig. 5.2(a), we can see that below $A \lesssim 6.1J_\parallel/L$ the rung currents take finite values which indicates a vortex state. A clear abrupt change of the rung current and other observables signals another transition between states at approximately $5.3J_\parallel/L \lesssim A \lesssim 5.4J_\parallel/L$. The vortex state in between $5.4J_\parallel/L \lesssim A \lesssim 6.1J_\parallel/L$ is characterized by a stable vortex density $\rho_v = 1/2$ (Fig. 5.3(a)) which points towards a VL$_{1/2}$-SF state. This state is confirmed by the value of the central charge $c \approx 1$ (Fig. 5.2(b)) and the algebraic decay of the single particle correlation functions (Fig. 5.4(a)). We observe that in the VL$_{1/2}$-SF phase the chiral current changes its sign due to the increase of the unit cell, as explained in Refs. [79, 80]. The VL$_{1/2}$-SF state can be
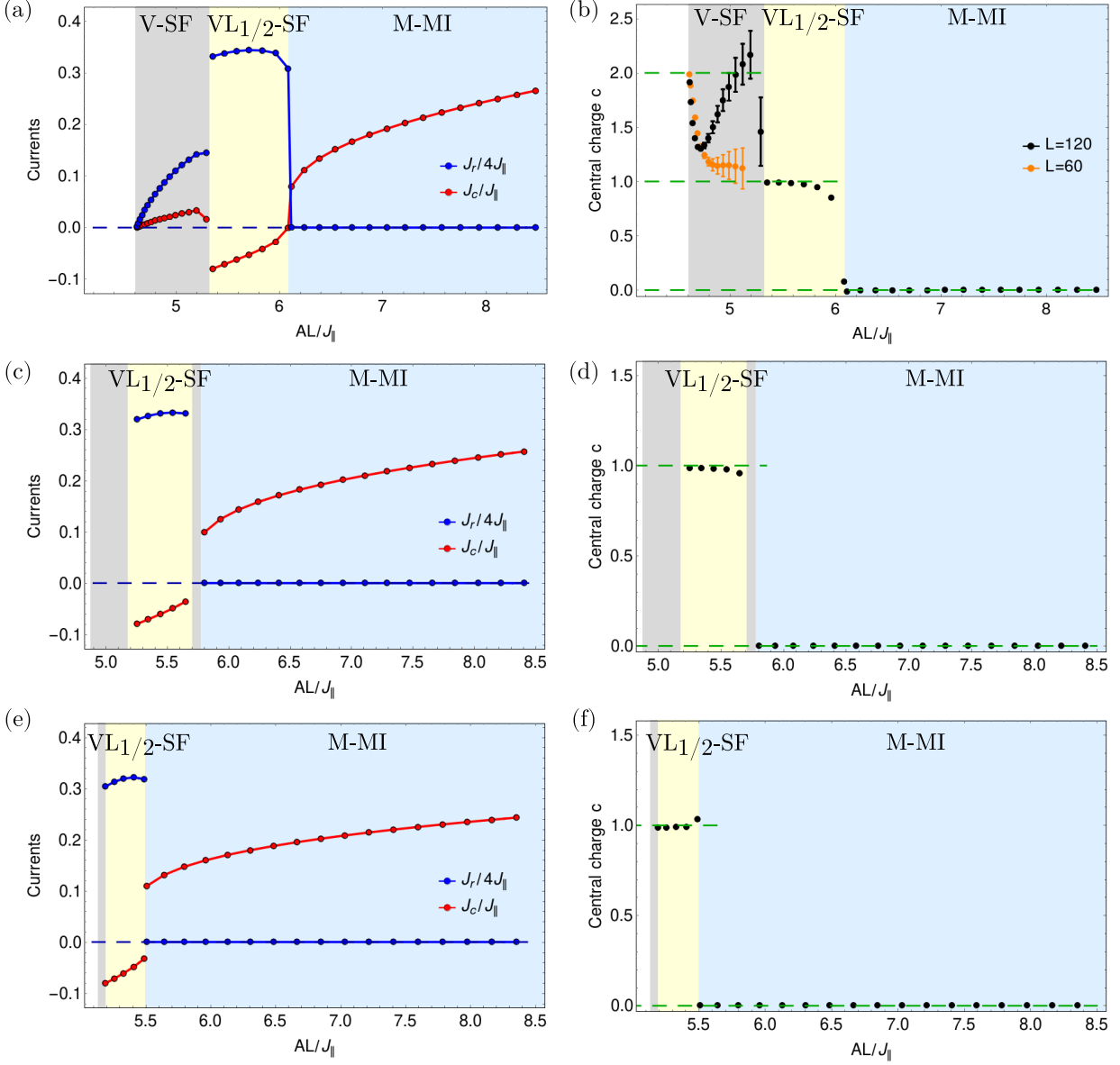
Figure 5.2.: The chiral current J_c and the average rung current J_r as a function of the pump strength $AL/J_\parallel$, for the parameters $\varphi = 0.9$, $\rho = 0.5$ with (a) $U = 1.5J_\parallel$, (c) $U = 2J_\parallel$, (e) $U = 2.5J_\parallel$. The central charge c, computed from the scaling of entanglement entropy, for (b) $U = 1.5J_\parallel$, (d) $U = 2J_\parallel$, (f) $U = 2.5J_\parallel$. The errorbars represented the fit error. In the vortex superfluid region we represented the value of the central charge for two system sizes, $L = 120$ and $L = 60$, which shows a strong size dependent behavior. Dashed horizontal lines indicate the constant value 0, 1 or 2, as a guide to the eye.
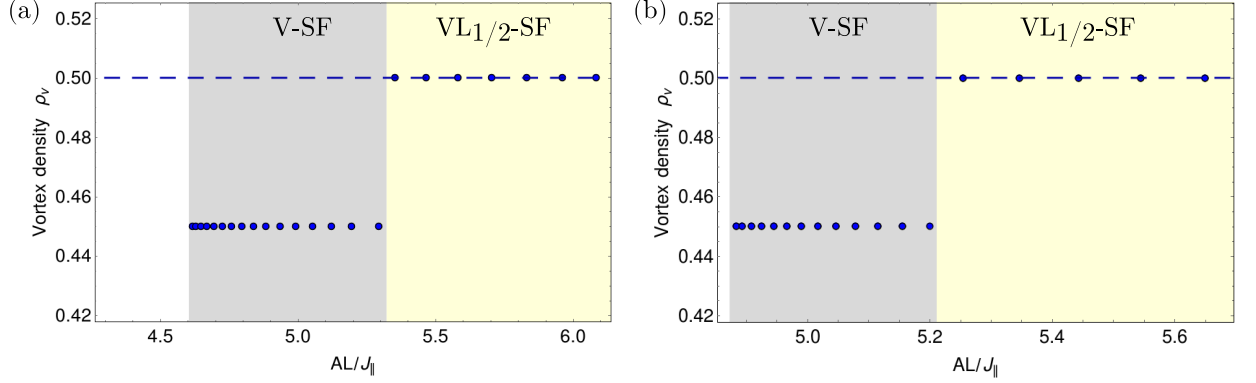
Figure 5.3.: The vortex density ρ_v as a function of the pump strength $AL/J_\parallel$, where the rung current is finite for the parameters $\varphi = 0.9$, $\rho = 0.5$, with (a) $U = 1.5J_\parallel$, (b) $U = 2J_\parallel$. The vortex density has the value $\rho_v = 1/2$ for (a) $5.3J_\parallel/L \lesssim A \lesssim 6.1J_\parallel/L$, (b) $5.21J_\parallel/L \lesssim A \lesssim 5.7J_\parallel/L$, which represents the VL$_{1/2}$-SF phase. Dashed horizontal line indicates the constant value $1/2$.
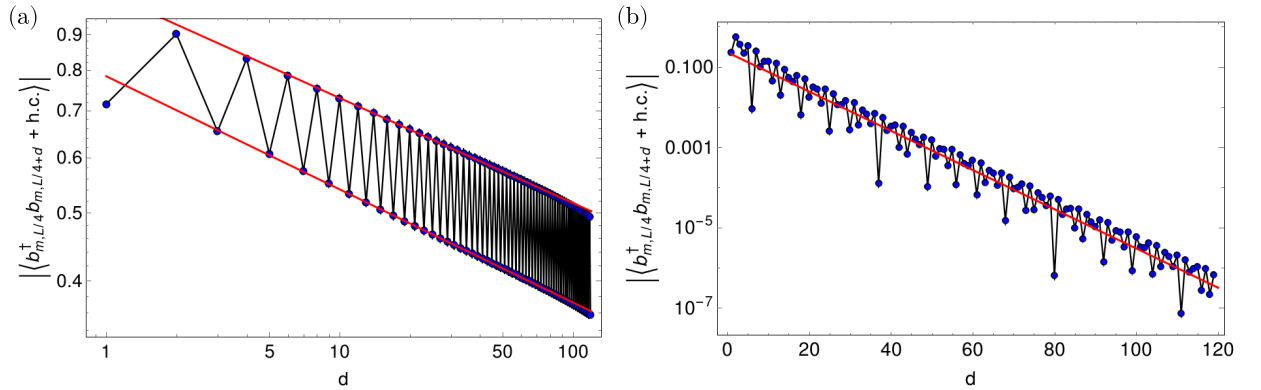
Figure 5.4.: The absolute value of the single particle correlations, $|\langle b_{m,L/4}^\dagger b_{m,L/4+d} + h.c.\rangle|$, (a) in a logarithmic plot, in the vortex lattice phase and (b) in a semi-logarithmic plot, in the Meissner phase, for $L = 240$, $\varphi = 0.9$, $\rho = 0.5$ and $U = 1.5J_\parallel$, (a) $A = 5.46J_\parallel/L$, (b) $A = 6.7J_\parallel/L$. The correlations show an (a) algebraic, (b) exponential decay, which signals the (a) superfluid, (b) Mott-insulating phase. The red curve is the fit (a) $\propto x^{-\alpha_1}$, with the fit parameter $\alpha_1 = 0.15 \pm 0.01$, (b) $\propto e^{-\alpha_2 x}$, with the fit parameter $\alpha_2 = 0.11 \pm 0.02$.

observed while increasing the interaction, but it moves towards lower pump strengths and has a smaller extent, $5.24J_\parallel/L \lesssim A \lesssim 5.7J_\parallel/L$ for $U = 2J_\parallel$ (Fig. 5.2(c)-(d)) and $5.2J_\parallel/L \lesssim A \lesssim 5.5J_\parallel/L$ for $U = 2.5J_\parallel$ (Fig. 5.2(e)-(f)).

The incommensurate vortex density below $A \lesssim 5.4J_\parallel/L$ suggests a vortex liquid state (Fig. 5.3(a)). It would have a central charge of two. However, the value of the central charge extracted from our numerical calculations still depends crucially on the system size as shown in Fig. 5.2(b) such that a final conclusion is difficult. As we mentioned, the stability of the vortex superfluid phase for $U = 2J_\parallel$ and $U = 2.5J_\parallel$ is not clear.

For a pump strength above $A \gtrsim 6.1J_\parallel/L$ the rung current is suppressed and the current flows only along the legs of the ladder (Fig. 5.2(a)). The central charge vanishes indicating a totally gapped system. This is confirmed by the exponential decay of the single-particle correlations with distance as seen in Fig. 5.4(b). This state is a Meissner Mott-insulator.

Thus for the parameters $\varphi = 0.9$, $\rho = 0.4$ and $U = 1.5J_\parallel$ the dynamical stabilization of a vortex liquid superfluid, vortex lattice superfluid with $\rho_v = 1/2$ and a Meissner Mott-insulating states is possible.

In Fig. 5.5, we are presenting the entanglement entropy of a subsystem of l rungs embedded in the ladder with $L = 240$ rungs. The behavior of the entropy is given by Eq. (3.62): $S_{vN} = \frac{c}{6} \log \left(\frac{L}{\pi} \sin \frac{\pi l}{L} \right) + s_1$, thus we use this formula the extract the central charge (see Fig. 5.2). In Fig. 5.5(a), as we are in the vortex superfluid phase the entropy scaling presents additional substructure due to the incommensurability characteristic to this phase, this behavior explains the large error bars from Fig. 5.2(a). In Fig. 5.5(b), there is a high agreement between the numerical data and the expected fit, obtaining a central charge close to the characteristic value of the vortex lattice phase, $c = 0.98 \approx 1$. As in the Meissner Mott-insulating state the central charge is zero, we do not expect Eq. (3.62) to capture the behavior of the entanglement entropy scaling, see Fig. 5.5(c).

5.3. Steady state diagram at flux $\varphi = 0.8$ and filling $\rho = 0.8$

In this subsection we solve the self-consistency condition and identify the steady states which can be stabilized as we vary the pump strength A, for flux $\varphi = 0.8$, filling $\rho = 0.8$ and two values of the on-site interaction $U = 1J_\parallel$ and $U = 2J_\parallel$. For this case the dynamic stabilization of VL$_{1/3}$-SF, biased ladder superfluid, and Meissner superfluid states is possible.

The expectation value of the directed rung tunneling $\langle K_\perp \rangle/L$ has a concave curvature, with
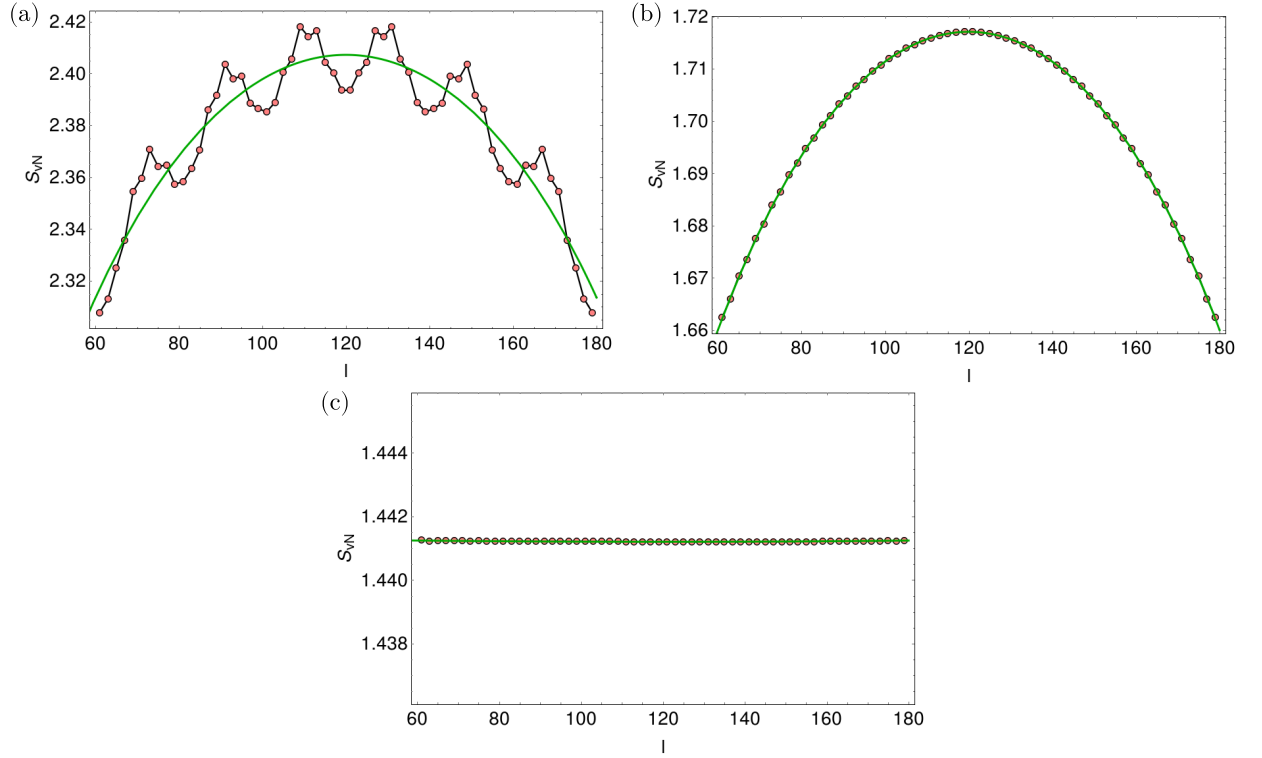
Figure 5.5.: The scaling of the von Neumann entanglement entropy used for computing the central charge presented in Fig. 5.2, in the (a) vortex superfluid (b) vortex lattice superfluid phase and (c) Meissner Mott phase, for $L = 240$, $\varphi = 0.9$, $\rho = 0.5$ and $U = 1.5J_{\parallel}$, (a) $A = 4.88J_{\parallel}/L$, (b) $A = 5.46J_{\parallel}/L$, (c) $A = 6.7J_{\parallel}/L$. The green curve is the fit of the expression from Eq. (3.62) with the fit parameters (a) $c = 1.62 \pm 0.07$, $s_1 = 1.23 \pm 0.05$, (b) $c = 0.988 \pm 0.001$, $s_1 = 1.002 \pm 0.001$, (c) $c = -0.00065 \pm 0.0006$, $s_1 = 1.441 \pm 0.00004$.

Figure 5.6.: Graphical interpretation of the self-consistency condition for the parameters $\varphi = 0.8$, $\rho = 0.8$ with (a) $U = 1J_{\parallel}$, (c) $U = 2J_{\parallel}$. The directed rung tunneling $\langle K_{\perp} \rangle / L$ is represented for two system sizes, $L = 120$ and $L = 60$. The straight (purple) line represents the right-hand side of the self-consistency condition, which is a linear function with slope $\frac{J_{\parallel}}{AL}$. The crossings of the two curves give the solutions of the self-consistency condition. Solutions $J_{\perp}/J_{\parallel}$ of the self-consistency equation which are proportional to the cavity field $Re(\alpha)$ versus the pump strength $AL/J_{\parallel}$, for (b) $U = 1J_{\parallel}$, (d) $U = 2J_{\parallel}$. The filled colored areas represent the extent of different phases. In the grey area the stability of the solutions is not clear for all system sizes.

some additional substructure especially close to the phase transitions. For small values of $J_\perp$, $\langle K_\perp \rangle / L$ has a strong dependence on the size of the system for both $U = 1J_\parallel$ and $U = 2J_\parallel$, as we observe from Fig. 5.6(a),(c) and thus the stability in this region depends crucially on the size of the system. In the following we will concentrate on the states which are stable for all considered system sizes. The non-trivial stable solutions are plotted in Fig. 5.6(b),(d), where we have always chosen the solution $J_\perp > 0$. Not shown are the corresponding solutions at the inverse of the value which exist due to the $\mathbb{Z}_2$ symmetry of the model.

One can observe from Fig. 5.6(b),(d) that we have (system size independent) non-trivial stable solutions with a finite occupation of the cavity field above the pump strength $A \approx 3.19 J_\parallel / L$ for $U = 1J_\parallel$, and $A \approx 3.25 J_\parallel / L$ for $U = 2J_\parallel$.

As for the considered parameter set going from $U = 1J_\parallel$ to $U = 2J_\parallel$ does not change the nature of the phases and the only change appears in the extent of the phase, we will, firstly, characterize the phases for $U = 1J_\parallel$. We have to analyze the behavior of the observables characterizing these states (Fig. 5.7), as explained in Seq. 3.3.

We find a vortex state, with finite rung currents, for $3.19 J_\parallel / L \lesssim A \lesssim 3.59 J_\parallel / L$. We extract the central charge by fitting Eq. (3.62) to the numerically computed von Neumann entanglement entropy. The central charge has a value of $c \approx 1$ in this region, which points, together with the finite rung current, towards a lattice vortex superfluid state. The superfluid nature can also be confirmed by an algebraic decay of the single particle correlation function along the ladder (see Fig. 5.9(a)). The algebraic decay is modulated by a periodic function, with the period of three lattice sites. From the vortex density (Fig. 5.8(a)), we identify the $VL_{1/3}$-SF state corresponding to this modulation. We observe that by increasing the strength of the interactions, the extent of the lattice vortex superfluid state shrinks to $3.25 J_\parallel / L \lesssim A \lesssim 3.45 J_\parallel / L$, (Fig. 5.7(d)).

For $U = 1J_\parallel$, in the region $3.66 J_\parallel / L \lesssim A \lesssim 5.01 J_\parallel / L$, the density imbalance between the two legs acquires finite values with a sharp onset at the lower boundary (Fig. 5.7(c)). This signals the biased ladder state. Our numerical data is not precise enough in order to identify the transition between $VL_{1/3}$-SF and the biased ladder states in the region $3.59 J_\parallel / L \lesssim A \lesssim 3.66 J_\parallel / L$. Whereas our numerical data (Fig. 5.6(b)) suggests multiple solutions for the same value of the pump strength, from our numerical resolution we cannot decide on their stability condition. In the biased ladder state, the currents along the rungs of the ladder are suppressed, which is consistent with the numerical data from Fig. 5.7(a). Additionally, the charge remains constant around $c \approx 1$ (Fig. 5.7(b)). The superfluid nature of the biased ladder state can be inferred from the algebraic decay of the single particle correlation function along the ladder,
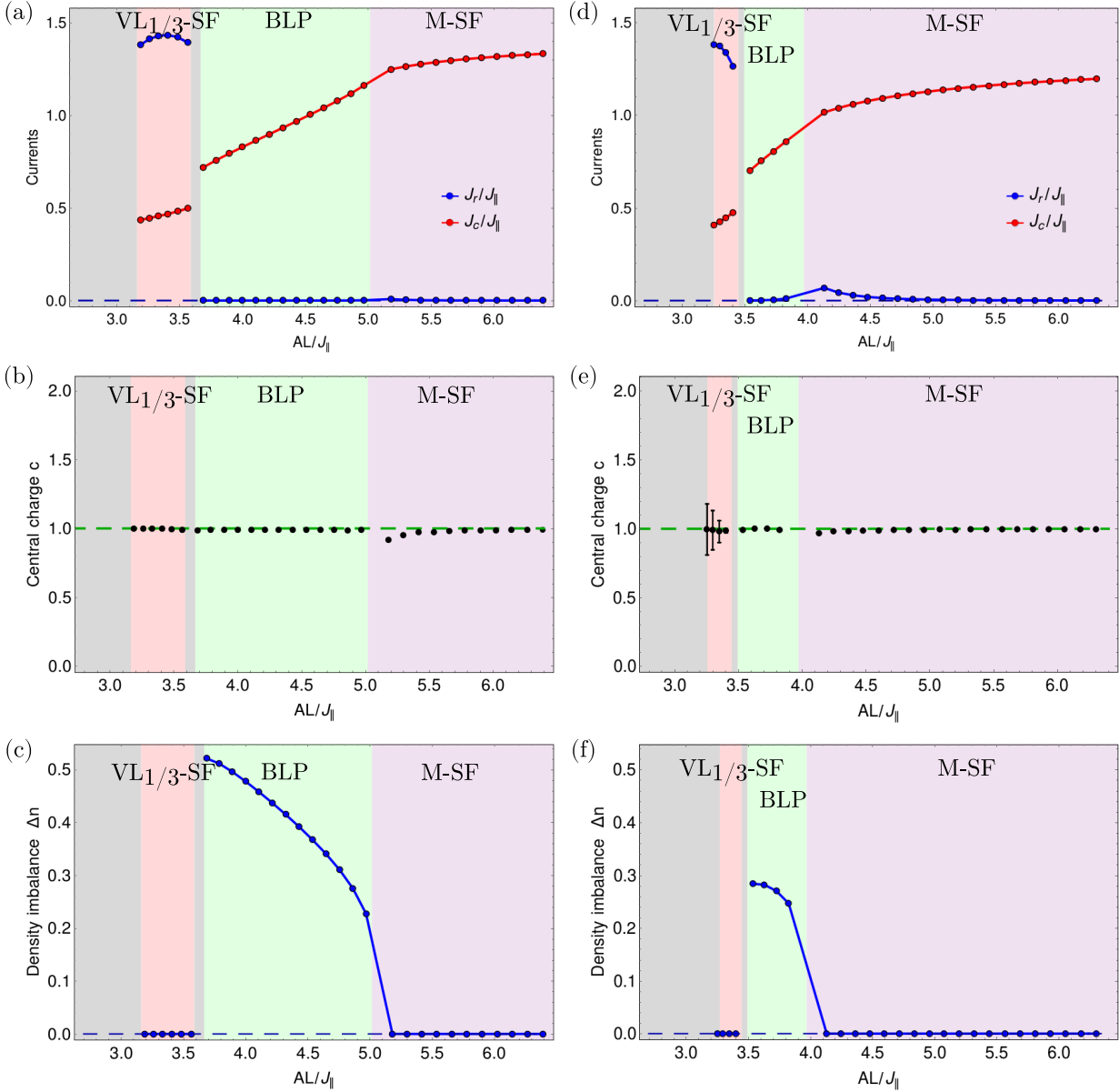
Figure 5.7.: The chiral current J_c and the average rung current J_r as a function of the pump strength $AL/J_\parallel$, for the parameters $\varphi = 0.8$, $\rho = 0.8$ with (a) $U = 1J_\parallel$, (d) $U = 2J_\parallel$. The central charge c, computed from the scaling of entanglement entropy, for (b) $U = 1J_\parallel$, (e) $U = 2J_\parallel$. The errorbars represented the fit error. The density imbalance between the two legs of the ladder, for (c) $U = 1J_\parallel$, (f) $U = 2J_\parallel$. Dashed horizontal lines indicate the constant value 0, or 1, as a guide to the eye.
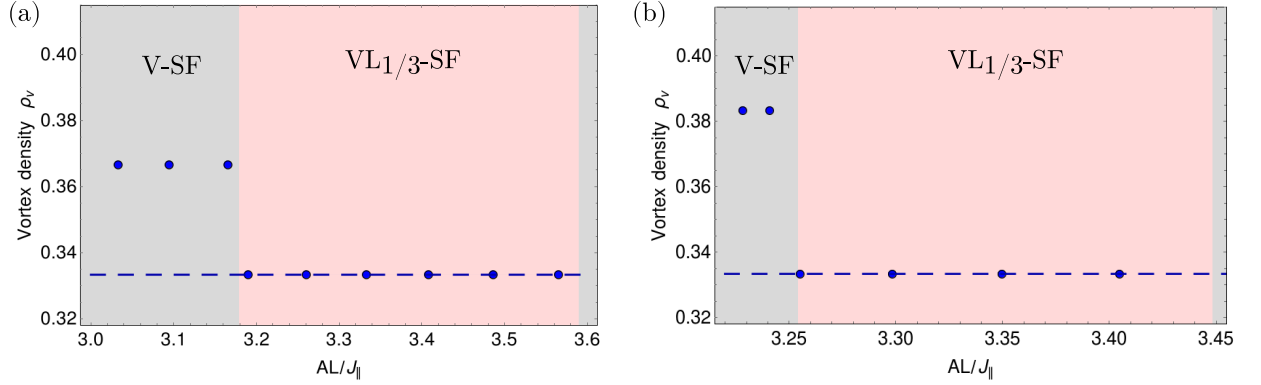
Figure 5.8.: The vortex density ρ_v as a function of the pump strength $AL/J_\parallel$, where the rung current is finite for the parameters $\varphi = 0.8$, $\rho = 0.8$, with (a) $U = 1J_\parallel$, (b) $U = 2J_\parallel$. The vortex density has the value $\rho_v = 1/3$ for (a) $3.19J_\parallel/L \lesssim A \lesssim 3.59J_\parallel/L$, (b) $3.25J_\parallel/L \lesssim A \lesssim 3.45J_\parallel/L$, which represents the VL$_{1/3}$-SF phase. Dashed horizontal line indicates the constant value $1/3$.

which occurs on top of a periodic function (see Fig. 5.9(b)).

It is expected that for stronger on-site interaction [80, 84] the biased ladder phase is reduced and will disappear above a critical value U_c. We can observe this in Fig. 5.7(f), where for $U = 2J_\parallel$, we see a density imbalance only in the region $3.5J_\parallel/L \lesssim A \lesssim 4J_\parallel/L$ and the magnitude of the imbalance is smaller than the one plotted in Fig. 5.7(c).

For large values of the pump strength $A \gtrsim 5.01J_\parallel/L$, the density imbalance vanishes (see Fig. 5.7(c)). The chiral current shows saturation, while the currents on the rungs are still suppressed (see Fig. 5.7(a)). The single particle correlation function decays algebraically. Considering these previous findings together with the fact that the state has one gapless mode ($c \approx 1$), the state above $A \gtrsim 5.01J_\parallel/L$ is a Meissner superfluid. For $U = 2J_\parallel$, the Meissner superfluid can be found also for lower values of the pump strength, the state starts above $A \gtrsim 4J_\parallel/L$.

Thus, for the parameters $\varphi = 0.8$, $\rho = 0.8$ and $U = 1J_\parallel$ the dynamical stabilization of a vortex lattice superfluid with $\rho_v = 1/3$, a biased ladder superfluid and a Meissner superfluid states is possible.

In Fig. 5.10, we are presenting the entanglement entropy of a subsystem of l rungs embedded in the ladder with $L = 240$ rungs. The behavior of the entropy is given by: $S_{vN} = \frac{c}{6}\log\left(\frac{L}{\pi}\sin\frac{\pi l}{L}\right) + s_1$, Eq. (3.62), we use this formula the extract the central charge (see Fig. 5.7). In Fig. 5.5(a), we are in the VL$_{1/3}$-SF phase the entropy scaling presents additional substructure due to the periodicity this phase, in order to reduce the error of the fit one can make use of

the periodicity and fit only the upper or the lower branch. In Figs. 5.5(b),(c), one can observe a good agreement between the numerical data and the expected fit, obtaining a central charge $c = 0.98 \approx 1$ (as one expects in the biased ladder and the Meissner superfluid phases).
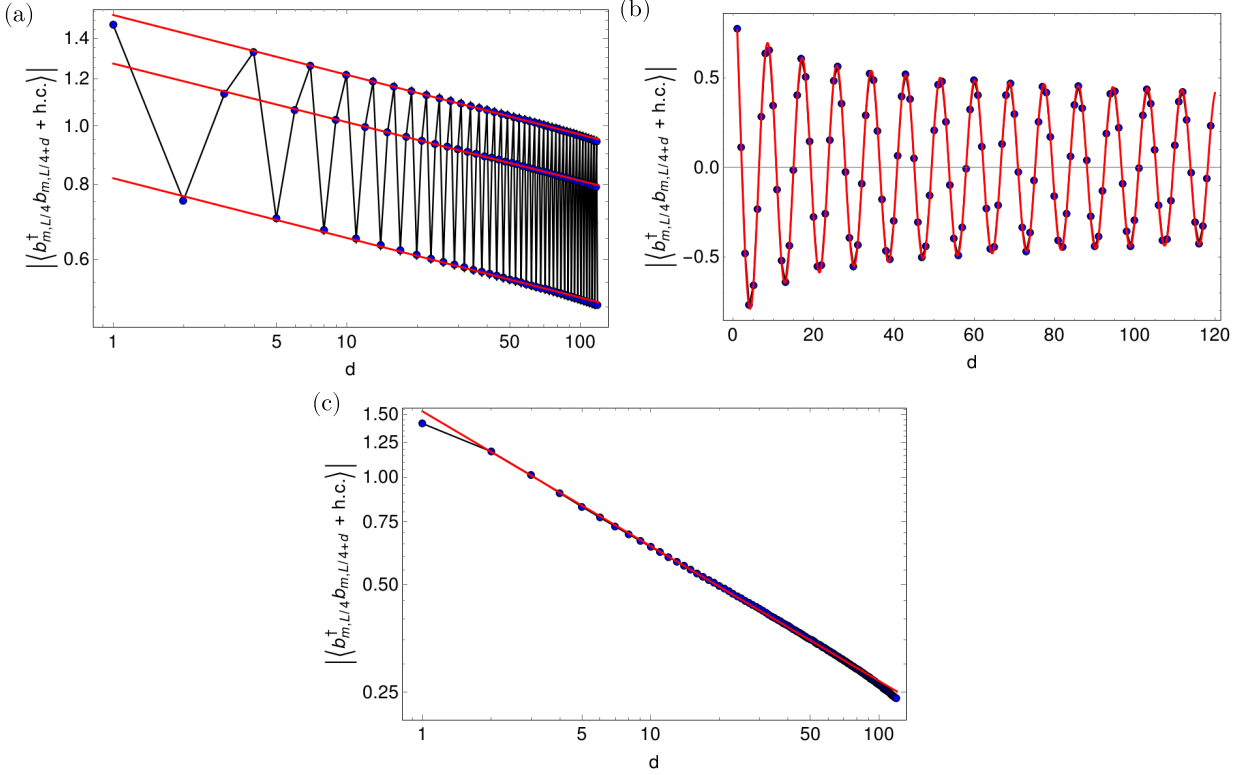
Figure 5.9.: The absolute value of the single particle correlations, $|\langle b^\dagger_{m,L/4} b_{m,L/4+d} + h.c.\rangle|$, (a) in a logarithmic plot, in the vortex lattice phase, (b) biased-ladder phase, and (c) in a logarithmic plot, in the Meissner phase, for $L = 240$, $\varphi = 0.8$, $\rho = 0.8$ and $U = 1J_\parallel$, (a) $A = 3.44J_\parallel/L$, (b) $A = 4.26J_\parallel/L$ and (c) $A = 6.26J_\parallel/L$. The correlations show an algebraic decay, which signals the superfluid phase. The red curve is the fit $\propto x^{-\alpha}$ (for (b) we modulated the algebraic decay with a cosine function), where the fit parameter is (a) $\alpha = 0.098 \pm 0.001$, (b) $\alpha = 0.182 \pm 0.001$, (c) $\alpha = 0.377 \pm 0.001$.

In the following, we look at the single particle correlations in the biased ladder phase. In Fig. 5.9(b) we saw that the correlations show an algebraic decay modulated by a periodic function, signaling the superfluid nature. But in this phase the $\mathbb{Z}_2$ symmetry between the two legs of the ladder is broken, thus we can ask ourselves if the single particle correlations along the legs show a different behavior on each leg. In Fig. 5.11, we represented the absolute value of the single particle correlations along each leg. One can observe that for the leg with a higher density the exponent of the algebraic decay, $\alpha = 0.162 \pm 0.001$, is smaller compared to the exponent

of the algebraic decay of the correlations in the leg with a lower density, $\alpha = 0.191 \pm 0.001$. This behavior is qualitatively consistent with what one observes in a Bose-Hubbard chain in the superfluid phase. In Fig. 5.12, we represented the influence of the filling on the exponent of the algebraic decay in a Bose-Hubbard chain. We observe that in the Bose-Hubbard chain one would expect that the exponent decreases for a higher density, as we see also in the ladder in Fig. 5.11.
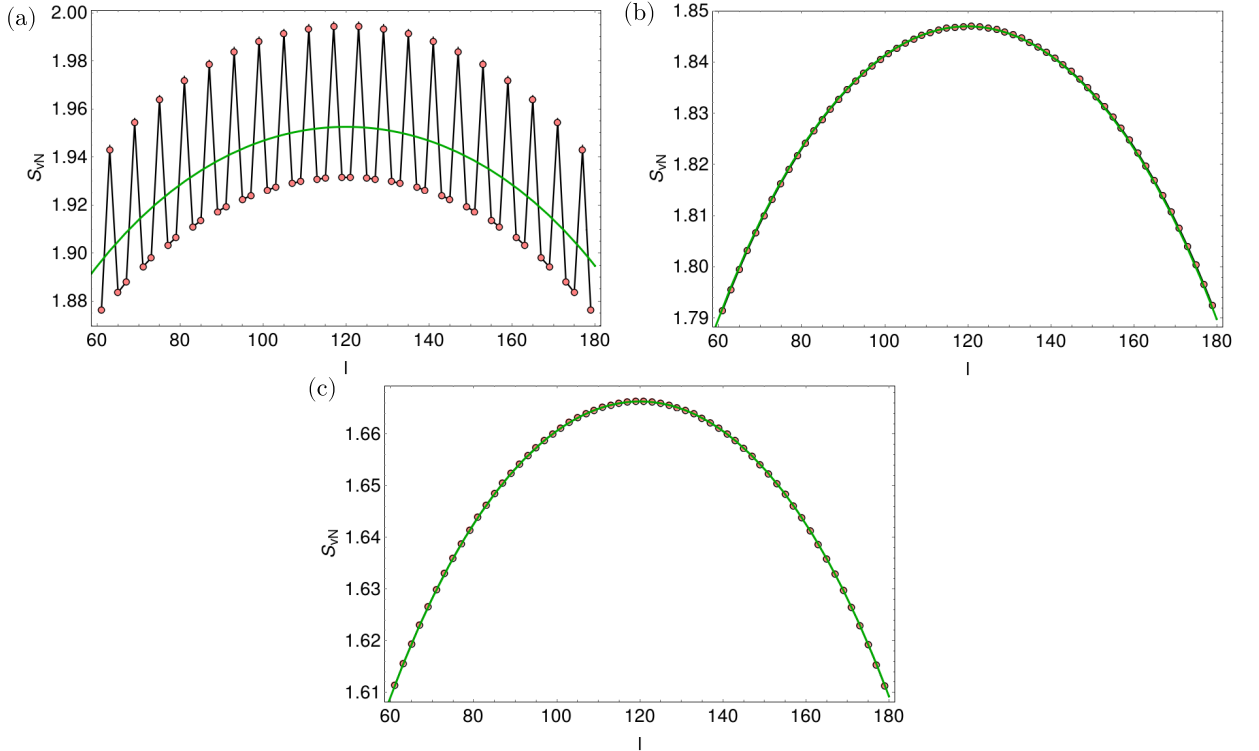
Figure 5.10.: The scaling of the von Neumann entanglement entropy used for computing the central charge presented in Fig. 5.7, in the (a) vortex lattice superfluid phase, (b) biased ladder phase and (c) Meissner superfluid phase, for $L = 240$, $\varphi = 0.8$, $\rho = 0.8$ and $U = 1J_\parallel$, (a) $A = 3.44J_\parallel/L$, (b) $A = 4.26J_\parallel/L$, (c) $A = 6.26J_\parallel/L$. The green curve is the fit of the expression from Eq. (3.62) with the fit parameters (a) $c = 1.00 \pm 0.23$, $s_1 = 1.22 \pm 0.16$, (b) $c = 0.989 \pm 0.002$, $s_1 = 1.131 \pm 0.001$, (c) $c = 0.988 \pm 0.0004$, $s_1 = 0.951 \pm 0.0003$.
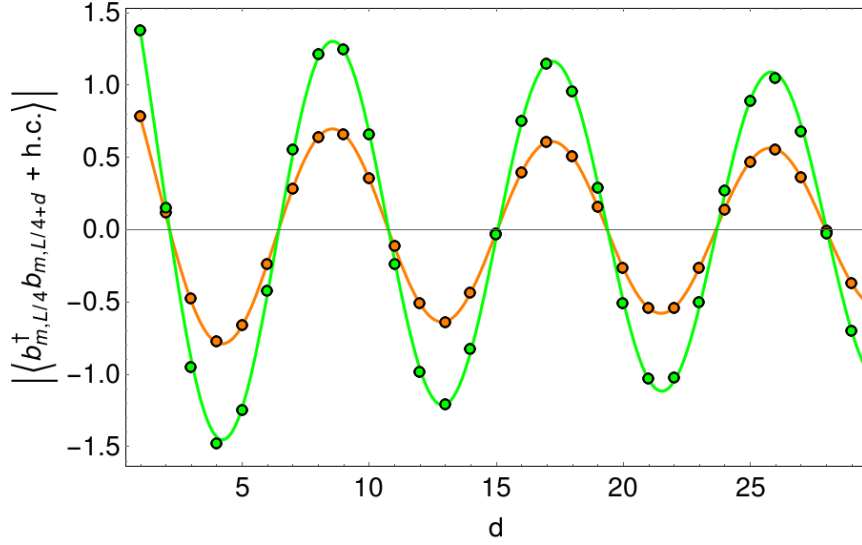
Figure 5.11.: The absolute value of the single particle correlations, $|\langle b_{m,L/4}^{\dagger} b_{m,L/4+d} + h.c.\rangle|$ in the biased-ladder phase along each leg, for $L = 60$, $\varphi = 0.8$, $\rho = 0.8$, $U = 1J_{\parallel}$ and $A = 4.26J_{\parallel}/L$. The green curve corresponds to the leg with higher density $n_1 \approx 1.01$ and the orange curve corresponds to the leg with a lower density $n_2 \approx 0.59$. The correlations show an algebraic decay, which signals the superfluid phase. We fit the data with $\propto x^{-\alpha}$ (modulated with a cosine function), where the fit parameter is $\alpha = 0.162 \pm 0.001$ (green curve) and $\alpha = 0.191 \pm 0.001$ (orange curve).
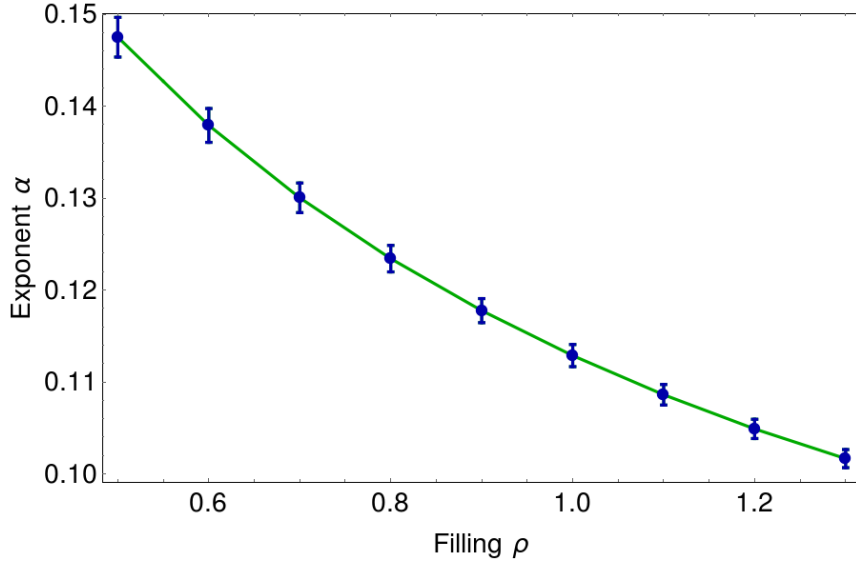
Figure 5.12.: The exponent, α, of the algebraic decay, $\propto x^{-\alpha}$, for the single particle correlations, $|\langle b_{L/4}^{\dagger} b_{L/4+d} + h.c.\rangle|$ in a Bose-Hubbard chain as a function of the filling, for $L = 60$ sites and on-site interaction $U = 1J_{\parallel}$.

6. Summary and Conclusions

In this work we investigated the steady state diagram of bosonic atoms coupled to an optical cavity. The bosonic atoms are confined to quasi-one-dimensional ladder structures formed by optical lattices. The optical lattice geometry is chosen that a large potential offset between the legs exists, which suppresses the tunneling along the rungs of the ladder. Due to the chosen coupling of the atoms and the cavity field, the tunneling on the rungs is restored via the creation or annihilation of a cavity photon and has a spatial dependent phase imprint, which breaks the time reversal symmetry. Above a critical value of the pump strength, due to the feedback between the atoms and the cavity field, a finite occupation of the cavity field mode arises and the bosonic atoms feel an artificial gauge field. This corresponds to a spontaneous self-organization of the system above a critical pump value. In the steady state the bosonic atoms acquire a chiral current due to the artificial magnetic field. We consider an effective Hamiltonian for the bosonic atoms, obtained by the adiabatic elimination of the cavity field. This introduces a self-consistency condition that needs to be solved together with the effective Hamiltonian.

We analyzed low-energy properties of the effective Hamiltonian for the atomic degrees of freedom. The single particle energy bands can exhibit one minimum at $k = 0$, or two distinct minima at finite quasi-momentum, as a function on the value of the rung tunneling amplitude. We performed a Bogoliubov theory for the weakly interacting case and we obtained a linear dispersion relation around $k = 0$ for the case with one minimum (which would correspond to the Meissner superfluid). In the case with 2 minima, we have the situation where only one minimum is populated and a density imbalance exists (biased ladder phase), or the situation with two independent condensates and two phononic modes (corresponding to the vortex superfluid). But the Bogoliubov theory cannot be used to describe the coupled ladder and cavity system, as one cannot solve the self-consistency condition in this framework.

Employing the state of the art density matrix renormalization group method for the effective Hamiltonian and considering the self-consistency condition, we demonstrated the stabilization of Meissner phases both in the superfluid (M-SF) and in the Mott insulator (M-MI) regimes. Additionally, we found vortex superfluid phases which can be incommensurate (V-SF), or commensurate with the ladder (VL$_{\rho_v}$-SF), the vortex lattice states. Finally, a biased-ladder superfluid phase with imbalanced density on the two legs of the ladder can be stabilized. We analyzed the stability of the mentioned phases for different on-site interaction strengths. One of the advan-

tages of the dynamic stabilization of the states is their stability and robustness. The evolution towards the steady states is characterized by a dissipative attractor dynamics which means that many external perturbations decay exponentially towards the steady state.

Experimentally, the proposed setup can be implemented in different ways. We derived our model for the case of the ladder structures created using superlattice potentials. However, an alternative method is to use the synthetic lattice dimension. In this implementation the atoms are confined to one-dimensional structures and the second direction is implemented by internal states of the atoms [118, 124, 125]. The transitions between the two states are implemented via Raman transitions employing the cavity mode and an external pump beam. In this case, our model needs to be extended such that it takes into account the interaction of the different internal atomic states, which translates into the interaction of the atoms on the same rung.

As an outlook, one can extend the presented scheme to a two-dimensional geometry. The ground state of the two-dimensional Bose-Hubbard model in an artificial magnetic field can exhibit exciting phases like vortex lattice superfluid phases with different vortex configurations, that are breaking the spatial symmetry, [111, 126, 127], or bosonic integer and fractional quantum Hall states [128]. The effect of the magnetic field on the phase transitions in the two-dimensional Bose-Hubbard model has also been studied [129]. Thus, the question of which states can be stabilized in the coupled cavity-atomic system is of interest.

A. Appendix

A.1. Header file *bosehubbard.h*

```cpp
#ifndef __ITENSOR_BOSEHUBBARD_H
#define __ITENSOR_BOSEHUBBARD_H
#include "itensor/mps/siteset.h"
#include "math.h"

namespace itensor {
class BoseHubbardSite;
using BoseHubbard = BasicSiteSet<BoseHubbardSite>;
class BoseHubbardSite
    {
    IQIndex s;
        int Nc_;
    public:
    BoseHubbardSite() { }
    BoseHubbardSite(IQIndex I) : s(I) { }
    BoseHubbardSite(int n, Args const& args = Args::global())
        {
                Nc_=args.getInt("Nc");
                                std::vector<IndexQN> inds;
                for (int i=0; i<=Nc_;i++)
                {
                        inds.push_back(IndexQN(Index(nameint("n"+std::to_string(i)+" ",n),1,Site),QN("Nb=",i)));
                }
                s=IQIndex(nameint("site=",n),std::move(inds));
        }
    IQIndex
    index() const { return s; }
    IQIndexVal
    state(std::string const& state)
    {
        int er=0;
        if(state == "0" || state == "Emp" || state == "n0")
    {
                return s(1);
                er=1;
     }
     else
        for(int j=1;j<=Nc_;j++)
        {
                if(state == std::to_string(j) || state=="n"+std::to_string(j))
                {
                        return s(j+1);
                        er=1;
                }
        }
        if(er==0)
    {
       Error("State " + state + " not recognized");
    }
    return IQIndexVal{};
    }
        IQTensor
        op(std::string const& opname,
           Args const& args) const
        {
        auto sP = prime(s);
        IQTensor Op(dag(s),sP);
        if(opname == "Nb")
        {
                        for(int j=1;j<=(Nc_+1);j++)
                        {
                                Op.set(s(j),sP(j),j-1);
                        }
        }
        else
                if(opname == "Nbsquare")
        {
                        for(int j=1;j<=(Nc_+1);j++)
                        {
                                Op.set(s(j),sP(j),(j-1)*(j-1));
                        }
        }
```

```
        else
        if(opname == "B")
        {
                        for(int j=2;j<=(Nc_+1);j++)
                        {
                                Op.set(s(j),sP(j-1),std::sqrt(j*1.-1));
                        }
        }
        else
        if(opname == "Bdag")
        {
                        for(int j=1;j<=Nc_;j++)
                        {
                                Op.set(s(j),sP(j+1),std::sqrt(j*1.));
                        }
        }
            else
        {
            Error("Operator " + opname + " name not recognized");
        }

        return Op;
        }
    };
} //namespace itensor
#endif
```

A.2. Header file *dmrg_modified.h*

```
// DMRG without a fixed number of sweeps
// We present just the part we modified

template <class Tensor, class LocalOpT>
Real inline
DMRGWorker2(MPSt<Tensor>& psi,
            LocalOpT& PH,
            const Sweeps& sweeps,
            const Args& args = Global::args())
    {
    DMRGObserver<Tensor> obs(psi,args);
    Real energy = DMRGWorker2(psi,PH,sweeps,obs,args);
    return energy;
    }

template <class Tensor, class LocalOpT>
Real
DMRGWorker2(MPSt<Tensor>& psi,
            LocalOpT& PH,
            const Sweeps& sweeps,
            DMRGObserver<Tensor>& obs,
            Args args = Global::args())
    {
    const bool quiet = args.getBool("Quiet",false);
    const int debug_level = args.getInt("DebugLevel",(quiet ? 0 : 1));
        const int maxsw=args.getInt("maxsw",30);
        const Real engoal=args.getReal("engoal",1E-8);
    const int N = psi.N();
    Real energy = NAN;
        Real energylast=NAN;
    psi.position(1);
    args.add("DebugLevel",debug_level);
    args.add("DoNormalize",true);
        int sw=1;
        Real enerror=1;
    while(sw<=maxsw && enerror>engoal)
        {
        cpu_time sw_time;
                if(sw<=sweeps.nsweep())
                {
                        args.add("Sweep",sw);
                        args.add("Cutoff",sweeps.cutoff(sw));
                        args.add("Minm",sweeps.minm(sw));
                        args.add("Maxm",sweeps.maxm(sw));
                        args.add("Noise",sweeps.noise(sw));
                        args.add("MaxIter",sweeps.niter(sw));
                }
                else
                {
                        args.add("Sweep",sweeps.nsweep());
```

```
                        args.add("Cutoff",sweeps.cutoff(sweeps.nsweep()));
                        args.add("Minm",sweeps.minm(sweeps.nsweep()));
                        args.add("Maxm",sweeps.maxm(sweeps.nsweep()));
                        args.add("Noise",sweeps.noise(sweeps.nsweep()));
                        args.add("MaxIter",sweeps.niter(sweeps.nsweep()));
                    }

            if(!PH.doWrite()
               && args.defined("WriteM")
               && sweeps.maxm(sw) >= args.getInt("WriteM"))
                {
                if(!quiet)
                    {
                    println("\nTurning on write to disk, write_dir = ",
                            args.getString("WriteDir","./"));
                    }
                PH.doWrite(true);
                }
                    printfln("\n Sweep number: %d",sw);
            for(int b = 1, ha = 1; ha <= 2; sweepnext(b,ha,N))
                {
                if(!quiet)
                    {
                    printfln("Sweep=%d, HS=%d, Bond=(%d,%d)",sw,ha,b,(b+1));
                    }
                PH.position(b,psi);
                auto phi = psi.A(b)*psi.A(b+1);
                energy = davidson(PH,phi,args);
                auto spec = psi.svdBond(b,phi,(ha==1?Fromleft:Fromright),PH,args);
                if(!quiet)
                    {
                    printfln("    Truncated to Cutoff=%.1E, Min_m=%d, Max_m=%d",
                             sweeps.cutoff(sw),
                             sweeps.minm(sw),
                             sweeps.maxm(sw) );
                    printfln("    Trunc. err=%.1E, States kept: %s",
                             spec.truncerr(),
                             showm(linkInd(psi,b)) );
                    }
                obs.lastSpectrum(spec);
                args.add("AtBond",b);
                args.add("HalfSweep",ha);
                args.add("Energy",energy);
                obs.measure(args);
                }
                    if(sw>1)
                    {
                            enerror=std::abs(energylast-energy);
                    }
                    energylast=energy;
            auto sm = sw_time.sincemark();
            printfln("    Sweep %d CPU time = %s (Wall time = %s)",
                     sw,showtime(sm.time),showtime(sm.wall));
            if(obs.checkDone(args)) break;
                    printfln("    energy error: %0.10f",enerror);
                    sw=sw+1;
            }
        psi.normalize();
        return energy;
        }
```

A.3. File *BH_ladder.cc*

```cpp
#include "itensor/all.h"
#include "bosehubbard.h"
#include "dmrg2.h"
#include "math.h"
#include "string.h"
#include "stdio.h"
#include <iomanip>
#include <sstream>
using namespace std;
using namespace itensor;

int
main(int argc, char* argv[])
    {
        //Parse the input file
    if(argc < 2) { printfln("Usage: %s inputfile_dmrg_table",argv[0]); return 0; }
    auto input = InputGroup(argv[1],"input");
```

A.3 File *BH_ladder.cc*

```cpp
    //Read in individual parameters from the input file
    auto N = input.getInt("N"); //needs to be even
        auto U=input.getReal("U",0.0);
        auto Jper=input.getReal("Jper",1.0);
        auto phi=input.getReal("phi",0.0);
        auto bpot=input.getReal("boundpot",0.0);
        auto bnol=input.getInt("bornol",3);
        auto bnor=input.getInt("bornor",3);
        auto Jpar=input.getReal("Jpar",1.0);;//always 1
        auto factp=cos(phi/2*Pi)+sin(phi/2*Pi)*1_i; //Exp(i*phi/2)
        auto factm=cos(phi/2*Pi)-sin(phi/2*Pi)*1_i; //Exp(-i*phi/2)
    auto nsweeps = input.getInt("nsweeps");
    auto quiet = input.getYesNo("quiet",true);
            auto initialstate=input.getInt("initialstate",0);
        //initial state: 0 - 1 boson; 1 - 1 boson/site;
        //2-0.5 boson/site (00 11) 3-0.5 boson/site (01 10)
        //4-0.5 bosons/site (alternate)
        auto mydmrg=input.getYesNo("mydmrg",false); //use my dmrg code or the itensor routine
        auto dmrgfixedsw=input.getYesNo("dmrgfixedsw", true); //fixed number of sweeps
        auto meassw=input.getYesNo("meas_in_sweeps",false);
        auto FileNameOutput=input.getString("outfilename","BHout");
        //create name for output files
        stringstream streamU, streamJper, streamphi;
        streamU << fixed << setprecision(2) << U;
        streamJper << fixed << setprecision(2) << Jper;
        streamphi << fixed << setprecision(2) << phi;
        FileNameOutput=FileNameOutput+"_N"+to_string(N)+"_U"+streamU.str()+"_Jper"+streamJper.str()+"_phi"+streamphi.str();
        //output file for energy
        string outputfilename1=FileNameOutput;
outputfilename1.append("_en.out");
ofstream outputfile1;
outputfile1.open (outputfilename1);
// Read the sweeps parameters from a table.
//
//Read in the sweeps table itself
auto table = InputGroup(input,"sweeps");
//Create the sweeps class & print
auto sweeps = Sweeps(nsweeps,table);
println(sweeps);
    //local bosonic dimension
    auto Nc=input.getInt("bosoncut",3);
    auto sites=BoseHubbard(N,{"Nc",Nc});
    auto init=InitState(sites);
    if(initialstate==1)
    {
            for(int i=1;i<=N;i++)
            {
                    init.set(i,"1");
            }
    }
    else
    if(initialstate==2)
    {
            for(int i=1;i<=N;i++)
            {
                    if(i%2==0)
                            init.set(i,"1");
                    else
                            init.set(i,"0");
            }
    }
    else
    if(initialstate==3)
    {
            for(int i=1;i<=N/2;i++)
            {
                    if(i%2==0)
                            init.set(i,"1");
                    else
                            init.set(i,"0");
            }
            for(int i=N/2+1;i<=N;i++)
            {
                    if(i%2==0)
                            init.set(i,"0");
                    else
                            init.set(i,"1");
            }
    }
    else
    if(initialstate==4)
    {
```

```cpp
                for(int i=1;i<=N;i++)
                {
                        if(i%4==1)
                                init.set(i,"1");
                        else
                        if(i%4==2)
                                init.set(i,"0");
                        else
                        if(i%4==3)
                                init.set(i,"0");
                        else
                                init.set(i,"1");
                }
        }

        IQMPS psi;
        psi=IQMPS(init);
        //definition of the MPO Hamiltonian
        auto ampo=AutoMPO(sites);
        for(int j=1; j<=N; j++)
        {
                ampo+=(U/2),"Nbsquare",j;
                ampo+=(-U/2),"Nb",j;
        }
        for(int j=1; j<N; j++)
        {
                if(j%2==1)
                {
                        ampo+=(-Jper),"Bdag",j+1,"B",j;
                        ampo+=(-Jper),"Bdag",j,"B",j+1;
                }
        }
        for(int j=1; j<N-1; j++)
        {
                if(j%2==1)
                {
                        ampo+=(-Jpar*factp),"Bdag",j,"B",j+2;
                        ampo+=(-Jpar*factm),"Bdag",j+2,"B",j;
                }
                else
                {
                        ampo+=(-Jpar*factm),"Bdag",j,"B",j+2;
                        ampo+=(-Jpar*factp),"Bdag",j+2,"B",j;
                }
        }
        for(int j=1; j<2*bnol+1;j++)
        {
                if(j%2==1)
                {
                        ampo+=(-bpot),"Nb",j;
                }
                else
                {
                        ampo+=(bpot),"Nb",j;
                }
        }
        for(int j=N; j>N-(2*bnor);j--)
        {
                if(j%2==1)
                {
                        ampo+=(-bpot),"Nb",j;
                }
                else
                {
                        ampo+=(bpot),"Nb",j;
                }
        }
        auto H=IQMPO(ampo);
        if(mydmrg)
        {
        auto Heff=LocalMPO<IQTensor>(H);
        Real energy=0;
        //output file for truncation error
        string outputfilename2=FileNameOutput;
outputfilename2.append("_truncerr.out");
ofstream outputfile2;
outputfile2.open (outputfilename2);
        //output file for number of eigenvalues kept
        string outputfilename3=FileNameOutput;
outputfilename3.append("_m.out");
ofstream outputfile3;
outputfile3.open (outputfilename3);
```

A.3 File *BH_ladder.cc*

```cpp
        //output file for measurement of the chiral current during the sweeps
        string outputfilename8=FileNameOutput;
        outputfilename8.append("_SWchcur.out");
        ofstream outputfile8;
        outputfile8.open (outputfilename8);
        //output file for measurement of Kper during the sweeps
        string outputfilename9=FileNameOutput;
        outputfilename9.append("_SWkper.out");
        ofstream outputfile9;
        outputfile9.open (outputfilename9);
        //sweeps
        for(int sw=1; sw<=sweeps.nsweep();++sw)
        {
                if(sw>1)
                {
                        println("Energy=%.20f \n",energy);
                }
                println("Sweep=%d",sw);
                //loop over bonds
                for(int b=1, dir=1; dir!=3; sweepnext(b,dir,N))
                {
                        //regauge and construct Heff
                        psi.position(b);
                        Heff.position(b,psi);
                        //eigenvalues problem
                        IQTensor phi=psi.A(b)*psi.A(b+1);
                        energy=davidson(Heff,phi);
                        outputfile1 <<sw<<" "<<b<<" "<<setprecision(16)<<energy<<"\n";
                        //accuracy parameters for svd
                        auto args=Args("Cutoff",sweeps.cutoff(sw),"Maxm",sweeps.maxm(sw),"Minm",sweeps.minm(sw));
                        //tensors for svd results
                        auto& A=psi.Anc(b);
                        auto& B=psi.Anc(b+1);
                        IQTensor D;
                        Spectrum spec=svd(phi,A,D,B,args);
                        outputfile2 <<sw<<" "<<b<<" "<<setprecision(16)<<spec.truncerr()<<"\n";
                        outputfile3 <<sw<<" "<<b<<" "<<spec.numEigsKept()<<"\n";
                        if(dir==1) //sweeping right
                        {
                                B=D*B;
                        }
                        else
                                if(dir==2) //sweeping left
                                {
                                        A=A*D;
                                }
                }
        }
        println("Energy=%.20f \n",energy);
        outputfile2.close();
        outputfile3.close();
        outputfile8.close();
        outputfile9.close();
        }
        else
        if(dmrgfixedsw==true)
        {
                auto energy2 = dmrg(psi,H,sweeps,{"Quiet",true});
                println("Energy=%.20f \n",energy2);
                outputfile1 <<setprecision(16)<<energy2<<"\n";
        }
        else
        {
                auto maxsw=input.getInt("maxsw", 30); //max number of sweeps in case the precision is not met
                auto engoal=input.getReal("engoal",1E-8); //energy error goal between the sweeps
                auto energy2 = dmrg2(psi,H,sweeps,{"Quiet",true,"maxsw",maxsw,"engoal",engoal});
                        println("\n Energy=%.20f \n",energy2);
                        outputfile1 <<setprecision(16)<<energy2<<"\n";
        }
        outputfile1.close();
        //mps to file
        auto mps_file = input.getYesNo("mps_file",false);
        if(mps_file==true)
        {
                //output file for truncation error
                string outputfilenamemps=FileNameOutput;
                outputfilenamemps.append("_mps");
                writeToFile(outputfilenamemps,psi);
        }
        //operators & measurements
        //density measurement
        auto no_meas = input.getYesNo("no_meas",false); //boson number measurement
```

```cpp
        if(no_meas==true)
        {
                auto no_all= input.getYesNo("no_all",false); //measure all sites
                //output file for density
                string outputfilename4=FileNameOutput;
                outputfilename4.append("_dens.out");
                ofstream outputfile4;
                outputfile4.open (outputfilename4);
                if(no_all==true)
                {
                        Real Ntot=0;
                        for(int i=1;i<=N;i++)
                        {
                                IQTensor Ni= sites.op("Nb",i);
                                psi.position(i);
                                IQTensor ket = psi.A(i);
                                IQTensor bra = dag(prime(ket,Site));
                                auto nav = (bra*Ni*ket).real();
                                printf("at site %u <n>=%0.10f \n",i,nav);
                                outputfile4 <<i<<" "<<setprecision(16)<<nav<<"\n";
                                Ntot+=nav;
                        }
                        printf("\n<N_total>=%0.5f \n",Ntot);
                        outputfile4 <<"\n"<<setprecision(16)<<Ntot<<"\n";
                }
                outputfile4.close();
        }

        //rung current measurement
        auto rcur_meas = input.getYesNo("rcur_meas",false);
        if(rcur_meas==true)
        {
                auto rcur_all= input.getYesNo("rcur_all",false); //measure all rungs
                //output file for rung currents
                string outputfilename5=FileNameOutput;
                outputfilename5.append("_rcur.out");
                ofstream outputfile5;
                outputfile5.open (outputfilename5);
                if(rcur_all==true)
                {
                        for(int i=1;i<=N;i+=2)
                        {
                                IQTensor bdag1= sites.op("Bdag",i);
                                IQTensor b1= sites.op("B",i);
                                IQTensor bdag2= sites.op("Bdag",i+1);
                                IQTensor b2= sites.op("B",i+1);
                                psi.position(i);
                                IQTensor ket = psi.A(i)*psi.A(i+1);
                                IQTensor bra = dag(prime(ket,Site));
                                auto c1 = (bra*bdag1*b2*ket).cplx();
                                auto c2 = (bra*bdag2*b1*ket).cplx();
                                printf("between site %u and site %u <j_r>=-iJ_per(%0.5f - %0.5f) = %0.5f \n",i,i+1,c1,c2,imag(
                                        Jper*(c1-c2)));

                                outputfile5 <<i<<" "<<i+1<<" "<<setprecision(16)<<imag(Jper*(c1-c2))<<"\n";
                        }
                }
                outputfile5.close();
        }
        //leg current measurement
        auto lcur_meas = input.getYesNo("lcur_meas",false);
        if(lcur_meas==true)
        {
                auto lcur_all= input.getYesNo("lcur_all",false); //measure all leg currents

                string outputfilename6=FileNameOutput;
                outputfilename6.append("_lcur.out");
                ofstream outputfile6;
                outputfile6.open (outputfilename6);
                if(lcur_all==true)
                {
                        Real jch=0;
                        Real jch_part=0;

                        for(int i=1;i<N-1;i++)
                        {
                                IQTensor bdag1= sites.op("Bdag",i);
                                IQTensor b1= sites.op("B",i);
                                IQTensor bdag2= sites.op("Bdag",i+2);
                                IQTensor b2= sites.op("B",i+2);
                                psi.position(i);
                                IQTensor ket = psi.A(i)*psi.A(i+1)*psi.A(i+2);
```

```cpp
                            IQTensor bra=dag(ket);
                            IQTensor ket1=bdag1*b2*ket;
                            ket1=noprime(ket1);
                            IQTensor ket2=bdag2*b1*ket;
                            ket2=noprime(ket2);
                            auto c1 = (bra*ket1).cplx();
                            auto c2 =(bra*ket2).cplx();
                            if(i%2==1)
                            {
                                    auto jloc1=factp*c1;
                                    auto jloc2=factm*c2;
                                    printf("between site %u and site %u <j_l>=-i(%0.5f - %0.5f) = %0.5f \n",i,i+2,jloc1,
                                        jloc2,imag(jloc1-jloc2));
                                    outputfile6 <<i<<" "<<i+2<<" "<<setprecision(16)<<imag(jloc1-jloc2)<<"\n";
                                    jch+=imag(jloc1-jloc2);
                                    if(i>=N/4 && i<3*N/4)
                                    {
                                            jch_part+=imag(jloc1-jloc2);
                                    }
                            }
                            else
                            {
                                    auto jloc1=factm*c1;
                                    auto jloc2=factp*c2;
                                    printf("between site %u and site %u <j_l>=-i(%0.5f - %0.5f) = %0.5f \n",i,i+2,jloc1,
                                        jloc2,imag(jloc1-jloc2));
                                    outputfile6 <<i<<" "<<i+2<<" "<<setprecision(16)<<imag(jloc1-jloc2)<<"\n";
                                    jch+=imag(jloc2-jloc1);
                                    if(i>=N/4 && i<3*N/4)
                                    {
                                            jch_part+=imag(jloc2-jloc1);
                                    }
                            }
                    }
                    jch=jch/N;
                    jch_part=jch_part/N*2;
                    printf("\nJ_ch=%0.5f ",jch);
                    printf("\nJ_ch_part=%0.5f %u\n",jch_part);
                    outputfile6 <<"\n"<<setprecision(16)<<jch<<"\n";
                    outputfile6 <<setprecision(16)<<jch_part<<"\n";
            }
            outputfile6.close();
    }
    //K_per measurement
    auto kper_meas = input.getYesNo("kper_meas",false); //Kper measurement
    if(kper_meas==true)
    {
            auto kper_all= input.getYesNo("kper_all",false); //measure all sites
            string outputfilename7=FileNameOutput;
            outputfilename7.append("_Kper.out");
            ofstream outputfile7;
            outputfile7.open (outputfilename7);
            if(kper_all==true)
            {
                    Real kpertotr=0, kpertoti=0;
                    Real kpertotr_part=0, kpertoti_part=0;
                    for(int i=1;i<N;i=i+2)
                    {
                            IQTensor bdagi= sites.op("Bdag",i);
                            IQTensor bi1= sites.op("B",i+1);
                            psi.position(i);
                            IQTensor ket = psi.A(i)*psi.A(i+1);
                            IQTensor bra = dag(prime(ket,Site));
                            auto kper = (bra*bdagi*bi1*ket).cplx();
                            printf("between site %u and site %u <K_per>=%0.10f \n",i,i+1,kper);
                            outputfile7 <<i<<" "<<i+1<<" "<<setprecision(16)<<kper<<"\n";
                            kpertotr+=real(kper);
                            kpertoti+=imag(kper);
                            if(i>=N/4 && i<3*N/4)
                                    {
                                            kpertotr_part+=real(kper);
                                            kpertoti_part+=imag(kper);
                                    }
                    }
                    printf("\n<Kper_total>=%0.10f %0.10f \n",kpertotr,kpertoti);
                    outputfile7 <<"\n"<<setprecision(16)<<kpertotr<<"  "<<kpertoti<<"\n";
                    kpertotr=kpertotr/N*2;
                    kpertoti=kpertoti/N*2;
                    outputfile7 <<setprecision(16)<<kpertotr<<"  "<<kpertoti<<"\n";
                    kpertotr_part=kpertotr_part/N*4;
                    kpertoti_part=kpertoti_part/N*4;
                    outputfile7 <<setprecision(16)<<kpertotr_part<<"  "<<kpertoti_part;
```

```cpp
                }
                outputfile7.close();
        }
        auto corr_meas = input.getYesNo("corr_meas",false); //correlations
        if(corr_meas==true)
        {
                string outputfilename8=FileNameOutput;
                outputfilename8.append("_corr_densR.out");
                ofstream outputfile8;
                outputfile8.open (outputfilename8);
                string outputfilename9=FileNameOutput;
                outputfilename9.append("_corr_densL.out");
                ofstream outputfile9;
                outputfile9.open (outputfilename9);
                string outputfilename10=FileNameOutput;
                outputfilename10.append("_corr_longrange.out");
                ofstream outputfile10;
                outputfile10.open (outputfilename10);
                for(int i=N/4;i<3*N/4;i++)
                        {
                                if(i%2==1)
                                {
                                        IQTensor N1= sites.op("Nb",i);
                                        IQTensor N2= sites.op("Nb",i+1);
                                        IQTensor N3= sites.op("Nb",i+2);
                                        psi.position(i);
                                        IQTensor ket = psi.A(i)*psi.A(i+1)*psi.A(i+2);
                                        IQTensor bra=dag(ket);
                                        IQTensor ket1=N1*N2*ket;
                                        ket1=noprime(ket1);
                                        IQTensor ket21=N1*ket;
                                        ket21=noprime(ket21);
                                        IQTensor ket22=N2*ket;
                                        ket22=noprime(ket22);
                                        auto nnav=(bra*ket1).real();
                                        auto nav1=(bra*ket21).real();
                                        auto nav2=(bra*ket22).real();
                                        printf("between site %u and site %u <n1n2>-<n1><n2>=%0.10f-%0.10f=%0.10f \n",i,i+1,nnav
                                                ,(nav1*nav2),(nnav-nav1*nav2));
                                        outputfile8 <<i<<" "<<i+1<<" "<<setprecision(16)<<nnav<<" "<<(nnav-nav1*nav2)<<"\n";
                                        ket1=N1*N3*ket;
                                        ket1=noprime(ket1);
                                        IQTensor ket23=N3*ket;
                                        ket23=noprime(ket23);
                                        nnav=(bra*ket1).real();
                                        auto nav3=(bra*ket23).real();
                                        printf("between site %u and site %u <n1n2>-<n1><n2>=%0.10f-%0.10f=%0.10f \n",i,i+2,nnav
                                                ,(nav1*nav3),(nnav-nav1*nav3));
                                        outputfile9 <<i<<" "<<i+2<<" "<<setprecision(16)<<nnav<<" "<<(nnav-nav1*nav3)<<"\n";
                                }
                                else
                                {
                                        IQTensor N1= sites.op("Nb",i);
                                        IQTensor N3= sites.op("Nb",i+2);
                                        psi.position(i);
                                        IQTensor ket = psi.A(i)*psi.A(i+1)*psi.A(i+2);
                                        IQTensor bra=dag(ket);
                                        IQTensor ket1=N1*N3*ket;
                                        ket1=noprime(ket1);
                                        IQTensor ket21=N1*ket;
                                        ket21=noprime(ket21);
                                        IQTensor ket23=N3*ket;
                                        ket23=noprime(ket23);
                                        auto nnav=(bra*ket1).real();
                                        auto nav1=(bra*ket21).real();
                                        auto nav3=(bra*ket23).real();
                                        printf("between site %u and site %u <n1n2>-<n1><n2>=%0.10f-%0.10f=%0.10f \n",i,i+2,nnav
                                                ,(nav1*nav3),(nnav-nav1*nav3));
                                        outputfile9 <<i<<" "<<i+2<<" "<<setprecision(16)<<nnav<<" "<<(nnav-nav1*nav3)<<"\n";
                                }
                        }
                        int poz=N/4;
                        if(poz%2==0)
                                poz=poz+1;
                        IQTensor bdag1= sites.op("Bdag",poz);
                        psi.position(poz);
                        IQTensor braket = psi.A(poz);
                        braket=bdag1*braket;
                        auto ir = commonIndex(psi.A(poz),psi.A(poz+1),Link);
                        braket=braket*dag(prime(prime(psi.A(poz),Site),ir));
                        braket=braket*psi.A(poz+1);
                        braket=braket*dag(prime(psi.A(poz+1),Link));
```

```cpp
                    for(int i=2;i<N/2;i=i+2)
                    {
                            IQTensor bi1= sites.op("B",poz+i);
                            braket=braket*psi.A(poz+i);
                            IQTensor braket_fin=braket*bi1;
                            auto il = commonIndex(psi.A(poz+i),psi.A(poz+i-1),Link);
                            braket_fin=braket_fin*dag(prime(prime(psi.A(poz+i),Site),il));
                            auto corr=braket_fin.cplx();
                            printf("between site %u and site %u corr=%0.10f \n",poz,poz+i,corr);
                            outputfile10 <<poz<<" "<<poz+i<<" "<<setprecision(16)<<real(corr)<<" "<<imag(corr)<<"\n";
                            braket=braket*dag(prime(psi.A(poz+i),Link));
                            braket=braket*psi.A(poz+i+1);
                            braket=braket*dag(prime(psi.A(poz+i+1),Link));
                    }
            outputfile8.close();
            outputfile9.close();
            outputfile10.close();
        }

    auto entropy_meas = input.getYesNo("entropy_meas",false); //entropy
    if(entropy_meas==true)
    {
            string outputfilename11=FileNameOutput;
            outputfilename11.append("_entropy.out");
            ofstream outputfile11;
            outputfile11.open (outputfilename11);
            for(int i=N/4;i<3*N/4;i++)
                    {
                            psi.position(i);
                            IQTensor wf = psi.A(i)*psi.A(i+1);
                            auto U = psi.A(i);
                            IQTensor S,V;
                            auto spectrum = svd(wf,U,S,V);
                            Real SvN = 0.;
                            for(auto p : spectrum.eigs())
                                    {
                                            if(p > 1E-12) SvN += -p*log(p);
                                    }
                            printf("entropy at site %u =%0.10f \n",i,SvN);
                            outputfile11 <<i<<" "<<setprecision(16)<<SvN<<"\n";
                    }
            outputfile11.close();
        }
    return 0;
}
```

List of Figures

List of Figures

Bibliography

[1] M. H. Anderson, J. R. Ensher, M. R. Matthews, C. E. Wieman, and E. A. Cornell, "Observation of Bose-Einstein Condensation in a Dilute Atomic Vapor," *Science*, vol. 269, no. 5221, pp. 198–201, 1995.

[2] C. C. Bradley, C. A. Sackett, J. J. Tollett, and R. G. Hulet, "Evidence of Bose-Einstein Condensation in an Atomic Gas with Attractive Interactions," *Phys. Rev. Lett.*, vol. 75, pp. 1687–1690, Aug 1995.

[3] K. B. Davis, M. O. Mewes, M. R. Andrews, N. J. van Druten, D. S. Durfee, D. M. Kurn, and W. Ketterle, "Bose-Einstein Condensation in a Gas of Sodium Atoms," *Phys. Rev. Lett.*, vol. 75, pp. 3969–3973, Nov 1995.

[4] B. DeMarco and D. S. Jin, "Onset of Fermi Degeneracy in a Trapped Atomic Gas," *Science*, vol. 285, no. 5434, pp. 1703–1706, 1999.

[5] I. Bloch, J. Dalibard, and W. Zwerger, "Many-body physics with ultracold gases," *Rev. Mod. Phys.*, vol. 80, pp. 885–964, Jul 2008.

[6] M. Greiner, O. Mandel, T. Esslinger, T. W. Hansch, and I. Bloch, "Quantum phase transition from a superfluid to a Mott insulator in a gas of ultracold atoms," *Nature*, vol. 415, pp. 39–44, Jan 2002.

[7] D. Jaksch, C. Bruder, J. I. Cirac, C. W. Gardiner, and P. Zoller, "Cold Bosonic Atoms in Optical Lattices," *Phys. Rev. Lett.*, vol. 81, pp. 3108–3111, Oct 1998.

[8] M. P. A. Fisher, P. B. Weichman, G. Grinstein, and D. S. Fisher, "Boson localization and the superfluid-insulator transition," *Phys. Rev. B*, vol. 40, pp. 546–570, Jul 1989.

[9] G. G. Batrouni, R. T. Scalettar, and G. T. Zimanyi, "Quantum critical phenomena in one-dimensional Bose systems," *Phys. Rev. Lett.*, vol. 65, pp. 1765–1768, Oct 1990.

[10] D. S. Rokhsar and B. G. Kotliar, "Gutzwiller projection for bosons," *Phys. Rev. B*, vol. 44, pp. 10328–10332, Nov 1991.

[11] G. G. Batrouni and R. T. Scalettar, "World-line quantum Monte Carlo algorithm for a one-dimensional Bose model," *Phys. Rev. B*, vol. 46, pp. 9051–9062, Oct 1992.

[12] J. K. Freericks and H. Monien, "Phase diagram of the Bose-Hubbard Model," *EPL (Europhysics Letters)*, vol. 26, no. 7, p. 545, 1994.

[13] J. K. Freericks and H. Monien, "Strong-coupling expansions for the pure and disordered Bose-Hubbard model," *Phys. Rev. B*, vol. 53, pp. 2691–2700, Feb 1996.

[14] R. V. Pai, R. Pandit, H. R. Krishnamurthy, and S. Ramasesha, "One-Dimensional Disordered Bosonic Hubbard Model: A Density-Matrix Renormalization Group Study," *Phys. Rev. Lett.*, vol. 76, pp. 2937–2940, Apr 1996.

[15] T. D. Kühner and H. Monien, "Phases of the one-dimensional Bose-Hubbard model," *Phys. Rev. B*, vol. 58, pp. R14741–R14744, Dec 1998.

[16] N. Elstner and H. Monien, "Dynamics and thermodynamics of the Bose-Hubbard model," *Phys. Rev. B*, vol. 59, pp. 12184–12187, May 1999.

[17] T. D. Kühner, S. R. White, and H. Monien, "One-dimensional Bose-Hubbard model with nearest-neighbor interaction," *Phys. Rev. B*, vol. 61, pp. 12474–12489, May 2000.

[18] B. Capogrosso-Sansone, N. V. Prokof'ev, and B. V. Svistunov, "Phase diagram and thermodynamics of the three-dimensional Bose-Hubbard model," *Phys. Rev. B*, vol. 75, p. 134302, Apr 2007.

[19] J. K. Freericks, H. R. Krishnamurthy, Y. Kato, N. Kawashima, and N. Trivedi, "Strong-coupling expansion for the momentum distribution of the Bose-Hubbard model with benchmarking against exact numerical results," *Phys. Rev. A*, vol. 79, p. 053631, May 2009.

[20] M. A. Cazalilla, R. Citro, T. Giamarchi, E. Orignac, and M. Rigol, "One dimensional bosons: From condensed matter systems to ultracold gases," *Rev. Mod. Phys.*, vol. 83, pp. 1405–1466, Dec 2011.

[21] H. Ritsch, P. Domokos, F. Brennecke, and T. Esslinger, "Cold atoms in cavity-generated dynamical optical potentials," *Rev. Mod. Phys.*, vol. 85, pp. 553–601, Apr 2013.

[22] M. Müller, S. Diehl, G. Pupillo, and P. Zoller, "Engineered Open Systems and Quantum Simulations with Atoms and Ions," *Advances in Atomic Molecular and Optical Physics*, vol. 61, pp. 1–80, 2012.

[23] K. Baumann, C. Guerlin, F. Brennecke, and T. Esslinger, "Dicke quantum phase transition with a superfluid gas in an optical cavity," *Nature*, vol. 464, pp. 1301–1306, Apr 2010.

Bibliography

[24] K. Jens, K. Hans, W. Matthias, M. Ludwig, and A. Hemmerich, "Dynamical phase transition in the open Dicke model," *Proc. Natl. Acad. Sci. USA*, vol. 112, no. 3290, 2015.

[25] P. Domokos and H. Ritsch, "Collective Cooling and Self-Organization of Atoms in a Cavity," *Phys. Rev. Lett.*, vol. 89, p. 253003, Dec 2002.

[26] F. Dimer, B. Estienne, A. S. Parkins, and H. J. Carmichael, "Proposed realization of the Dicke-model quantum phase transition in an optical cavity QED system," *Phys. Rev. A*, vol. 75, p. 013804, Jan 2007.

[27] Nagy, D., Szirmai, G., and Domokos, P., "Self-organization of a Bose-Einstein condensate in an optical cavity," *Eur. Phys. J. D*, vol. 48, no. 1, pp. 127–137, 2008.

[28] F. Piazza, P. Strack, and W. Zwerger, "Bose-Einstein condensation versus Dicke-Hepp-Lieb transition in an optical cavity," *Annals of Physics*, vol. 339, pp. 135 – 159, 2013.

[29] J. Klinder, H. Keßler, M. R. Bakhtiari, M. Thorwart, and A. Hemmerich, "Observation of a Superradiant Mott Insulator in the Dicke-Hubbard Model," *Phys. Rev. Lett.*, vol. 115, p. 230403, Dec 2015.

[30] R. Landig, L. Hruby, N. Dogra, M. Landini, R. Mottl, T. Donner, and T. Esslinger, "Quantum phases from competing short- and long-range interactions in an optical lattice," *Nature*, vol. 532, pp. 476–479, Apr 2016. Letter.

[31] T. J. Elliott and I. B. Mekhov, "Engineering many-body dynamics with quantum light potentials and measurements," *Phys. Rev. A*, vol. 94, p. 013614, Jul 2016.

[32] M. R. Bakhtiari, A. Hemmerich, H. Ritsch, and M. Thorwart, "Nonequilibrium Phase Transition of Interacting Bosons in an Intra-Cavity Optical Lattice," *Phys. Rev. Lett.*, vol. 114, p. 123601, Mar 2015.

[33] C. Maschler and H. Ritsch, "Cold Atom Dynamics in a Quantum Optical Lattice Potential," *Phys. Rev. Lett.*, vol. 95, p. 260401, Dec 2005.

[34] C. Maschler, I. B. Mekhov, and H. Ritsch, "Ultracold atoms in optical lattices generated by quantized lightÂ fields," *The European Physical Journal D*, vol. 46, pp. 545–560, Mar 2008.

[35] J. Larson, B. Damski, G. Morigi, and M. Lewenstein, "Mott-Insulator States of Ultracold Atoms in Optical Resonators," *Phys. Rev. Lett.*, vol. 100, p. 050401, Feb 2008.

[36] W. Niedenzu, R. Schulze, A. Vukics, and H. Ritsch, "Microscopic dynamics of ultracold particles in a ring-cavity optical lattice," *Phys. Rev. A*, vol. 82, p. 043605, Oct 2010.

[37] A. O. Silver, M. Hohenadler, M. J. Bhaseen, and B. D. Simons, "Bose-Hubbard models coupled to cavity light fields," *Phys. Rev. A*, vol. 81, p. 023617, Feb 2010.

[38] S. Fernández-Vidal, G. De Chiara, J. Larson, and G. Morigi, "Quantum ground state of self-organized atomic crystals in optical resonators," *Phys. Rev. A*, vol. 81, p. 043407, Apr 2010.

[39] Y. Li, L. He, and W. Hofstetter, "Lattice-supersolid phase of strongly correlated bosons in an optical cavity," *Phys. Rev. A*, vol. 87, p. 051604, May 2013.

[40] S. Safaei, C. Miniatura, and B. Grémaud, "Triangular and honeycomb lattices of cold atoms in optical cavities," *Phys. Rev. A*, vol. 92, p. 043810, Oct 2015.

[41] J. Larson, G. Morigi, and M. Lewenstein, "Cold Fermi atomic gases in a pumped optical resonator," *Phys. Rev. A*, vol. 78, p. 023815, Aug 2008.

[42] J. Keeling, M. J. Bhaseen, and B. D. Simons, "Fermionic Superradiance in a Transversely Pumped Optical Cavity," *Phys. Rev. Lett.*, vol. 112, p. 143002, Apr 2014.

[43] F. Piazza and P. Strack, "Umklapp Superradiance with a Collisionless Quantum Degenerate Fermi Gas," *Phys. Rev. Lett.*, vol. 112, p. 143003, Apr 2014.

[44] Y. Chen, Z. Yu, and H. Zhai, "Superradiance of Degenerate Fermi Gases in a Cavity," *Phys. Rev. Lett.*, vol. 112, p. 143004, Apr 2014.

[45] S. Gopalakrishnan, B. L. Lev, and P. M. Goldbart, "Emergent crystallinity and frustration with Bose-Einstein condensates in multimode cavities," *Nat Phys*, vol. 5, pp. 845–850, Nov 2009.

[46] S. Nimmrichter, K. Hammerer, P. Asenbaum, H. Ritsch, and M. Arndt, "Master equation for the motion of a polarizable particle in a multimode cavity," *New Journal of Physics*, vol. 12, no. 8, p. 083003, 2010.

[47] P. Strack and S. Sachdev, "Dicke Quantum Spin Glass of Atoms and Photons," *Phys. Rev. Lett.*, vol. 107, p. 277202, Dec 2011.

[48] S. Gopalakrishnan, B. L. Lev, and P. M. Goldbart, "Frustration and Glassiness in Spin Models with Cavity-Mediated Interactions," *Phys. Rev. Lett.*, vol. 107, p. 277201, Dec 2011.

Bibliography

[49] M. Müller, P. Strack, and S. Sachdev, "Quantum charge glasses of itinerant fermions with cavity-mediated long-range interactions," *Phys. Rev. A*, vol. 86, p. 023604, Aug 2012.

[50] H. Habibian, A. Winter, S. Paganelli, H. Rieger, and G. Morigi, "Bose-Glass Phases of Ultracold Atoms due to Cavity Backaction," *Phys. Rev. Lett.*, vol. 110, p. 075304, Feb 2013.

[51] A. Janot, T. Hyart, P. R. Eastham, and B. Rosenow, "Superfluid Stiffness of a Driven Dissipative Condensate with Disorder," *Phys. Rev. Lett.*, vol. 111, p. 230403, Dec 2013.

[52] M. Buchhold, P. Strack, S. Sachdev, and S. Diehl, "Dicke-model quantum spin and photon glass in optical cavities: Nonequilibrium theory and experimental signatures," *Phys. Rev. A*, vol. 87, p. 063622, Jun 2013.

[53] Y. Deng, J. Cheng, H. Jing, and S. Yi, "Bose-Einstein Condensates with Cavity-Mediated Spin-Orbit Coupling," *Phys. Rev. Lett.*, vol. 112, p. 143007, Apr 2014.

[54] L. Dong, L. Zhou, B. Wu, B. Ramachandhran, and H. Pu, "Cavity-assisted dynamical spin-orbit coupling in cold atoms," *Phys. Rev. A*, vol. 89, p. 011602, Jan 2014.

[55] J.-S. Pan, X.-J. Liu, W. Zhang, W. Yi, and G.-C. Guo, "Topological Superradiant States in a Degenerate Fermi Gas," *Phys. Rev. Lett.*, vol. 115, p. 045303, Jul 2015.

[56] B. Padhi and S. Ghosh, "Spin-orbit-coupled Bose-Einstein condensates in a cavity: Route to magnetic phases through cavity transmission," *Phys. Rev. A*, vol. 90, p. 023627, Aug 2014.

[57] F. Mivehvar and D. L. Feder, "Synthetic spin-orbit interactions and magnetic fields in ring-cavity QED," *Phys. Rev. A*, vol. 89, p. 013803, Jan 2014.

[58] F. Mivehvar and D. L. Feder, "Enhanced stripe phases in spin-orbit-coupled Bose-Einstein condensates in ring cavities," *Phys. Rev. A*, vol. 92, p. 023611, Aug 2015.

[59] K. v. Klitzing, G. Dorda, and M. Pepper, "New Method for High-Accuracy Determination of the Fine-Structure Constant Based on Quantized Hall Resistance," *Phys. Rev. Lett.*, vol. 45, pp. 494–497, Aug 1980.

[60] D. C. Tsui, H. L. Stormer, and A. C. Gossard, "Two-Dimensional Magnetotransport in the Extreme Quantum Limit," *Phys. Rev. Lett.*, vol. 48, pp. 1559–1562, May 1982.

[61] R. B. Laughlin, "Anomalous Quantum Hall Effect: An Incompressible Quantum Fluid with Fractionally Charged Excitations," *Phys. Rev. Lett.*, vol. 50, pp. 1395–1398, May 1983.

[62] G. Moore and N. Read, "Nonabelions in the fractional quantum hall effect," *Nuclear Physics B*, vol. 360, no. 2, pp. 362 – 396, 1991.

[63] J. Dalibard, F. Gerbier, G. Juzeliūnas, and P. Öhberg, "Colloquium," *Rev. Mod. Phys.*, vol. 83, pp. 1523–1543, Nov 2011.

[64] N. R. Cooper and J. Dalibard, "Reaching Fractional Quantum Hall States with Optical Flux Lattices," *Phys. Rev. Lett.*, vol. 110, p. 185301, Apr 2013.

[65] N. Goldman, G. Juzeliūnas, P. "Ohberg, and I. B. Spielman, "Light-induced gauge fields for ultracold atoms," *Reports on Progress in Physics*, vol. 77, no. 12, p. 126401, 2014.

[66] Y.-J. Lin, R. L. Compton, A. R. Perry, W. D. Phillips, J. V. Porto, and I. B. Spielman, "Bose-Einstein Condensate in a Uniform Light-Induced Vector Potential," *Phys. Rev. Lett.*, vol. 102, p. 130401, Mar 2009.

[67] Y.-J. Lin, R. L. Compton, K. Jimenez-Garcia, J. V. Porto, and I. B. Spielman, "Synthetic magnetic fields for ultracold neutral atoms," *Nature*, vol. 462, pp. 628–632, Dec 2009.

[68] J. Struck, C. Ölschläger, R. Le Targat, P. Soltan-Panahi, A. Eckardt, M. Lewenstein, P. Windpassinger, and K. Sengstock, "Quantum Simulation of Frustrated Classical Magnetism in Triangular Optical Lattices," *Science*, vol. 333, no. 6045, pp. 996–999, 2011.

[69] M. Aidelsburger, M. Atala, S. Nascimbène, S. Trotzky, Y.-A. Chen, and I. Bloch, "Experimental Realization of Strong Effective Magnetic Fields in an Optical Lattice," *Phys. Rev. Lett.*, vol. 107, p. 255301, Dec 2011.

[70] H. Miyake, G. A. Siviloglou, C. J. Kennedy, W. C. Burton, and W. Ketterle, "Realizing the Harper Hamiltonian with Laser-Assisted Tunneling in Optical Lattices," *Phys. Rev. Lett.*, vol. 111, p. 185302, Oct 2013.

[71] D. Jaksch and P. Zoller, "Creation of effective magnetic fields in optical lattices: the Hofstadter butterfly for cold neutral atoms," *New Journal of Physics*, vol. 5, no. 1, p. 56, 2003.

[72] M. Aidelsburger, M. Atala, M. Lohse, J. T. Barreiro, B. Paredes, and I. Bloch, "Realization of the Hofstadter Hamiltonian with Ultracold Atoms in Optical Lattices," *Phys. Rev. Lett.*, vol. 111, p. 185301, Oct 2013.

[73] M. Aidelsburger, M. Lohse, C. Schweizer, M. Atala, J. T. Barreiro, S. Nascimbene, N. R. Cooper, I. Bloch, and N. Goldman, "Measuring the Chern number of Hofstadter bands with ultracold bosonic atoms," *Nat Phys*, vol. 11, pp. 162–166, Feb 2015. Letter.

Bibliography

[74] M. Atala, M. Aidelsburger, M. Lohse, J. T. Barreiro, B. Paredes, and I. Bloch, "Observation of chiral currents with ultracold atoms in bosonic ladders," *Nat Phys*, vol. 10, pp. 588–593, Aug 2014. Article.

[75] G. Jotzu, M. Messer, R. Desbuquois, M. Lebrat, T. Uehlinger, D. Greif, and T. Esslinger, "Experimental realization of the topological Haldane model with ultracold fermions," *Nature*, vol. 515, pp. 237–240, Nov 2014. Letter.

[76] E. Orignac and T. Giamarchi, "Meissner effect in a bosonic ladder," *Phys. Rev. B*, vol. 64, p. 144515, Sep 2001.

[77] A. Tokuno and A. Georges, "Ground states of a Bose-Hubbard ladder in an artificial magnetic field: field-theoretical approach," *New Journal of Physics*, vol. 16, no. 7, p. 073005, 2014.

[78] M. Piraud, F. Heidrich-Meisner, I. P. McCulloch, S. Greschner, T. Vekua, and U. Schollwöck, "Vortex and Meissner phases of strongly interacting bosons on a two-leg ladder," *Phys. Rev. B*, vol. 91, p. 140406, Apr 2015.

[79] S. Greschner, M. Piraud, F. Heidrich-Meisner, I. P. McCulloch, U. Schollwöck, and T. Vekua, "Spontaneous Increase of Magnetic Flux and Chiral-Current Reversal in Bosonic Ladders: Swimming against the Tide," *Phys. Rev. Lett.*, vol. 115, p. 190402, Nov 2015.

[80] S. Greschner, M. Piraud, F. Heidrich-Meisner, I. P. McCulloch, U. Schollwöck, and T. Vekua, "Symmetry-broken states in a system of interacting bosons on a two-leg ladder with a uniform Abelian gauge field," *Phys. Rev. A*, vol. 94, p. 063628, Dec 2016.

[81] A. Dhar, M. Maji, T. Mishra, R. V. Pai, S. Mukerjee, and A. Paramekanti, "Bose-Hubbard model in a strong effective magnetic field: Emergence of a chiral Mott insulator ground state," *Phys. Rev. A*, vol. 85, p. 041602, Apr 2012.

[82] A. Dhar, T. Mishra, M. Maji, R. V. Pai, S. Mukerjee, and A. Paramekanti, "Chiral Mott insulator with staggered loop currents in the fully frustrated Bose-Hubbard model," *Phys. Rev. B*, vol. 87, p. 174501, May 2013.

[83] R. Wei and E. J. Mueller, "Theory of bosons in two-leg ladders with large magnetic fields," *Phys. Rev. A*, vol. 89, p. 063617, Jun 2014.

[84] S. Uchino and A. Tokuno, "Population-imbalance instability in a Bose-Hubbard ladder in the presence of a magnetic flux," *Phys. Rev. A*, vol. 92, p. 013625, Jul 2015.

[85] S. Uchino, "Analytical approach to a bosonic ladder subject to a magnetic field," *Phys. Rev. A*, vol. 93, p. 053629, May 2016.

[86] A. Petrescu and K. Le Hur, "Chiral Mott insulators, Meissner effect, and Laughlin states in quantum ladders," *Phys. Rev. B*, vol. 91, p. 054520, Feb 2015.

[87] M. Calvanese Strinati, E. Cornfeld, D. Rossini, S. Barbarino, M. Dalmonte, R. Fazio, E. Sela, and L. Mazza, "Laughlin-like States in Bosonic and Fermionic Atomic Synthetic Ladders," *Phys. Rev. X*, vol. 7, p. 021033, Jun 2017.

[88] A. Petrescu, M. Piraud, G. Roux, I. P. McCulloch, and K. Le Hur, "Precursor of the Laughlin state of hard-core bosons on a two-leg ladder," *Phys. Rev. B*, vol. 96, p. 014524, Jul 2017.

[89] M. Di Dio, S. De Palo, E. Orignac, R. Citro, and M.-L. Chiofalo, "Persisting Meissner state and incommensurate phases of hard-core boson ladders in a flux," *Phys. Rev. B*, vol. 92, p. 060506, Aug 2015.

[90] E. Orignac, R. Citro, M. D. Dio, S. D. Palo, and M.-L. Chiofalo, "Incommensurate phases of a bosonic two-leg ladder under a flux," *New Journal of Physics*, vol. 18, no. 5, p. 055017, 2016.

[91] E. Orignac, R. Citro, M. Di Dio, and S. De Palo, "Vortex lattice melting in a boson ladder in an artificial gauge field," *Phys. Rev. B*, vol. 96, p. 014518, Jul 2017.

[92] A. Sheikhan, F. Brennecke, and C. Kollath, "Cavity-induced generation of nontrivial topological states in a two-dimensional Fermi gas," *Phys. Rev. A*, vol. 94, p. 061603, Dec 2016.

[93] C. Kollath, A. Sheikhan, S. Wolff, and F. Brennecke, "Ultracold Fermions in a Cavity-Induced Artificial Magnetic Field," *Phys. Rev. Lett.*, vol. 116, p. 060401, 2016.

[94] S. Wolff, A. Sheikhan, and C. Kollath, "Dissipative time evolution of a chiral state after a quantum quench," *Phys. Rev. A*, vol. 94, p. 043609, Oct 2016.

[95] A. Sheikhan, F. Brennecke, and C. Kollath, "Cavity-induced chiral states of fermionic quantum gases," *Phys. Rev. A*, vol. 93, p. 043609, 2016.

[96] W. Zheng and N. R. Cooper, "Superradiance Induced Particle Flow via Dynamical Gauge Coupling," *Phys. Rev. Lett.*, vol. 117, p. 175302, Oct 2016.

Bibliography

[97] K. E. Ballantine, B. L. Lev, and J. Keeling, "Meissner-like Effect for a Synthetic Gauge Field in Multimode Cavity QED," *Phys. Rev. Lett.*, vol. 118, p. 045302, Jan 2017.

[98] C.-M. Halati, A. Sheikhan, and C. Kollath, "A cavity-induced artificial gauge field in a Bose-Hubbard ladder," *arXiv:1707.04123*, 2017.

[99] H. Carmichael, *Statistical Methods in Quantum Optics 1: Master Equations and Fokker-Planck Equations.* Springer-Verlag Berlin Heidelberg, 1st ed. ed., 1999.

[100] L. Tian, "Cavity-assisted dynamical quantum phase transition at bifurcation points," *Phys. Rev. A*, vol. 93, p. 043850, Apr 2016.

[101] S. T. Carr, B. N. Narozhny, and A. A. Nersesyan, "Spinless fermionic ladders in a magnetic field: Phase diagram," *Phys. Rev. B*, vol. 73, p. 195114, May 2006.

[102] G. Roux, E. Orignac, S. R. White, and D. Poilblanc, "Diamagnetism of doped two-leg ladders and probing the nature of their commensurate phases," *Phys. Rev. B*, vol. 76, p. 195105, Nov 2007.

[103] A. Jaefari and E. Fradkin, "Pair-density-wave superconducting order in two-leg ladders," *Phys. Rev. B*, vol. 85, p. 035104, Jan 2012.

[104] D. Hügel and B. Paredes, "Chiral ladders and the edges of quantum hall insulators," *Phys. Rev. A*, vol. 89, p. 023619, Feb 2014.

[105] L. Pitaevskii and S. Stringari, *Bose-Einstein Condensation.* Oxford Science Publications, 1st ed. ed., 2003.

[106] N. M. Hugenholtz and D. Pines, "Ground-State Energy and Excitation Spectrum of a System of Interacting Bosons," *Phys. Rev.*, vol. 116, pp. 489–506, Nov 1959.

[107] A. M. Ettouhami, "Re-Examining Bogoliubov's Theory of an Interacting Bose Gas," *Progress of Theoretical Physics*, vol. 127, no. 3, pp. 453–533, 2012.

[108] J.-P. Blaizot and G. Ripka, *Quantum Theory of Finite Systems.* The MIT Press, 1985.

[109] M.-W. Xiao, "Theory of transformation for the diagonalization of quadratic Hamiltonians," *arXiv:0908.0787*, Aug. 2009.

[110] A. R. Kolovsky, "Bogoliubov depletion of the fragmented condensate in the bosonic flux ladder," *Phys. Rev. A*, vol. 95, p. 033622, Mar 2017.

[111] S. Powell, R. Barnett, R. Sensarma, and S. Das Sarma, "Bogoliubov theory of interacting bosons on a lattice in a synthetic magnetic field," *Phys. Rev. A*, vol. 83, p. 013612, Jan 2011.

[112] G. Vidal, J. I. Latorre, E. Rico, and A. Kitaev, "Entanglement in Quantum Critical Phenomena," *Phys. Rev. Lett.*, vol. 90, p. 227902, Jun 2003.

[113] P. Calabrese and J. Cardy, "Entanglement entropy and quantum field theory," *Journal of Statistical Mechanics: Theory and Experiment*, vol. 2004, no. 06, p. P06002, 2004.

[114] C. Holzhey, F. Larsen, and F. Wilczek, "Geometric and renormalized entropy in conformal field theory," *Nuclear Physics B*, vol. 424, no. 3, pp. 443 – 467, 1994.

[115] N. Laflorencie, E. S. Sørensen, M.-S. Chang, and I. Affleck, "Boundary Effects in the Critical Scaling of Entanglement Entropy in 1D Systems," *Phys. Rev. Lett.*, vol. 96, p. 100603, Mar 2006.

[116] I. Affleck and A. W. W. Ludwig, "Universal noninteger "ground-state degeneracy" in critical quantum systems," *Phys. Rev. Lett.*, vol. 67, pp. 161–164, Jul 1991.

[117] T. Giamarchi, *Quantum Physics in One Dimension*. Oxford Science Publications, 2003.

[118] B. K. Stuhl, H.-I. Lu, L. M. Aycock, D. Genkina, and I. B. Spielman, "Visualizing edge states with an atomic Bose gas in the quantum Hall regime," *Science*, vol. 349, no. 6255, pp. 1514–1518, 2015.

[119] S. R. White, "Density matrix formulation for quantum renormalization groups," *Phys. Rev. Lett.*, vol. 69, pp. 2863–2866, Nov 1992.

[120] U. Schollwöck, "The density-matrix renormalization group," *Rev. Mod. Phys.*, vol. 77, pp. 259–315, Apr 2005.

[121] U. Schollwöck, "The density-matrix renormalization group in the age of matrix product states," *Annals of Physics*, vol. 326, no. 1, pp. 96 – 192, 2011. January 2011 Special Issue.

[122] K. A. Hallberg, "New trends in density matrix renormalization," *Advances in Physics*, vol. 55, no. 5-6, pp. 477–526, 2006.

[123] "ITensor Library." `http://itensor.org`.

[124] A. Celi, P. Massignan, J. Ruseckas, N. Goldman, I. B. Spielman, G. Juzeliūnas, and M. Lewenstein, "Synthetic Gauge Fields in Synthetic Dimensions," *Phys. Rev. Lett.*, vol. 112, p. 043001, Jan 2014.

Bibliography

[125] M. Mancini, G. Pagano, G. Cappellini, L. Livi, M. Rider, J. Catani, C. Sias, P. Zoller, M. Inguscio, M. Dalmonte, and L. Fallani, "Observation of chiral edge states with neutral fermions in synthetic Hall ribbons," *Science*, vol. 349, no. 6255, pp. 1510–1513, 2015.

[126] D. S. Goldbaum and E. J. Mueller, "Vortex lattices of bosons in deep rotating optical lattices," *Phys. Rev. A*, vol. 77, p. 033629, Mar 2008.

[127] D. S. Goldbaum and E. J. Mueller, "Commensurability and hysteretic evolution of vortex configurations in rotating optical lattices," *Phys. Rev. A*, vol. 79, p. 063625, Jun 2009.

[128] Y.-C. He, F. Grusdt, A. Kaufman, M. Greiner, and A. Vishwanath, "Realizing and Adiabatically Preparing Bosonic Integer and Fractional Quantum Hall states in Optical Lattices," *arXiv:1703.00430*, Mar. 2017.

[129] M. Niemeyer, J. K. Freericks, and H. Monien, "Strong-coupling perturbation theory for the two-dimensional Bose-Hubbard model in a magnetic field," *Phys. Rev. B*, vol. 60, pp. 2357–2362, Jul 1999.

Statement

I hereby declare that the work presented here was formulated by myself and that no sources or tools other than those cited were used.

Date	Signature